Université Bordeaux Montaigne

Ecole Doctorale Montaigne Humanité (ED 480)

THESE DE DOCTORAT EN « SCIENCES ET TECHNOLOGIES (TERRE, EAU, IMAGE) »

GEORESSOURCES ET ENVIRONNEMENTS EA 3592

TRANSPORT DES MICROPLASTIQUES ET DES NANOPLASTIQUES DANS LES MILIEUX POREUX SATURES : APPROCHES EXPERIMENTALES ET MODELISATION

Présentée et soutenue publiquement le 24 Mai 2024 par

Hande Mahide OKUTAN

Sous la Direction de M. Philippe LE COUSTUMER et M. Bedri KURTULUŞ

Membres du Jury :

M. Frederic HUNEAU,	Pr,	Université de Corse Pasquale Paoli, France
M. Mohammed BAALOUSHA,	Pr,	Université de South Carolina, Etats-Unis
M. Moumtaz RAZACK,	Pr,	Université de Poitiers, France
Mme Sena AKCER-ON,	MCF,	Université de Muğla Sıtkı Koçman, Turquie
M. Emrah PEKKAN,	Dr,	Université Technique d'Eskişehir, Turquie
M. Serge STOLL,	Dr,	Université de Genève, Suisse

RESUME

Objectifs de la thèse

Grâce à une approche multidisciplinaire intégrant des investigations expérimentales, une modélisation analytique et numérique, et une surveillance environnementale, cette étude cherche à faire progresser notre compréhension des phénomènes de transport et de rétention des microplastiques (MPls) et des nanoplastiques (NPls) dans les milieux poreux, à élucider leurs interactions avec les environnements d'eaux souterraines et les stations d'épuration industrielles dans la perspective de l'efficacité des filtres à sable et à contribuer au développement de solutions scientifiques pour atténuer la pollution plastique et sauvegarder les ressources d'eau douce pour les générations actuelles et futures.

Le chapitre 1 donne un aperçu des différentes variables physiques et chimiques qui influencent le comportement des microplastiques et des nanoplastiques (MNPls) dans les milieux poreux. Le chapitre 2 donne un aperçu complet des matériaux et des méthodologies utilisés dans cette étude. Des explications détaillées des procédures expérimentales et de leurs fondements théoriques sont fournies pour assurer la clarté et la compréhension.

Les recherches du chapitre 3 ont commencé par une exploration des paramètres de transport hydrodynamique dans les milieux poreux saturés, en utilisant des techniques de traceurs fluorescents qui permettent de comprendre les propriétés des milieux poreux. Des solutions analytiques existantes pour le transport de solutés ont été utilisées et testées afin d'évaluer leur aptitude à modéliser le transport de MPls. Ceci a impliqué la réalisation d'expériences en colonnes unidimensionnelles, incorporant à la fois un traceur conservateur (fluorescéine) et un MPls en polyéthylène (PE) d'une taille de 200-500 µm. Ensuite, des solutions analytiques ont été mises en œuvre, en sélectionnant les équations appropriées basées sur la méthode d'injection : instantanée pour la fluorescéine et à durée finie pour les MPls PE. Enfin, une approche de solution inverse a été utilisée pour extraire les paramètres hydrodynamiques spécifiques au transport des MPls à travers les milieux poreux à partir des solutions analytiques.

Le chapitre 4 aborde la complexité de l'utilisation de milieux poreux et de MPls plus petits, ce qui nécessite une solution numérique approfondie par rapport aux méthodes analytiques. Cette section de la thèse est consacrée à l'étude de la capacité de filtration des milieux poreux, en se concentrant spécifiquement sur le transport de particules MPl de type PE, d'une taille de 16 ± 6 µm, dans un milieu poreux saturé de type sable de quartz. De même, dans la section précédente, un colorant fluorescent a été utilisé pour établir les propriétés hydrodynamiques du sable. En outre, l'étude vise à évaluer l'efficacité de la filtration à l'aide de modèles numériques dérivés des équations d'écoulement et de transport. Cette étude implique la détermination des paramètres de sorption à

l'aide de modèles de sorption cinétique réversible et irréversible, la quantification des efficacités de rétention et l'examen de l'impact des variations de débit sur les phénomènes de transport.

Le chapitre 5 repose sur l'hypothèse de base selon laquelle l'efficacité de la filtration sur sable pour retenir les NPls est influencée par leurs fonctionnalités de surface, une influence encore modulée par la présence d'agents tensioactifs dans le système de filtration. Les conditions expérimentales ont été adaptées du système de filtration sur sable de la station industrielle de traitement de l'eau potable (STEP) de Genève, en Suisse. Elles ont ensuite été reproduites dans des conditions de laboratoire avec du sable et des débits similaires afin de combler les lacunes des études existantes concernant la dynamique de rétention et l'efficacité de la filtration sur sable pour les NPls. L'objectif était d'étudier l'efficacité de rétention du système de filtration sur sable de la STEP en présence de divers groupes fonctionnels de surface, revêtements et concentrations de NPls de polystyrène (PS). En outre, l'impact des surfactants sur les processus d'adsorption et de désorption a été exploré. En outre, les propriétés d'homoagrégation ont été évaluées à l'aide d'une méthode non conventionnelle connue sous le nom d'analyse des dimensions fractales, qui n'est pas couramment employée dans les études portant sur l'efficacité de la rétention des matières plastiques à la suite d'approches de filtration sur sable.

Il est essentiel de comprendre les mécanismes qui régissent le transport des MPls et des NPls dans les milieux poreux. Elle permet de clarifier leur devenir dans l'environnement et leurs impacts écologiques, d'éclairer les stratégies d'évaluation et de gestion des risques et de préserver l'intégrité des ressources en eau douce et des réserves d'eau potable.

Chapitre 3 : Étude expérimentale unidimensionnelle du transport de microplastiques en polyéthylène dans un milieu homogène saturé

Okutan, H.M.; Sağir Ç.; Fontaine, C.; Nauleau, B.; Kurtulus, B.; Le Coustumer, P.; Razack, M.; One-Dimensional Experimental Investigation of Polyethylene Microplastic Transport in a Homogeneous Saturated Medium. Frontiers in Environmental Science 2022, 10:885875. https://doi.org/10.3389/fenvs.2022.885875

Les plastiques sont largement utilisés dans tous les domaines de la vie. Les microplastiques (MPls) sont considérés comme des contaminants émergents dans la nature. Pourtant, les paramètres de transport des MPls dans les eaux souterraines ne sont pas bien caractérisés. Dans cette étude, le transport des MPls dans les milieux homogènes saturés a été étudié. À cette fin, des essais en colonne unidimensionnels ont été réalisés à l'aide de traceurs fluorescents et microplastiques afin de déterminer les conditions hydrodynamiques du transport des microplastiques dans les laboratoires de l'Université de Poitiers, en France. Les milieux testés étaient la silice de grande taille, la silice de petite taille, le sable et le gravier grossier. Les paramètres de transport hydrodynamique ont été calculés par la méthode de la solution inverse en utilisant les résultats des solutions expérimentales et analytiques. Seul le gravier grossier avec des pores d'une taille minimale de 1 mm et maximale de 20 mm (5 mm de médiane) et une porosité cinématique de 40,2 % s'est avéré adapté au transport du polyéthylène (PE) usagé dont la taille des particules se situait entre 200 et 500 µm. Il n'est pas possible de transporter des particules de PE de la taille sélectionnée

à partir de milieux à grains fins. Le transport s'est effectué dans des milieux à gros grains tels que le gravier grossier. Les valeurs de dispersivité calculées pour le gravier grossier étaient de 2,58 cm et 3,02 cm en utilisant des traceurs fluorescents et PE, respectivement. Les expériences ont montré que les particules de PE utilisées ne peuvent pas être transportées si la vitesse d'écoulement moyenne est inférieure à 2,02 cm/min dans le milieu de gravier grossier. L'accumulation de microplastiques pourrait être un problème pour un aquifère réel plutôt que son transport, étant donné que la vitesse d'écoulement réelle des eaux souterraines est généralement beaucoup plus faible.

Chapitre 4 : Comprendre l'efficacité de rétention des microplastiques et la dynamique de sorption dans les milieux poreux.

Okutan, H.; Sağır, Ç.; Kurtuluş, B.; Özmen, H.B.; Pekkan, E.; Razack, M.; Le Coustumer, P. Understanding Microplastics Retention Efficiency and Sorption Dynamics in Porous Media. Preprints 2024, 2024021670. https://doi.org/10.20944/preprints202402.1670.v1 (Submitted to Nanomaterials MDPI)

Les plastiques sont devenus omniprésents dans la société moderne et sont largement utilisés dans divers secteurs. Cependant, leur recyclabilité inadéquate, associée aux processus de dégradation et d'abrasion, entraîne souvent la fragmentation des plastiques en morceaux plus petits, appelés MPl, qui se retrouvent ensuite dans les environnements naturels par le biais de divers mécanismes de transport tels que le vent, le ruissellement et l'infiltration. Une fois libérées dans l'environnement, ces particules de MPl présentent des risques importants pour les écosystèmes naturels, notamment les ressources en eau douce, car elles peuvent perturber des équilibres écologiques délicats et nuire aux organismes vivants.

Les propriétés de filtration des milieux poreux jouent un rôle crucial dans la régulation de la qualité des eaux souterraines en éliminant ou en réduisant la concentration des particules et des contaminants au fur et à mesure que l'eau se déplace dans le sous-sol. Il est essentiel de comprendre les mécanismes complexes de filtration dans les milieux poreux pour concevoir des stratégies efficaces visant à atténuer la contamination par les MPl.

Le processus de filtration dans les milieux poreux comporte trois étapes clés : le transport, l'attachement et le détachement. Des mécanismes physiques tels que la diffusion brownienne, le dépôt, l'interception directe et l'hydrodynamique régissent le transport des particules dans les pores des filtres. La cinétique de sorption joue un rôle important dans l'attachement et le détachement des particules dans les milieux poreux, des facteurs tels que le débit et la taille des particules influençant la dynamique de sorption.

Les montages expérimentaux ont impliqué l'utilisation de sable de quartz comme milieu poreux en raison de son utilisation répandue et de sa disponibilité. Les études expérimentales ont été menées à l'université technique d'Eskisehir, en Turquie. La détermination de la taille des particules de sable et de la conductivité hydraulique a fourni des paramètres essentiels pour comprendre l'efficacité de la filtration. L'utilisation de traceurs à colorants fluorescents et la modélisation numérique ont

permis de calculer la porosité et la dispersivité effectives, améliorant ainsi la compréhension des caractéristiques des milieux poreux. Les expériences de transport menées dans des colonnes acryliques ont suivi une séquence systématique, commençant par des tests de perméamètre à tête constante pour vérifier la conductivité hydraulique, suivis par des expériences de traçage de colorant pour évaluer les propriétés hydrodynamiques, et se terminant par des expériences de transport de MPls (16 ± 6 µm) pour déterminer les paramètres de sorption et les efficacités de rétention. Les expériences ont été menées à différents débits (31 ml min-¹ et 65 ml min-¹) pour évaluer l'impact du débit sur la dynamique de sorption et l'efficacité de la filtration. La modélisation numérique à l'aide de MT3DMS et MODFLOW a fourni des informations supplémentaires sur le transport des MPl et la cinétique de sorption dans les milieux poreux. Des analyses de sensibilité ont permis d'évaluer les effets des différents paramètres de sorption.

L'impact du débit sur la sorption a été exploré, révélant des variations dans les paramètres de sorption tels que le coefficient de distribution (K_d), le coefficient de transfert de masse (β) et le taux de sorption irréversible (K_1). Les débits relativement faibles étaient associés à des valeurs Kd et β plus élevées, indiquant une sorption accrue et des taux de transfert de masse modifiés. L'augmentation de Kd a conduit à une sorption plus graduelle et à un retard accru, tandis que les changements de β ont affecté le rythme de la sorption et la concentration maximale. Le débit a également influencé la masse retenue, des débits plus élevés entraînant une diminution de l'efficacité de la rétention, ce qui indique la prédominance de l'advection sur la rétention. Les taux de rétention ont été évalués à différents débits, montrant des taux de rétention moyens de 28 ± 1 % et 24 ± 2 % pour la modélisation numérique et les mesures expérimentales à un débit de 31 ml min-¹, et de 17 ± 1 % et 9 ± 4 % respectivement à un débit de 65 ml min-¹. L'erreur absolue moyenne (MAE) de 6 % indique de légères différences entre les taux de rétention prédits et mesurés.

L'étude a permis de combler des lacunes importantes dans les connaissances relatives à la dynamique du transport des MPl polydispersés, de type fragmentaire et de non-référence dans les milieux poreux. En élucidant le rôle de la cinétique de sorption et du débit sur l'efficacité de la filtration, l'étude contribue au développement de stratégies visant à atténuer la contamination par les MPl dans les systèmes d'eaux souterraines. Les résultats de l'étude ont révélé que le débit influençait de manière significative la dynamique de sorption, des débits plus faibles étant associés à des taux de sorption et des efficacités de rétention plus élevés. L'utilisation de modèles numériques a permis d'estimer avec précision les taux de rétention, avec toutefois de légères différences par rapport aux mesures expérimentales. Ces résultats soulignent l'importance de prendre en compte des facteurs tels que le débit, la présence de tensioactifs et les caractéristiques des particules pour comprendre le transport des MPl dans les milieux poreux. Il est essentiel de comprendre cette dynamique pour développer des stratégies de filtration efficaces afin de préserver les ressources en eau douce. Les études futures pourraient envisager de modifier les propriétés de l'eau pour mieux imiter les systèmes naturels, ce qui contribuerait à améliorer la protection des sources d'eau douce et le développement de stratégies visant à sauvegarder ces ressources vitales.

Chapitre 5 : Rétention et transport de nanoplastiques avec différentes fonctionnalités de surface dans un système de filtration sur sable

Okutan, H.; Hul, G.; Stoll, S.; Le Coustumer, P. Retention and Transport of Nanoplastics with Different Surface Functionalities in a Sand Filtration System. Nanomaterials 2024, 14, 32. https://doi.org/10.3390/nano14010032

Les nanoplastiques (NPls) posent des problèmes importants dans les échantillons environnementaux, en particulier dans les stations d'épuration des eaux (STEP), où leur élimination est cruciale pour préserver la qualité de l'eau potable. Toutefois, la détection et la différenciation des NPls des autres polluants dans les échantillons naturels restent problématiques en raison de leur petite taille (moins de 1 µm) et de l'absence de méthodes de détection normalisées. Parmi les différents procédés de traitement des STEP, la filtration sur sable joue un rôle essentiel dans l'élimination des contaminants dissous et particulaires. Malgré son efficacité, des études ont montré que la filtration sur sable peut ne pas éliminer les NPls de moins de 1 µm, ce qui souligne la nécessité de mieux comprendre leurs mécanismes de rétention et de transport. Pour combler cette lacune, des expériences de filtration sur sable en laboratoire ont été menées pour reproduire des conditions similaires à celles des stations d'épuration de Genève, en Suisse. Des NPls de polystyrène avec des groupes fonctionnels amidine positifs ([A-PS]+) et des NP de polystyrène sulfate avec des groupes fonctionnels sulfate négatifs ([S-PS]-) ont été utilisées. L'impact de la fonctionnalité de surface, de la variation de la concentration des NPls, ainsi que de la présence de surfactants dans l'enrobage des [A-PS]+ et des formes en solution, sur l'adsorption et la désorption des NPls dans les milieux poreux a été étudié.

Les résultats expérimentaux ont révélé que les charges de surface des NPls, influencées par diverses fonctionnalités de surface ou par des revêtements de molécules tensioactives, affectaient de manière significative leur comportement de rétention dans les milieux poreux. Les forces d'interaction électrostatique ont joué un rôle majeur, les NPls présentant des efficacités de rétention distinctes en fonction de leurs charges de surface. Les efficacités de rétention des NP ont été classées comme suit : fonctionnalisées avec de l'amidine [A-PS]+ > avec du sulfate [S-PS]- > avec de l'amidine enrobée de tensioactifs [SDS-A-PS]-. Les hétérogénéités de charge ont fait que les particules chargées négativement se sont attachées aux coins des minéraux argileux, tandis que les particules chargées positivement se sont attachées aux minéraux de quartz. En outre, les mesures du potentiel ζ ont indiqué une augmentation notable de la rétention des particules chargées positivement avec l'augmentation des concentrations, alors que l'effet sur les particules chargées négativement était moins prononcé. Avec l'injection de surfactant dans le filtre à sable contenant des NPls [A-PS]+ adsorbées, une inversion de charge s'est produite, entraînant le transport des particules chargées positivement présentes dans le milieu dans un état chargé négativement et a conduit à la remobilisation des NPls, mettant en évidence le transport potentiel dans les phases de traitement ultérieures.

L'analyse de la dimension fractale à partir de l'imagerie microscopie électronique en transmission (MET) a permis de mieux comprendre les propriétés d'agrégation, les agrégats de plus petite taille étant associés à des efficacités de rétention moindres. Les caractéristiques des agrégats se sont

révélées être en corrélation avec les efficacités de rétention. Les NPl [A-PS]+ formaient des agrégats plus compacts, conduisant à des efficacités de rétention plus élevées.

Les manipulations ont été effectuées dans les laboratoires de l'Université de Genève, en Suisse. Seule l'imagerie TEM a été réalisée au centre d'imagerie de Bordeaux, en France.

Ces résultats soulignent l'importance de la filtration sur sable dans les stations d'épuration, qui sert de barrière protectrice contre les particules en suspension et contribue à des pratiques de traitement de l'eau rentables et respectueuses de l'environnement. Il est essentiel de comprendre les effets de rétention des NPls dans les filtres à sable pour améliorer les performances de ces derniers et orienter la recherche sur l'amélioration de la rétention à d'autres stades du traitement. Pour aller de l'avant, l'exploration du développement de médias de filtres à sable qui imitent étroitement les conditions environnementales naturelles constitue une piste de recherche intrigante. En outre, l'étude de l'impact d'autres contaminants sur les comportements de rétention et de transport des NPls mérite d'être approfondie afin de garantir des stratégies complètes de traitement de l'eau.

L'étude met en lumière l'interaction complexe entre les fonctionnalités de surface, les surfactants et les milieux poreux qui influencent la rétention et le transport des NPls dans les systèmes de filtration sur sable. Ces connaissances contribuent non seulement à améliorer l'efficacité de la filtration sur sable dans l'élimination des NPls, mais aussi à informer le développement de stratégies de traitement de l'eau plus efficaces pour préserver la qualité de l'eau potable.

Conclusion

L'objectif de ce travail de thèse était d'étudier et de comprendre le comportement et le devenir des MPls et des NPls dans les milieux poreux saturés. Les milieux poreux désignent des substances géologiques, telles que le sable, le gravier, le sol, les roches fissurées, le grès et le calcaire karstique, caractérisées par des espaces vides permettant l'écoulement de l'eau. Invariablement, ces cas présentent une combinaison de matrices solides et d'espaces vides dans leurs domaines. Dans le cadre de cette thèse, les milieux poreux saturés ont été associés à la phase de filtration du sable dans les usines de traitement de l'eau potable et aux réservoirs d'eau dans les nappes phréatiques souterraines, qui sont tous deux d'importantes sources d'eau douce. L'ensemble des études met en lumière la relation complexe entre les MNPls, les caractéristiques des milieux poreux et les facteurs environnementaux. Cela souligne le besoin crucial de comprendre la dynamique du transport et l'efficacité de la rétention afin de développer des stratégies d'atténuation efficaces et de protéger les ressources en eau.

La phase initiale de la recherche englobe l'association des MNPls avec divers types de milieux poreux afin d'établir des corrélations pertinentes pour la protection des ressources en eaux souterraines. Des équations mathématiques ont été utilisées pour décrire l'écoulement et le transport des contaminants MPls. L'accent a été mis en particulier sur les expressions mathématiques décrivant le mouvement de l'eau et des contaminants dans les espaces vides des milieux poreux saturés. Après avoir acquis un modèle mathématique adapté à des scénarios spécifiques, la solution subséquente, qu'elle soit analytique ou numérique, donne des indications précieuses sur la

dynamique de l'écoulement des fluides et le comportement des MPls dans les matériaux poreux géologiques examinés.

Dans un premier temps (chapitre 3), les modèles analytiques ont été examinés, en mettant l'accent sur la résolution du principal problème posé par la distribution unique de la taille et de la forme des MPls, telle qu'elle a été identifiée dans la littérature récente. Les paramètres hydrodynamiques tels que la porosité et la dispersivité de divers milieux poreux ont été déterminés à l'aide de traceurs conservateurs et, par la suite, ces paramètres ont été comparés à ceux obtenus à partir du transport de MPls. Les deux scénarios de transport ont été traités par des approches analytiques utilisant des techniques de modélisation inverse. Grâce à des expériences impliquant divers milieux poreux et des débits contrôlés dans des expériences en colonne, l'étude élucide l'impact de la vitesse moyenne sur le transport des particules, en soulignant l'importance des contraintes liées à la taille des pores et des distributions de porosité asymétriques.

Dans l'examen ultérieur du transport des MPls (chapitre 4), la complexité des formulations mathématiques s'est accrue, ce qui a conduit à l'adaptation des solutions numériques. Cette approche numérique a permis de mieux comprendre le transport des MPls à travers le sable de quartz, en mettant l'accent sur les paramètres de sorption réversibles et irréversibles pour des débits variables. Grâce aux expériences et aux simulations numériques, l'étude met en évidence l'interaction entre la cinétique de sorption, la dynamique de l'écoulement et les caractéristiques des particules. Cela donne des indications précieuses sur l'efficacité de la filtration et la dynamique de la rétention. La validation du modèle numérique par rapport aux résultats expérimentaux a montré une différence mineure d'environ 6 %, ce qui indique que le modèle numérique adapté, dérivé de la théorie du transport des solutés, est approprié pour modéliser le transport des MPls.

Dans l'étude du devenir des NPls dans l'eau propre (chapitre 5), l'accent a été mis sur l'analyse de la phase de filtration sur sable dans les stations d'épuration industrielles, qui est cruciale pour assurer l'approvisionnement en eau propre. Ici, l'accent a été mis non plus sur les paramètres hydrodynamiques, mais sur les propriétés physiques et chimiques des NPls, qui influencent leur transport et leur comportement à travers les filtres à sable. Les filtres à sable utilisés dans l'étude étaient constitués de sable de quartz saturé provenant de la STEP de Genève, en Suisse. Les conditions de débit ont été normalisées pour reproduire les opérations dans les STEP, tandis que des variations dans la concentration de NPls et les propriétés de la surface ont été introduites. Les recherches sur le comportement d'adsorption et de désorption des NPls ont porté sur la taille, le potentiel zêta, la concentration, la microscopie électronique et le traitement d'images. Grâce à des expériences en laboratoire reproduisant les conditions opérationnelles, l'étude met en lumière l'impact des fonctionnalités de surface et des surfactants sur la rétention et le transport des NPls dans les milieux poreux. En clarifiant la relation complexe entre les charges de surface, les propriétés d'agrégation et l'efficacité de la filtration, la recherche souligne l'importance d'améliorer les pratiques de filtration sur sable, qui sont des composants essentiels des stations d'épuration industrielles.

Collectivement, ces études mettent en évidence la nature interdisciplinaire de la recherche sur la pollution plastique et soulignent l'importance des efforts de collaboration dans l'élaboration de

solutions globales. En intégrant des approches expérimentales, la modélisation numérique et des cadres théoriques, ces études font progresser notre compréhension de la dynamique du transport des matières plastiques dans les milieux poreux et fournissent des informations cruciales pour éclairer les décideurs politiques et mettre en œuvre des mesures d'atténuation de la pollution.

To my dear husband…

ACKNOWLEDGMENT

I am grateful to my thesis directors, Mr. Bedri Kurtuluş and Mr. Philippe Le Coustumer, whose invaluable guidance and suggestions have been instrumental in the completion of this thesis. Their support, along with their unwavering belief in my abilities throughout my academic journey, have been incredibly motivating.

My PhD journey commenced at Muğla Sıtkı Koçman University, Türkiye, under the direction of Mr. Bedri Kurtuluş. He not only paved the way for me at the outset of my academic career but also encouraged me to go one step further. He guided me in forming connections to demonstrate the effectiveness of discussions and negotiations in resolving challenges. Mr. Philippe Le Coustumer's offer granted me the opportunity to become a doctoral candidate at the University of Bordeaux Montaigne, France. He was a steady presence during times when I felt overwhelmed by seemingly hopeless difficulties. His support has been evident through both words of reassurance, and practical actions that were always geared towards finding solutions. Interactions with him consistently enriched my academic outlook. He actively sought solutions, creating opportunities, and introduced me to individuals who expanded my academic horizons.

I extend my sincere gratitude to Mr. Moumtaz Razack for his support and guidance, enriching my studies with his knowledge and expertise. His mentoring provided me with the necessary environment to conduct my experiments, and his supervision were instrumental in both the hydrogeological modeling and experimental phases of my research.

I would like to thank Mr. Emrah Pekkan for his supervision and support in conducting my experiments at Eskişehir Technical University, Earth and Space Sciences Institute, and to Mr. Hasan Burak Özmen and Mr. Fatih Öztürk from the laboratory team for their assistance and support in the laboratory studies.

I wish to express my heartfelt appreciation to Mr. Serge Stoll. It has been a pleasure to meet him, and I am deeply grateful for his support, kindness and accessibility. His supervision proved invaluable throughout my collaboration with him and his team, the environmental physical-chemistry group at the University of Geneva, offering fresh and diverse perspectives at every stage of our work together.

I extend my sincere gratitude to Mr. Paul Sardini and Mr. Laurent Caner, the coordinators of the Hydrogeology and Transfer Master 2 program, for providing me the opportunity to participate in the Master 2 courses at the University of Poitiers. Additionally, I would like to express my appreciation to Mr. Jacques Bodin and Mr. Gilles Porel for their training in field and laboratory work related to pollution transport and groundwater modeling. The knowledge and skills I gained from these courses have proven invaluable at every stage of my PhD studies.

I would like to extend my gratitude to the team of the Bordeaux Imaging Center at University of Bordeax, particularly Mr. Etienne Gontier, Mrs. Sabrina Lacomme, Mr. Fabrice Cordelieres, and

Mr. Guillaume Maucort, for the invaluable training they provided me. Their warmth and kindness made the learning process a delightful experience.

I extend my gratitude to the personnel of the Geological Engineering Department and Institute of Science at Muğla Sıtkı Koçman University for their assistance in administrative processes. I present my many thanks to Mr. Murat Gül, Mr. Zeki Bora Ön, and Mr. Ergün Karacan for their courses.

I would like to thank Mrs. Sylvia Abram and the personnel of the *Ecole Doctorale Montaigne-Humanités* at the University of Bordeaux Montaigne for their warm welcome and support.

I would like to also thank Mrs. Vera Sandoval from the Academic Exchange Office of the University of Geneva. Her assistance with the administrative processes for the Excellence Scholarship program, through which I had the opportunity to study at the University of Geneva, was invaluable.

I am honored by the acceptance of Mr. Frederic Huneau and Mr. Mohammed Baalousha to agree to take on the role of reviewers for this thesis. I extend my heartfelt appreciation to Mr. Moumtaz Razack, Mrs. Sena Akçer-Ön, Mr. Emrah Pekkan, and Mr. Serge Stoll for agreeing to participate as members of the defense jury. Additionally, I am grateful to Mrs. Özlem Yağbasan for her participation in my thesis monitoring committees and for sharing her constructive comments.

I would like to express my gratitude to the French Embassy scholarship program and its implementer Campus France for granting me a scholarship for three years of my PhD studies. Additionally, I extend my thanks to the Sıtkı Koçman Foundation for their support during the initial two years of this scholarship. I am also appreciative of the Turkish Higher Education Council (YOK) and the Institute of Science at Mugla Sitki Kocman University for granting me the YOK 100/2000 doctoral scholarship.

I would like to extend sincere gratitude to Esan Eczacıbaşı Industrial Raw Materials Co. (Türkiye) for their generous support with earth materials.

I extend my gratitude to my colleagues from the environmental physical-chemistry group at the University of Geneva, Gabriela Hul, for her collaborative spirit and shared insights into our studies, Angel Negrete Velasco for his expertise in FTIR analysis, and Fanny Berset for enjoyable coffee and lunch breaks together.

I extend my sincere appreciation to my colleague Çağdaş Sağır for his support throughout my studies at the University of Poitiers and Eskisehir Technical University. His assistance during both the experimental and writing phases, as well as during academic and administrative challenges, have been invaluable. I fondly recall his meticulous measurements, which were as precise as a precision balance, and how they facilitated our experiments with a smile.

I am deeply grateful to my mother, Ayşe Gül Yeşilmaden, and my father, Semih Yeşilmaden, for their boundless support. Their love and pride in me have been a constant source of warmth and encouragement, filling my heart with gratitude and strength. My dear little sister, Zeynep Yeşilmaden, has always been by my side, offering support and companionship. She has been not only a constant presence but also my personal graphic designer, dedicating her time and talent to ensure my needs were met. I am immensely grateful to her for always prioritizing me. My dear

grandmother Türkan Can, before my graduation, she awarded me the title of Dr. and always believed in my success wholeheartedly, thank you for being there, I'm grateful.

Lastly, my deepest and most profound gratitude goes to my beloved husband, Cihan Okutan, for his unwavering love and support. I have always felt like the center of his world. His belief in me and his consistent encouragement have allowed me to shine brightly. Together, we have navigated challenges, finding solutions side by side. His optimism was a source of comfort and strength throughout our journey together. We have walked hand in hand to reach this point, and his presence is my greatest happiness. Thank you for everything, my dear darling.

TABLE OF CONTENTS

RESUME ..... **ii**
ACKNOWLEDGMENT ..... **xi**
TABLE OF CONTENTS ..... **xiv**
LIST OF TABLES ..... **xviii**
LIST OF FIGURES ..... **xx**
CHAPTER 1 - INTRODUCTION **1**
1.1. Thesis Objectives 1
1.2. Overview: Fate and Behavior of MNPs through Porous Media 2
1.3. List of Publications 7
CHAPTER 2 - MATERIALS AND METHODS **9**
2.1. Materials 9
2.1.1. Polyethylene Microplastics 9
2.1.2. Polystyrene Nanoplastics 10
2.1.3. Porous Media 14
2.1.4. Fluorescent Dyes 17
2.1.5. Surfactants 18
2.2. Methods 18
2.2.1. Column experiments 18
2.2.1.1. Experimental Procedure 18
2.2.1.2. One dimensional analytical and numerical modeling 22
2.2.2. Constant Head Permeameter Experiment 27
2.2.3. Retention Efficiency 27
2.2.4. Z-Average Hydrodynamic Diameter Measurements 28

2.2.5 Zeta Potential Measurements 29

2.2.6. Electron Microscopy 30

2.2.7. Fractal Dimensions 31

2.2.8. Spectroscopic Measurements 31

Annex 2.A – Method diagram for the Experiments with PE-1 35

Annex 2.B – Method diagram for the Experiments with PE-2 36

Annex 2.C – Method diagram for the Experiments with NPls 37

CHAPTER 3 - ONE-DIMENSIONAL EXPERIMENTAL INVESTIGATION OF POLYETHYLENE MICROPLASTIC TRANSPORT IN HOMOGENEOUS SATURATED MEDIUM 38

3.1. Summary 38

Abstract 40

3.2. Introduction 41

3.3. Material and Method 44

3.3.1. Properties of the PE Particles 44

3.3.2. Properties of the Porous Medium Materials 45

3.3.3. Fluorescent Tracer Column Tests 47

3.3.4. Microplastic Tracer Column Tests 50

3.4. Results and Discussion 53

3.4.1. Fluorescent Tracer Column Tests 53

3.4.2. Microplastic Tracer Column Tests 54

3.5. Conclusion 57

Annex 3.A. Supplementary Information 59

CHAPTER 4 - UNDERSTANDING MICROPLASTICS RETENTION EFFICIENCY AND SORPTION DYNAMICS IN POROUS MEDIA 62

4.1. Summary 62

Abstract 64

4.2. Introduction 65

4.3. Materials and Methods 66
4.3.1. Materials 66
4.3.2. Methods 68
4.3.2.1. Permeameter Experiments 68
4.3.2.2. Transport Experiments 69
4.3.2.3. Retention Efficiencies 71
4.3.2.4. Sensitivity Analyses 72
4.4. Results and Discussions 72
4.4.1. Permeameter Experiments 72
4.4.1.1. Transport Experiments 73
4.4.1.2. Retention Efficiencies 75
4.4.1.3. Sensitivity Analyses 76
4.5. Conclusion 78
Annex 4.A. Supplementary Information 80
CHAPTER 5 - RETENTION AND TRANSPORT OF NANOPLASTICS WITH DIFFERENT SURFACE FUNCTIONALITIES IN A SAND FILTRATION SYSTEM 84
5.1. Summary 84
Abstract 86
5.2. Introduction 87
5.3. Materials and Methods 89
5.3.1. Materials 89
5.3.2. Methods 90
5.3.2.1. Z-Average Hydrodynamic Diameter and Zeta (ζ) Potential Measurements 90
5.3.2.2. Turbidity Measurements 91
5.3.2.3. Scanning Electron Microscopy (SEM) and Transmission Electron Microscopy (TEM) Imaging 91
5.3.2.4. UV-Vis Spectrophotometry 91

5.3.2.5. Column Experiments 92
5.3.2.6. Aggregate Assessment with Fractal Dimension 92
5.4. Results 93
5.4.1. Characterization of NPls with Different Surface Functionalities 93
5.4.2. NPls Transport and Retention Behavior in Sand Filter 94
5.4.2.1. Effects of Injection Concentration 95
5.4.2.2. Effect of the NPls Surface Properties 97
5.4.3. Effects of Surfactant Coating 99
5.4.4. Remobilization 100
5.4.5. Aggregate Properties 101
5.4.6. Summary of Mechanism 103
5.5. Conclusions 104
Annex 5.A. Supplementary Information 106
6. CONCLUSIONS AND PERSPECTIVES 118
REFERENCES 122

LIST OF TABLES

Table 2.1. General descriptive statistics of PE-1 and PE-2 MPls. Units are in µm 10
Table 2.2. General descriptive statistics of size measurements of NPls with TEM. Units are in nm. 11
Table 2.3. Z-average hydrodynamic diameter (nm) and zeta potential (mV) measurements of NPls (pH = 3 ± 0.1)..... 11
Table 2.4. General descriptive statistics of the grain size of the porous medium materials. 14
Table 2.5. General descriptive statistics of the pores size of the porous medium materials. 15
Table 2.6. The sieve analysis measurements for quartz sand. 16
Table 2.7. The properties of size and shape of quartz sand grains. 17
Table 2.8. Parameters of the tests with PE-1..... 19
Table 2.9. The flow rates (Q) and injected tracer volumes (Vinj) for the fluorescent tracer tests. 20
Table 2.10. The flow rates (Q) and injected tracer volumes (Vinj) for the PE-2 and fluorescent tracer tests. 20
Table 3.1. General descriptive statistics of the grain size of the used PE, in µm. 44
Table 3.2. General descriptive statistics of the pores size of the porous medium materials. 46
Table 3.3. General descriptive statistics of the grain size of the porous medium materials. 47
Table 3.4. The flow rates (Q) and injected tracer volumes (Vinj) for the fluorescent tracer tests. 48
Table 3.5. Parameters of the tests with PE. 52
Table 3.6. Fluorescent tracer column test results: Recovered Mass, Mrec (µg) 53
Table 3.7. Fluorescent tracer column test results: the kinematic porosity (nk) and dispersivity (α) values for the mediums. 54
Table 3.8. The calculated values of the parameters for the plastic particle experiment P2 for coarse gravel. 56
Table 3.S1. Parameters of the experimental setups for the fluorescent tracer tests. 60
Table 4.1. The statistical properties of MPls size distribution (All the values are given in µm)... 67
Table 4.2. Hydraulic conductivity (K) values corresponding to each experimental series. (For the A series, tracer experiments were conducted at a flow rate of 31 ml min^{-1}, while for the B series, tracer experiments were conducted at a flow rate of 65 ml min^{-1}.) 73
Table 4.3. The dye experiment results for porosity (θ), dispersivity (α), distribution coefficient (Kd), and mass transfer rate (β) values. 73

Table 4.4. The computed parameters for distribution coefficient (Kd), , and mass transfer rate (β) , and irreversible kinetic sorption rate (K1) were determined for each flow rate, with the C/C0 peak representing the ratio of MPls concentration at the peak point. 75

Table 4.5. The numerically calculated retention rates for each experiment, varying according to the flow rate, are shown as R1, while the experimentally measured retention rates are indicated as R2.....75

Table 4.6.The retention efficiency values calculated numerical solution due to change in irreversible kinetic sorption rate (K1).....77

Table 4.7. The retention efficiency values calculated numerical solution due to change in flow rates, Q, with constant sorption parameters which are distribution coefficient (Kd), mass transfer rate (β), and irreversible kinetic sorption rate (K1). The sorption parameters of experiment MPl A, conducted at a flow rate of 31 ml min^{-1}, remained constant. 78

Table 4.S1. Particle size classification of MPls (adapted from (ISO 24187, 2023)) 80

Table 5.1. Summary of injection conditions, maximum effluent concentrations (MEC), and retained mass values. 95

Table 5.2. Total recovered mass from the experiments and the percentage of this total mass recovered after [A-PS]+ injection and SDS injection are shown. Recovered mass 1 represents the recovered mass percentage after NPL injections. Recovered mass 2 represents the recovered mass percentage after SDS solution injection, which is expected to cause remobilization of the sorbed NPls The total recovered mass percentage shows the recovered percentage according to initial conditions after both injections.....100

Table 5.3. The overall presentation of retention efficiency and fractal dimension values. 103

Table 5.S1. Sand grains characteristics determined with Camsizer (Retsch). Sand grains belong to 11 granulometric classes and mainly have sizes comprised between 2.38 and 2.83 mm, 2.83 and 3.36 mm as well as between 3.36 and 4.00 mm. They are of ellipsoidal shape, with an average width-to-length ratio equal to 0.655, and their surfaces are rather heterogenous, with an average roughness equal to 0.826 and an average convexity close to 1. 107

Table 5.S2. Statistical parameters for NPls from the TEM image measurements in “nm” unit (pH = 3 ± 0.1).....113

Table 5.S3. Statistical parameters for NPls from the TEM image measurements in “nm” unit (pH = 3 ± 0.1).....113

Table 5.S4. Summary of injection conditions, maximum effluent concentrations (MEC), and retained mass values for intermediate concentration conditions. 114

LIST OF FIGURES

Figure 2.1. PE-1 (blue line) and PE-2 (black line) spectra acquired by FTIR. 9

Figure 2.2. The size distrubiton histogram of PE-1 (a) and PE-2 (b) MPls. 10

Figure 2.3. Optical microscopy image of PE-1 (a) and PE-2 (b). 10

Figure 2.4. (a, b) [A-PS] + (a, b), [S-PS]- (c, d) and [SDS-A-PS]- (e, f) NPls (white arrows) size distribution and histogram which was measured from TEM micrography (pH = 3 ± 0.1) 12

Figure 2.5. Size and ζ potential titration curves for (a) [A-PS]+ and (b) [S-PS]- 13

Figure 2.6. The critical concentrations of SD) exhibited variations across different concentrations of [A-PS]+ NPls (Conditions: ultrapure water.). 14

Figure 2.7. The particle size distribution histogram for the large silica balls (a), small silica balls (b), sand (c) and coarse gravel (d) and the pore size distribution histogram for the large silica balls (e), small silica balls (f), sand (g) and coarse gravel (h). 15

Figure 2.8. The experimental setup for the PE-1 MPls tests (a) is the actual setup and (b) is the schematic illustration of setup. X signifies the length of the porous medium, R1 (0.3 cm) denotes the radius of the joint pipes, and R2 (8 cm) represents the radius of the column (Location: University of Poitiers, France). 19

Figure 2.9. The experimental setup for the PE-2 MPls tests (a) is the actual setup and (b) is the schematic illustration of the setup (Location: Eskişehir Technical University, Türkiye). 21

Figure 2.10. The experimental setup for the NPls tests (a) is the actual setup and (b) is the schematic illustration of setup (Location: University of Geneva, Switzerland) 22

Figure 2.11. The calibration curves for PE-2 MPl experiments were used as plotting curves. NTU is the unit of turbidity. (a) corresponds to MPl C, (b) corresponds to MPl D, (c) corresponds to MPl E, and (d) corresponds to MPl G experiments. 32

Figure 2.12 The calibration curves are employed to convert NTU measurements to concentration, and these curves are specialized for different types of NPls. Specifically, (a) is used for [A-PS]+, (b) is used for [S-PS]-, and (c) is used for [A-SDS-PS]- NPls experiments. . 32

Figure 2.13. The calibration curve to calculate the concentration of PE-1 MPls from fluorometer measurements. 33

Figure 3.1. The grain size histogram of the used PE. 44

Figure 3.2. SEM micrographs of the MP: (A) shape and size distribution; (B) detail of rugged PE particles. 45

Figure 3.3. The porous medium materials for the column tests: (A) large silica balls; (B) small silica balls; (C) sand; (D) coarse gravel 46

Figure 3.4. Experiment setup for the fluorescent tracer tests. 47
Figure 3.5. Experiment setup for the microplastic tests. 51
Figure 3.6. The equation for the inversion of the fluorometer measurements to PE concentrations. 52
Figure 3.7. BTCs of plastic particle experiment P2 for coarse gravel 56
Figure 3.S1. The pore size histograms for the used porous medium materials. 59
Figure 3.S2. The grain size histograms for the used porous medium materials. 60
Figure 3.S3. The experimental and the analytical fluorescent tracer concentration BTCs for each medium and each column test: (A) large silica, (B) small silica, (C) sand, and (D) coarse gravel 61
Figure 4.1. The histogram of the size distribution (a) and the optical microscopy image (b) of MPls. 67
Figure 4.2. The grain size distribution curve of sand. 68
Figure 4.3. The breakthrough curves observed and computed data for low (a) and high (b) flow rates. In each plot, the y-axis is denoted as C/C0, while the x-axis corresponds to pore volume. 74
Figure 4.4. The BTCs of the sensitivity simulations for the distribution coefficient, Kd (a), mass transfer rate, β (b), and kinetic sorption rate, K1 (c), were analyzed. The computed BTCs of the MPl A and DYE A experiments are represented by a blue line and a red line, respectively. In the legend, the parameters are listed in the order of Kd, β, and K1. (This sensitivity analyses corresponds to MPl A experiments where 1 pore volume is equal to 1688 ml) 77
Figure 4.S1. The calibration curves for dye experiments which were used for plotting BTCs. (a) is for DYE A, (b) is for DYE A.1, (c) is for DYE B and (d) is for DYE B.1 experiments 80
Figure 4.S2. The calibration curves for MPl experiments which were used plotting curves. NTU is the unit of turbidity. (a) is for MPl A, (b) is for MPl A.1, (c) is for MPl B and (d) is for MPl B.1 experiments 81
Figure 4.S3. The BTCs of the sensitivity simulations for the distribution coefficient, Kd (a), mass transfer rate, β (b), and kinetic sorption rate, K1 (c), were analyzed. The computed BTCs of the MPl B and DYE B experiments are represented by a blue line and a red line, respectively. In the legend, the parameters are listed in the order of Kd, β, and K1. (This sensitivity analyses corresponds to MPl B experiments where 1 pore volume is equal to 1678 ml) 82
Figure 4.S4. The BTCs of the sensitivity simulations for the flow rates were analyzed. The computed BTCs of the MPl B experiment are represented by a blue line. In the legend, the parameters are listed in the order of Kd, β, and K1. (This sensitivity analyses correspond to MPl A experiments where 1 pore volume is equal to 1688 ml). 83
Figure 5.1. Breakthrough curves for 100 mg/L, 500 mg/L, and 1000 mg/L injection concentration (C0) are shown for [A-PS]+ (a), [S-PS]− (b), and [SDS-A-PS]− (c) NPls 95

Figure 5.2. SEM micrography from the sand grain collected after the transport experiment. (a) Attachment of [A-PS]+ NPls onto the quartz surface and (b) attachment of [S-PS]− NPls onto clay minerals (white arrows).....96

Figure 5.3. Collective representation of hydrodynamic diameter and zeta (ζ) potential vs. PV graphs of experiments performed with [A-PS]+ (a,b), [S-PS]− (c,d), and [SDS-A-PS]− (e,f).....97

Figure 5.4. ζ potential measurements (a) and z-average hydrodynamic diameter (b) of effluents. The dashed line represents the SDS solution injection.....101

Figure 5.5. Fractal analyses results for each concentration, type of NPL, and desorbed sample. Three images of aggregates were used for each condition. 103

Figure 5.6. The schematic overview depicts the transport and retention process of NPls within a sand filtration column which is quartz sand and characterized as a saturated porous medium. Panels (a), (b), and (c) illustrate the retention efficiencies for [A-PS]+, [S-PS]−, and [SDS-A-PS]− NPls, respectively. Panel (d) presents the re-mobilization of adsorbed [A-PS]+ upon the introduction of an SDS solution.....104

Figure 5.S1. SDS critical concentrations for different polystyrene amidine latex nanoplastics concentrations. Experimental conditions: ultrapure water. 106

Figure 5.S2. The calibration curve which has relation between absorbance and concentration of fluorescein sodium salt. 108

Figure 5.S3. The experimental breakthrough curve and Model breakthrough curve after fitting procedure. The dye tracer experiment is duplicated. 109

Figure 5.S4. The calibration curves which presents relation the concentration and turbidity measurements for [A-PS] + (a), [S-PS]- (b) and [SDS-A-PS]- (c).....110

Figure 5.S5. The schematic illustration of used experimental setup.....111

Figure 5.S6. Size and ζ potential titration curves for (a) [A-PS]+ and (b) [S-PS]-. 112

Figure 5.S7. (a, b) [A-PS] + (c, d) [S-PS]- (e, f) [SDS-A-PS]- NPls (white arrows) size distribution which was measured from TEM micrography (pH = 3 ± 0.1).....113

Figure 5.S8. Observed breakthrough curves for 100 mg/L, 150 mg/L, 200 mg/L, 500 mg/L and 1000 mg/L injection concentration (C0) are shown for (a) [A-PS]+ (b) [S-PS]-.....114

Figure 5.S9. Collective representation of hydrodynamic diameter and ζ potential vs PV graphs of experiments performed with [A-PS]+ (a, b), [S-PS]- (c, d) and [SDS-A-PS]- (e, f) for all effluents. 115

Figure 5.S10. The breakthrough curves of adsorption and desorption experiments with 100 mg/L (a), 500 mg/L (b) and 1000 mg/L (c) [A-PS]+ injection. The dash line represents the SDS injection. 116

Figure 5.S11. Log-Log pilot of X axis is the ratio of the box size to the image size and Y axis is the number of pixels counted in per box for [A-PS]+ 500 mg/L injection conditions. (b) The TEM image of the [A-PS]+ NPls' homoaggregate (blue arrow) was used for Df calculation. 117

CHAPTER 1 - INTRODUCTION

1.1. Thesis Objectives

Through a multidisciplinary approach integrating experimental investigations, analytical and numerical modeling, and environmental monitoring, this study seeks to advance our understanding of Microplastics (MPls) and Nanoplastics (NPls) transport and retention phenomena in porous media, elucidate their interactions with groundwater environments and industrial Drinking Water Treatment Plants (DWTPs) with the perspective of sand filter efficiency and contribute to the development of science-based solutions for mitigating plastic pollution and safeguarding freshwater resources for present and future generations.

Chapter 1 is an overview and highlights various physical and chemical variables influencing the behavior of Microplastics and Nanoplastics (MNPls) within porous media. **Chapter 2** provides a comprehensive overview of the materials and methodologies employed in this study. Detailed explanations of the experimental procedures and their theoretical underpinnings are provided to ensure clarity and understanding.

The investigations in **Chapter 3** commenced with an exploration into the hydrodynamic transport parameters within saturated porous media, using fluorescent tracer techniques understanding porous media properties. Existing analytical solutions for solute transport were employed and tested to assess their suitability for modeling the transport of MPls. This involved conducting one-dimensional column experiments, incorporating both a conservative tracer (fluorescein) and a polyethylene (PE) MPls with a size of 200-500 µm. Subsequently, analytical solutions were implemented, selecting appropriate equations based on the injection method: instantaneous for fluorescein and finite-duration for PE MPls. Finally, an inverse solution approach was used to extract the hydrodynamic parameters specific to the transport of MPls through the porous media from the analytical solutions.

In **Chapter 4**, the complexity of employing smaller porous media and MPls is addressed, necessitating a thorough numerical solution over analytical methods. This section of the thesis is dedicated to investigating the filtration capacity of porous media, specifically focusing on the transport of PE-type MPl particles, with a size of 16 ± 6 µm, within a saturated quartz sand-type porous medium. Similarly, in the previous section, fluorescent dye was employed to establish the hydrodynamic properties of the sand. Furthermore, the study aims to assess filtration efficiency using numerical models derived from flow and transport equations. This investigation involves determining sorption parameters through reversible and irreversible kinetic sorption models,

quantifying retention efficiencies, and examining the impact of flow rate variations on the transport phenomena.

Chapter 5 is driven by the foundational hypothesis that the effectiveness of sand filtration in retaining NPls is influenced by their surface functionalities, an influence further modulated by the presence of surfactants in the filtration system. Experimental conditions were adapted from the sand filtration system of the industrial drinking water treatment plant (DWTP) in Geneva, Switzerland. They were then replicated under laboratory conditions with similar sand and flow rates to address gaps in existing studies regarding the retention dynamics and efficiency of sand filtration for NPls. The aim was to investigate the retention efficiency of the DWTP's sand filtration system in the presence of various surface functional groups, coatings, and concentrations of polystyrene (PS) NPls. Furthermore, the impact of surfactants on both adsorption and desorption processes was explored. Additionally, the homoaggregation properties were assessed using an unconventional method known as fractal dimension analysis, which is not commonly employed in studies focusing on plastic retention efficiency following sand filtration approaches.

Comprehending the mechanisms governing the transport of MPls and NPls through porous media is crucial. It helps clarify their environmental fate and ecological impacts, informs risk assessment and management strategies, and safeguards the integrity of freshwater resources and drinking water supplies.

1.2. Overview: Fate and Behavior of MNPs through Porous Media

In recent years, the widespread presence of plastic pollution has emerged as a pressing global concern, with MPls (particles smaller than 5 mm) and NPls (particles smaller than 1 µm) increasingly recognized as significant environmental contaminants (ISO/TR 21960, 2022). The extensive use and improper disposal of plastics have led to their ubiquitous distribution across terrestrial, aquatic, and atmospheric compartments, posing multifaceted challenges to ecosystems, human health, and environmental sustainability.

The deleterious effects of MNPls on nature, human health, and ecosystems have garnered increasing attention from researchers, policymakers, and environmental advocates alike (Prata et al., 2020). These minute plastic particles, manufactured, or derived from the fragmentation and degradation of larger plastic items (European Commission, 2023). Due to their small size, they can easily be transported and spread through different environmental matrices, such as soils, sediments, and aquatic systems. In these environments, they can induce adverse effects across multiple trophic levels (Amobonye et al., 2021).

The initial research primarily focused on the prevalence of MNPls pollutions within marine ecosystems (Andrady, 2011; Carpenter & Smith, 1972; Thompson, Olsen, et al., 2004). Rivers are often situated closer to plastic sources than marine waters, serving as significant pathways for the transport and release of plastic contaminants and lakes can act as long-term sink of plastic

contaminants (Alimi et al., 2018). Freshwater and terrestrial environments not only function as major sinks for MNPls but also can emerge as significant sources of groundwater MPls pollution. There is a noticeable lack of studies concerning the fate of plastic pollution within groundwater environments, despite the fact that groundwater stands as the largest reservoir of fresh water globally, accounting for a remarkable 97% of the Earth's available freshwater (Wei & Chen, 2023). The potential for MNPls to infiltrate groundwater can be influenced by processes such as groundwater recharge from surface water and interactions between surface water and groundwater (Koelmans et al., 2019). Soil-groundwater interactions are identified as the primary pathway for the migration of plastic particles into groundwater. Soils are estimated to contain a MNPls load ranging from 4 to 23 times greater than that of the oceans, serving as a major conduit for MPls to enter the food web directly (Allen et al., 2022).

Another avenue providing fresh water supply is industrial drinking water treatment plant (DWTPs), which use filtration of porous media as one of the processes. The water treatment methodology is tailored to the characteristics and requirements of each DWTP according to its design. Key processes aimed at removing dissolved and particulate contaminants include coagulation/flocculation, sand filtration, activated carbon filtration, and disinfection (Y. Li et al., 2022; Negrete Velasco et al., 2022; Y. Zhang et al., 2020). Research underscores the significant role of filtration stages, which act as an initial barrier complementing other treatment processes within the plant (G. Hul, Okutan, et al., 2024; Pulido-Reyes, Magherini, Bianco, Sethi, von Gunten, et al., 2022; Ramirez Arenas et al., 2022; Y. Zhang et al., 2020). Nonetheless, there remains a notable likelihood of tap water harboring particles smaller than 1 μm that evade retention by the DWTP (Y. Li et al., 2022). Mitigating the presence of such particles in drinking water sources, it is imperative to investigate the efficacy of various treatment processes, with particular attention to sand filtration, which effectively captures NPls (Pivokonsky et al., 2018). A deeper comprehension of the mechanisms underlying sand filtration is essential for managing and enhancing the transport and fate of NPls, recognized as environmental pollutants. Consequently, the filtration property of saturated porous media, examined within the scope of the thesis, serves as the foundation for exploring the behavior and fate of MNPls in saturated porous media, as discussed in this overview section.

The filtration mechanism of porous media comprises three distinct steps. Firstly, a transport step primarily governed by physical-hydraulic processes occurs. Afterward, a step for attachment begins, driven by a physical-chemical process. Lastly, the detachment step occurs, where retained particles are released as new particles or clean water is introduced. Together, these steps delineate the dynamic processes governing the complex filtration mechanism of porous media (Adin et al., 1979). The primary physical mechanisms driving particle transport within filter pores encompass Brownian diffusion, deposition, direct interception, and hydrodynamics. Brownian diffusion assumes a pivotal role, particularly for particles smaller than 1 micron (Banihashem & Karrabi, 2022). Deposition, governed by gravity, is associated with the sedimentation rate of particles, guiding them along streamlines toward the grains of porous media—termed collectors. This mechanism holds particular relevance for particles larger than 1 micron, where particle density becomes critical. Interception occurs as particles closely traverse streamlines near the collector,

leading to attachment. The hydrodynamic process, influenced by particle rotation and movement across streamlines, is intricately linked to particle shape and its interaction with the fluid (Banihashem & Karrabi, 2022; Compère et al., 2001; P. Sun et al., 2015).

The findings by O'Connor et al., (2019) indicate that MPls already present in sandy soils may have the potential to *infiltrate into the subsurface* to depths that, over the long term, could lead to exposure of MPls to subterranean fauna or receptors within the aquifer system. Additionally, the research has shown that among the five types of MPls examined, PE-fine MPls (D_{50} = 21 µm ± 25 µm) of smaller size demonstrated the greatest mobility. In comparing sandy soil and clay loam, the study found that while the penetration depth of NPls (0.45 µm) was consistent across both media, particles reached the same depth quicker in sandy soil than in clay loam (Ren, Gui, Wei, et al., 2021). The increase in size of plastic particles (from 0.8 to 2 µm) resulted the increase in retention the porous media. The aggregation of agglomeration also weakened the mobility of plastic particles. There is relation the effect of salinity on MPls transport strongly depended on MPls size (Z. Dong et al., 2018)

The *chemical properties of the water play* a crucial role in determining the retention of MPls and NPls within porous media. The surface charge relation between porous media and plastic particles effects. The retention and these electrical properties depend on chemical factors, such as solution pH, ionic strength, and colloid zeta potentials. A heightened negative charge fosters the expansion of the electrostatic double-layer between MNPls and sand, as well as between MNPls themselves. As the ionic strength increased, the zeta potential values of both negatively and positively charged NPls decreased. However, with an increase in ionic strength, the electrical double layer can be compressed, reducing the repulsive forces and resulting in a decreased net repulsive energy barrier between NPl particles, ultimately causing aggregation. Consequently, this phenomenon facilitates the transportation of plastic particles. The enhanced retention of both MNPls correlates with an increase in ionic strength (Chu et al., 2019; S. Dong et al., 2021; Z. Dong et al., 2018; J. Wu et al., 2019; X. Wu et al., 2020). The increase in pH levels facilitated the transport of NPls within porous media. This phenomenon is primarily attributed to surface potentials, resulting in a more negatively charged surface of NPls as pH increases (Ling et al., 2021).

The *surface functionalities* of plastics significantly influence their transport behavior. Changes in physicochemical properties, particularly in the surface chemistry of MNPls, such as an increase in oxygen-containing functional groups and a reduction in surface charge, have been observed. These alterations ultimately lead to the enhanced transport of aged MPls within the soil environment (Ren, Gui, Wei, et al., 2021). The surface functionalities effects the electrostatic attraction between colloids and sand (Z. Dong et al., 2019). The impact of the surface charge of NPls on the adsorption capacity of porous media was examined using NPls with opposite charges. The lower adsorption capacity observed for lower concentrations of NPls suspension can be attributed to weak interactions between negatively charged NPls aggregates and the negatively charged sand surface. Conversely, the higher adsorption capacity observed for higher concentrations is attributed to strong electrostatic interactions between positively charged NPls aggregates and negatively charged sand grains (G. Hul, Martignier, et al., 2024).

Elevated *concentrations* of MPls correlate with increased particle transport. Moreover, the influence of concentration diminishes with decreasing flow rates (Chu et al., 2019; Hou et al., 2020). The effect of flow rate on the transport capacity of pollutants varied depending on the porous medium. Each medium possesses unique surface properties and pore structures, resulting in differing impacts of flow rate (Ahfir et al., 2007; Chu et al., 2019; P. Zhang et al., 2016). This phenomenon is likely attributable to the rapid decrease in retention sites as the input concentration of MPls increases.

The presence of *engineered nanoparticles, bacteria, clay, and organic matter (OM),* in the environment directly influences the transport and deposition of MNPls. The presence of OM in the environment decreases the transport ability of MPls due to OM enhancing repulsive forces within the double layer between plastic particles and porous media (Hou et al., 2020). The presence of variable charge sites, primarily concentrated at the edges of clay minerals and influenced by the pH of the background solution, presents advantageous locations for the deposition of NPls (Lu et al., 2021). Also, the presence of clay coatings on surfaces of porous media has a notable impact on the charge heterogeneity and surface roughness. Clays can introduce charge heterogeneity due to their positively or less negatively charged surfaces, thereby enhancing the retention of negative charged plastic particles (Liang et al., 2022). In low ionic strength conditions, the presence of clay increases the mobility of MPls. Nevertheless, at high ionic strength, both clay and OM collectively affect MPls transport, with OM enhancing the transport of MPls (Li et al., 2021). MNPls have the capability to adsorb contaminants, potentially enhance the spread of contaminants and posing a risk of pollution to freshwater sources such as groundwater and DWTPs (Atugoda et al., 2021; Gouin et al., 2011; Guo et al., 2020; McCormick et al., 2016). Under high ionic strength conditions, the presence of MNPls resulted in an increase in bacteria transport and a decrease in bacteria deposition in quartz sand (He et al., 2018). The existence of surfactants in the aquatic environment suppresses aggregation and alters the mobility of MNPls by modifying their charge (Y. Jiang et al., 2022; Peng & Wang, 2022). At levels of ionic strength below a specified threshold, NPls facilitate the transportation of co-existing heavy metal ions, while exhibiting an inhibitory effect at higher ionic strength levels. At lower ionic strength levels, heavy metal ions may vie with ions on the NPs for the same adsorption sites, thereby encouraging the remobilization of heavy metal ions through ion exchange mechanisms. However, increased ionic strength can diminish the repulsive forces between NPls and porous media, leading to an augmentation in NPls diameter. Consequently, this may result in the obstruction and deposition of NPls within quartz sand, impeding the outflow of heavy metal ions (Ling et al., 2021).

The adaptation of approaches utilized for solute transport to *colloidal solution transport* is a common practice (Chu et al., 2019; Simunek et al., 2006). Various models in the literature integrate the classical advection-dispersion equation with different types of kinetic attachment models. The common approach assumes either one-site kinetics, involving both forward and reverse terms (Tufenkji & Elimelech, 2004) or two-site kinetics, which account for reversible and irreversible attachment mechanisms (Chu et al., 2019; Compère et al., 2001). In a kinetic model, the solute transport equation delineates the rate at which the solute is adsorbed onto the solid surface and subsequently desorbed from it (Fetter et al., 2018). MPls with size 1 μm were well simulated by

the convection-diffusion equation including two types of first-order kinetic deposition which are the rate of first-order deposition (attachment) and entrainment (detachment) (Chu et al., 2019). Recent studies have predominantly focused on analyzing the transport of MPls into porous media using particles ranging around 1 μm in size (Z. Dong et al., 2018; M. Li, Zhang, Rong, et al., 2021; Zhao et al., 2021). Hou et al., (2020) investigated MPls with sizes ranging from 40 μm to 48 μm, revealing that larger particle sizes, combined with lower ionic strength and the presence of fulvic acid, could potentially enhance the movement of MPls within porous media. Conversely, smaller-sized porous media and lower velocities were found to exhibit superior filtration performance. The maximum mass recovery of MPls was determined to be 18%. The attachment-detachment model, featuring a time-dependent detachment coefficient, offers enhanced predictive accuracy for the transport of MPls (10 μm and 20 μm) within porous media compared to conventional attachment models. This highlights the critical role of MPls desorption. Nevertheless, the detachment of large MPls from soil appears to occur in a relatively unpredictable manner, posing difficulties for both the Attachment Model and the Attachment-Detachment Model to capture effectively. The calculated total mass recovery under various conditions ranged from 0.08% to 35.9% (Qi et al., 2022).

Research on the *impact of MNPls on freshwater organisms* has garnered significant attention. Various studies have demonstrated that differing concentrations of MNPls within terrestrial aquatic ecosystems can have diverse effects on the growth, behavior, reproduction, and mortality of aquatic organisms (Meng et al., 2023). Moreover, research has indicated that the ecological impacts of plastics on organisms are heavily influenced by particle size, with smaller particles posing greater risks (Wright et al., 2013). These particles can also bioaccumulate and transfer along the food chain, ultimately reaching higher-level organisms, including humans. Human exposure to MNPls primarily occurs through oral intake, emphasizing the importance of investigating freshwater sources as potential reservoirs of these particles (B. Jiang et al., 2020).

1.3. List of Publications

Publications included in this thesis:

Articles :

Okutan, H.; Sağır, Ç., Kurtuluş, B., Özmen, H. B., Pekkan, E., Razack, M., Le Coustumer, P. (2024). Understanding Microplastics Retention Efficiency and Sorption Dynamics in Porous Media. Preprints 2024, 2024021670. https://doi.org/10.20944/preprints202402.1670.v1 (Submitted to Nanomaterials MDPI)

Okutan, H., Hul, G., Stoll, S., & Le Coustumer, P. (2023). Retention and Transport of Nanoplastics with Different Surface Functionalities in a Sand Filtration System. Nanomaterials, 14(1), 32. https://doi.org/10.3390/nano14010032

Okutan, H. M., Sağir, Ç., Fontaine, C., Nauleau, B., Kurtulus, B., Le Coustumer, P., & Razack, M. (2022). One-Dimensional Experimental Investigation of Polyethylene Microplastic Transport in a Homogeneous Saturated Medium. Frontiers in Environmental Science, 10. https://doi.org/10.3389/fenvs.2022.885875

Book chapters:

Okutan, H. M., Le Coustumer, P., Kurtuluş, B., & Razack, M. (2023). Transport Process of Microplastics from Terrestrial to Aquatic Environment: Evaluation of the Current Knowledge. In Recent Research on Environmental Earth Sciences, Geomorphology, Soil Science, Paleoclimate, and Karst (pp. 55–57). https://doi.org/10.1007/978-3-031-42917-0_13

Abstracts and Conference Presentations:

Le Coustumer P., **Okutan H.,** Kurtulus B., & Razack M., Continental Water Resources Concerned by Micro and Nanoplastics? , 2nd International Conference, Water Resources Management & Sustainability: Solutions for Arid Regions, 26-28 February 2024, Dubai

Okutan H., Sağır Ç., Pekkan E., Kurtulus B., Razack M., & Le Coustumer P. First results on the transport of polydisperse polyethylene microplastics in saturated porous media, 50th International Association of Hydrogeologists Congress, 17-22 September 2023, Cape Town, South Africa

Extended Abstracts:

Okutan H., Le Coustumer P., Kurtulus B., Razack M., Pekkan E., Sağır Ç., Initial Findings: Influence of Flow Velocities on Microplastics Retention in Saturated Porous Media, 4th International Conference Waters in Sensitive And Protected Areas, 10-13 April 2024, Pula, Croatia (Accepted to be presented and published).

Okutan H.M., Le Coustumer P., Kurtulus B., & Razack M. Transport Process of Microplastics from Terrestrial to Aquatic Environment: Evaluation of the current knowledge, Mediterranean Geosciences Union (MedGU), 25-28 November 2021, Istanbul, Türkiye

Publications not included in this thesis:

Hul, G., **Okutan, H.,** Le Coustumer, P., Ramseier Gentile, S., Zimmermann, S., Ramaciotti, P., Perdaems, P., & Stoll, S. (2024). Influence of Concentration, Surface Charge, and Natural Water Components on the Transport and Adsorption of Polystyrene Nanoplastics in Sand Columns. Nanomaterials, 14(6), 529. https://doi.org/10.3390/nano14060529.

Yeşilmaden, H. M., İnan, Ç. A., Kurtuluş, B., Canoğlu, M. C., Avşar, Ö., & Razack, M. (2021). Land subsidence assessment under excessive groundwater pumping using ESA Sentinel-1 satellite data: a case study of Konya Basin, Turkey. Environmental Earth Sciences, 80(11), 409. https://doi.org/10.1007/s12665-021-09718-z.

CHAPTER 2 - MATERIALS AND METHODS

2.1. Materials

2.1.1. Polyethylene Microplastics

Various polyethylene (PE) types with distinct surface characteristics and sizes of microplastics (MPls) were employed in the study. Notably, these materials lack precise calibration and standardization. The PE-1 particles in powder form, falling within the size range of 200–500 µm, were isolated using sieves. The PE-2 variant, sourced from Goonvean Fibres, United Kingdom, was purchased in a powdered state, with the company specifying its density as 0.91 g cm^{-3}. It is noteworthy that the general density range for PE is recognized to span from 0.88 to 0.96 g cm^{-3} (Hüffer et al., 2019; O'Connor et al., 2019). To ensure consistency, the chemical definition of both PE-1 and PE-2 was verified through Fourier-transform infrared (FTIR) measurements (Figure 2.1.). The characteristics of PE absorbance bands are 720 cm^{-1}, 1460 cm^{-1}, 2850 cm^{-1}, and 2920 cm^{-1} (da Silva & Wiebeck, 2022; Zięba-Palus, 2017).

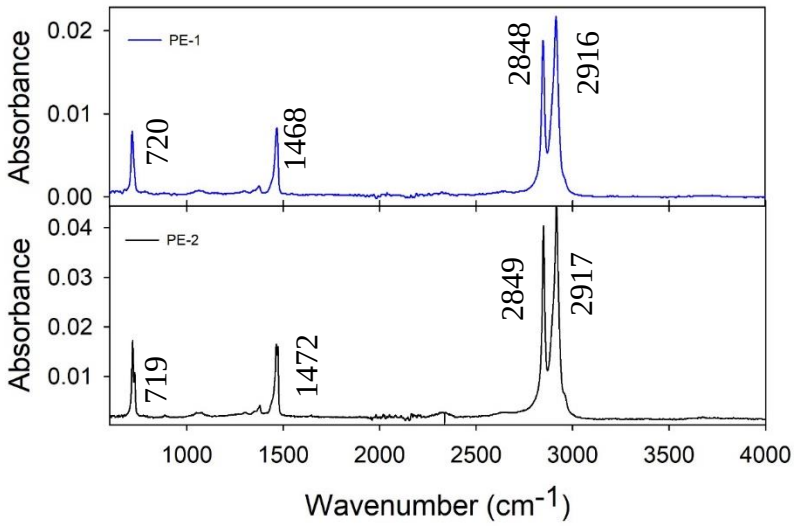


Figure 2.1. PE-1 (blue line) and PE-2 (black line) spectra acquired by FTIR.

The grain sizes of this PE-1 and PE-2 were measured by Zeiss Primostar optical microscopy and ZEN 2.6 Primostar software. The grain size statistics and the histogram of the PE particles are given in Table 2.1. and Figure 2.2., respectively. The average size is defined as 308 ± 91 µm for

PE-1 and 16 ± 6 µm for PE-2 (Table 2.1). Their shape is not well rounded and smooth shown in Figure 2.3.

Table 2.1. General descriptive statistics of PE-1 and PE-2 MPls. Units are in µm

	Size of Population	Max	Min	Median	Mean	Standard Deviation	25 %	75 %
PE-1	200	601	163	294	308	91	233	357
PE-2	400	77	2	16	16	6	13	19

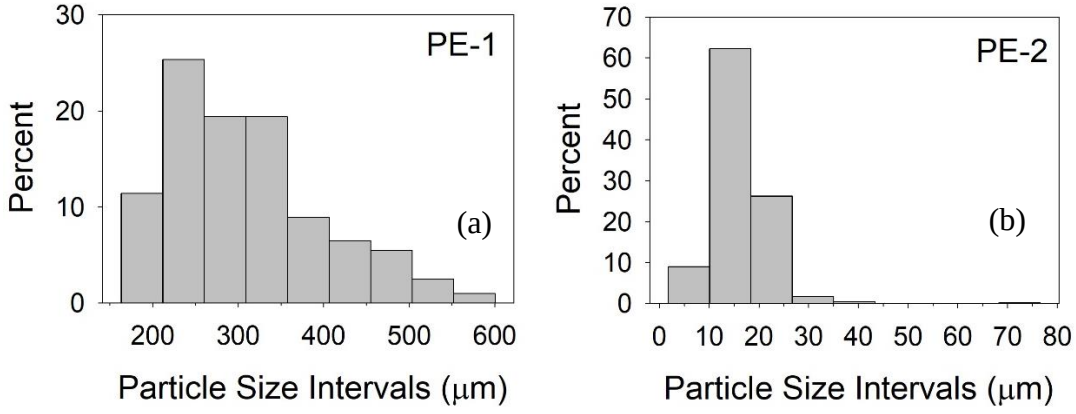


Figure 2.2. The size distrubiton histogram of PE-1 (a) and PE-2 (b) MPls.

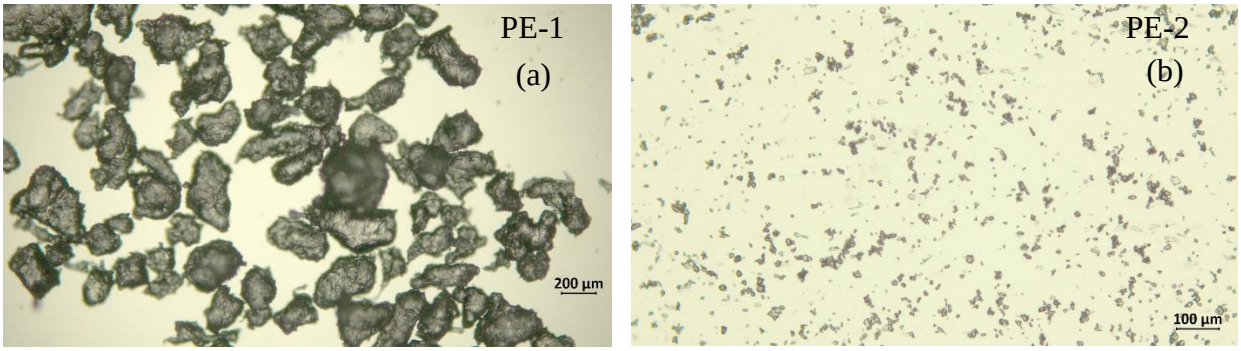


Figure 2.3. Optical microscopy image of PE-1 (a) and PE-2 (b).

2.1.2. Polystyrene Nanoplastics

Surfactant-free polystyrene latex nanoplastics (NPls) featuring positive amidine functional groups (-NH-NH2+) on their surfaces were generously provided by the Institute of Analytical Sciences (ISA), affiliated with the National Centre for Scientific Research (Paris, France), and the University Claude Bernard (Lyon, France). The suspension comprised 50 g/L of styrene transformed into polystyrene, achieving a conversion rate of 86%. The size of the amidine-functionalized

polystyrene latex NPls with a positive charge ([A-PS]+) was determined through dynamic light scattering (DLS) and transmission electron microscopy (TEM), yielding measurements of 177 ± 4 nm and 147 ± 17 nm, respectively.

Sulfate latex NPls without surfactants, featuring negative sulfate functional groups ($-SO^{2-}_4$) on their surfaces, were procured from Invitrogen (ThermoFisher Scientific, Switzerland). As per the manufacturer's specifications, these particles are identified by a primary diameter of 0.1 µm. The size measurements of the sulfate polystyrene latex nanoplastics with negative charge ([S-PS]-), as determined through dynamic light scattering (DLS) and transmission electron microscopy (TEM), were in line with the specifications provided by the supplier, measuring 114 ± 1 nm and 109 ± 10 nm, respectively. Both original solutions were stored in a dark environment at a temperature of 4°C and were utilized for the preparation of solutions with lower concentrations. All dilutions were made using ultrapure water (Milli Q water, Millipore, Switzerland, with a resistivity of > 18 MΩ·cm and total organic carbon (TOC) < 2 ppb).

Table 2.2 and Figure 2.4 present the size measurements of NPls obtained through TEM, along with their corresponding histogram. The micrograms related to these measurements are illustrated in Figure 2.4. Additionally, the size measurements based on DLS are detailed in Table 2.3.

Table 2.2. General descriptive statistics of size measurements of NPls with TEM. Units are in nm.

Type of NPls	Size of population	Mean	Standard Deviation	Max	Min	Median	25 %	75 %
[A-PS]+	917	147	17	168	55	152	144	157
[S-PS]-	964	109	9	244	83	109	104	114
[A-SDS-PS]-	229	168	17	204	105	170	161	179

The charges of each particle have been determined in the zeta potential measurement results obtained in aqueous solutions. Accordingly, the charges of [A-PS]+, [S-PS]-, and [SDS-A-PS]- nanoplastics are 43 ± 2 mV, -43 ± 3 mV, and -44 ± 1 mV, respectively (Table 2.3).

Table 2.3. Z-average hydrodynamic diameter (nm) and zeta potential (mV) measurements of NPls (pH = 3 ± 0.1).

[A-PS]+		[S-PS]-		[SDS-A-PS]-	
nm	mV	nm	mV	nm	mV
177 ± 4	43 ± 2	114 ± 1	-34 ± 1	172 ± 1	-44 ± 1

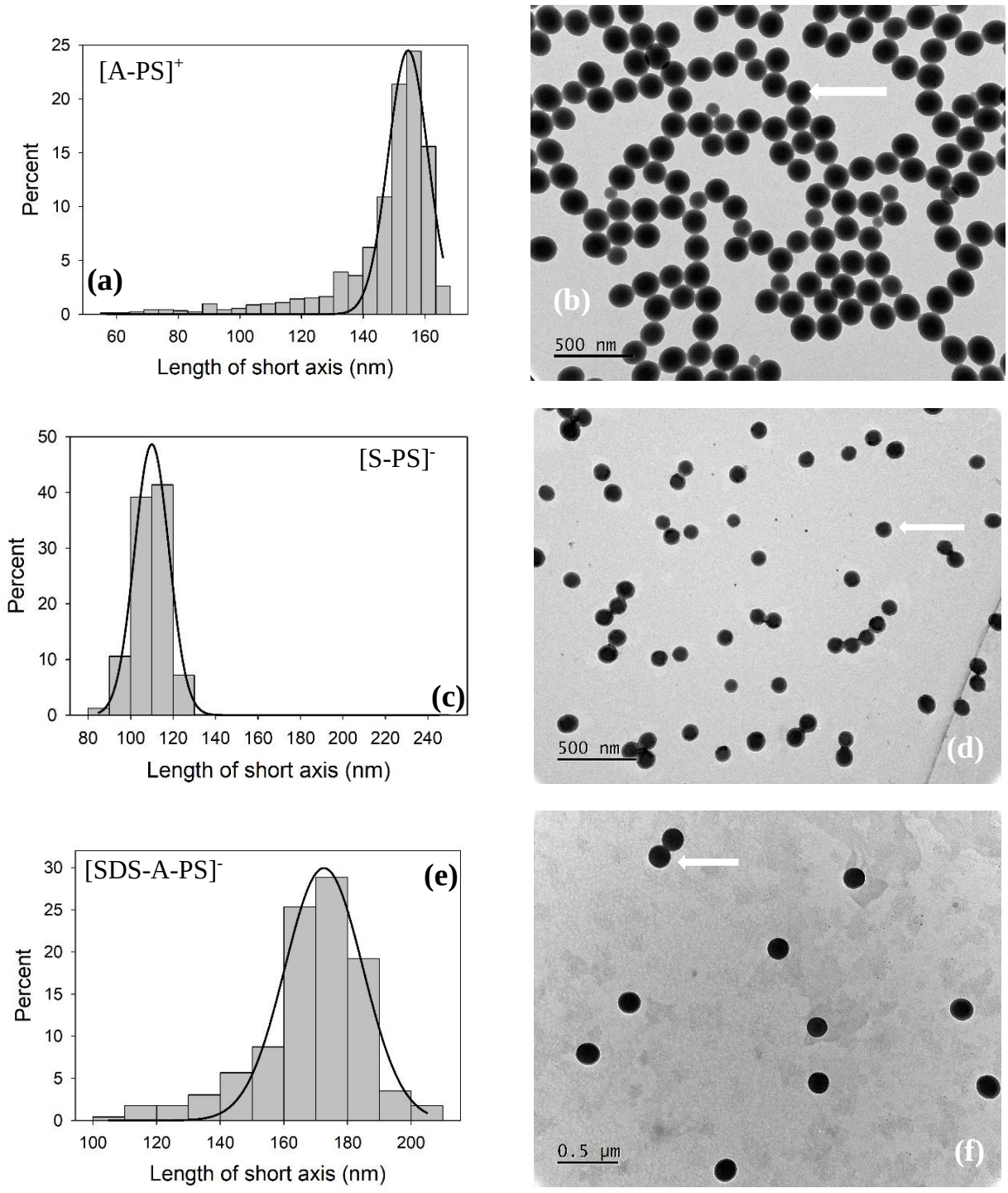


Figure 2.4. (a, b) [A-PS] + (a, b), [S-PS]- (c, d) and [SDS-A-PS]- (e, f) NPls (white arrows) size distribution and histogram which was measured from TEM micrography (pH = 3 ± 0.1)

A pH-titration curve was constructed for [A-PS]+ NPls and [S-PS]- NPls to elucidate their characteristics under varying pH conditions (Figure 2.5). Suspensions of each NPl type, with a concentration of 50 mg/L, underwent titration using diluted 1 M HCl and 1 M NaOH solutions (Titrisol, Merck, Switzerland) within a pH range of 3.0 ± 0.1 to 11.0 ± 0.1. pH adjustments were

carefully monitored using a Hach Lange HQ40d portable meter (Hach Lange, Switzerland). Measurements of the z-average hydrodynamic diameter and zeta potential (ζ) were conducted approximately 15 minutes after pH stabilization using ZetaSizer Nano ZS (Malvern Instruments, Worcestershire, United Kingdom). [A-PS]+ NPls exhibit a positive charge until reaching the point of zero charge, which is observed at a pH value of 10.7 ± 0.1. In contrast, [S-PS]- NPls remain stable and maintain a negative charge across the entire pH range.

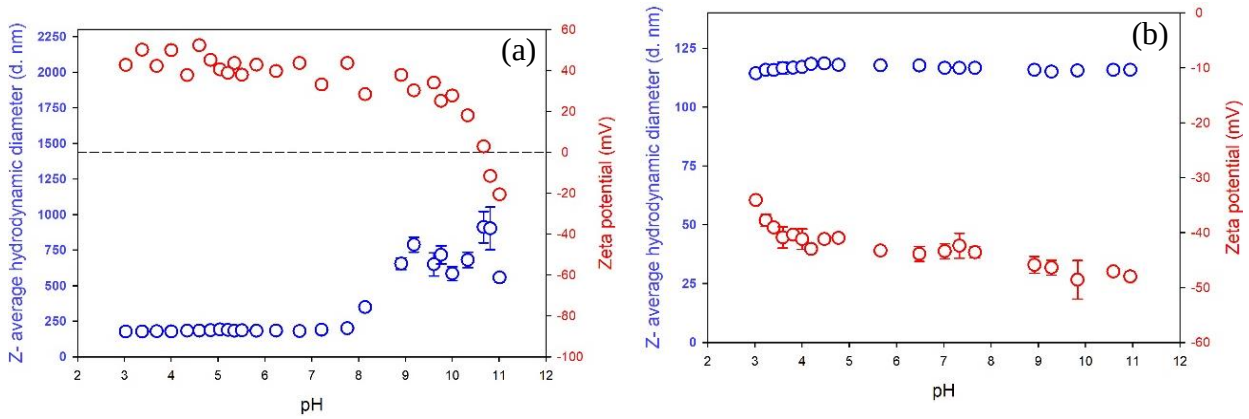


Figure 2.5. Size and ζ potential titration curves for (a) [A-PS]+ and (b) [S-PS]-.

Sodium dodecyl sulfate (SDS; AppliChem, purity >99%, Darmstadt, Germany) solutions were formulated by dissolving the surfactant in ultrapure water and were utilized without additional purification for the preparation of SDS-coated polystyrene amidine latex nanoplastics ([SDS-A-PS]-). The latter was created by combining a polystyrene amidine latex NPls solution of a specified concentration with an SDS solution of a designated concentration. The necessary quantity of SDS for coating was determined through batch experiments. A designated concentration of SDS was created and homogenized using an orbital shaker (IKA KS 260, Germany) for a minimum of 15 minutes. Subsequently, the hydrodynamic diameter and the zeta (ζ) potential of the NPls were measured. Critical SDS concentrations were determined through experimental means to ensure the complete coating of NPls surfaces and to prevent the presence of free surfactants in the solution. A plateau in ζ potential values for 100 mg/L, 500 mg/L, and 1000 mg/L [A-PS]+ NPls was observed at SDS concentrations of 300 mg/L, 400 mg/L, and 500 mg/L, respectively (Figure 2.6). These concentrations were then employed for the preparation of SDS-coated PS amidine latex ([SDS-A-PS]$^{-}$) NPls.

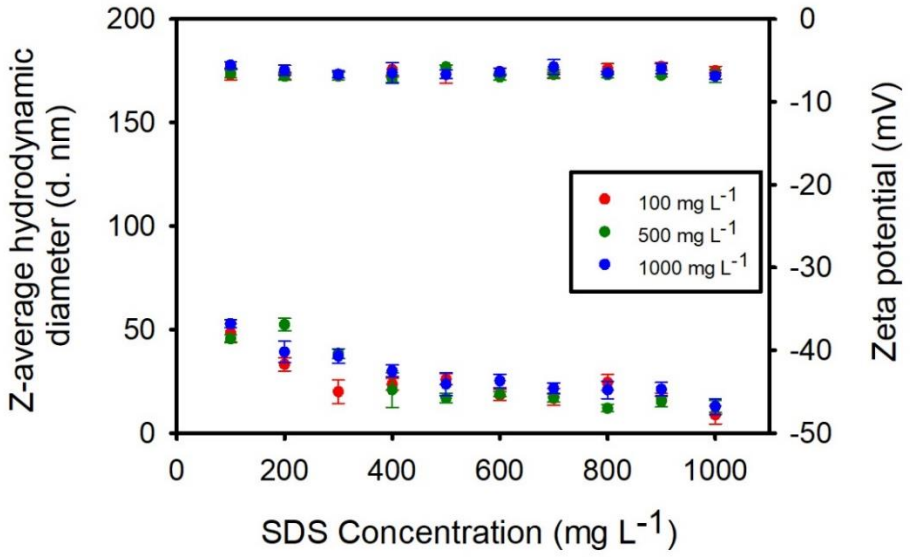


Figure 2.6. The critical concentrations of SD) exhibited variations across different concentrations of [A-PS]+ NPls (Conditions: ultrapure water.).

2.1.3. Porous Media

In the experiments involving PE-1, four distinct porous media types with varying grain sizes were utilized, namely large silica balls, small silica balls, sand, and coarse gravel. The grain and pore sizes of large silica balls, small silica balls, and sand were determined using optical microscopy (Table 2.4. and Table 2.5.). These materials were combined with resin in a plastic holder and allowed to dry. Subsequently, the dried samples were horizontally cut near the bottom, and the bottom sides were examined with an optical microscope to measure pore and grain sizes. The particle size of the coarse gravel was directly measured using a tape measure. For pore size measurements of the coarse gravel, pore sizes were directly assessed on the column filled with the material. A total of 40-90 measurements were conducted for each material to ensure a reliable pore/grain size distribution for each utilized material.

Table 2.4. General descriptive statistics of the grain size of the porous medium materials.

	Maximum	75 %	Mean	Median	25 %	Minimum	St. Deviation
Large Silica (µm)	3075	2038	1950	1865	1716	1205	404
Small Silica (µm)	1366	1109	1051	1055	989	705	127
Sand (µm)	1372	710	627	613	505	212	204
Coarse Gravel (mm)	47	31	27	27	23	16	7

Table 2.5. General descriptive statistics of the pores size of the porous medium materials.

	Maximum	75 %	Mean	Median	25 %	Minimum	St. Deviation
Large Silica (µm)	2634	1658	1144	1079	510	298	677
Small Silica (µm)	1295	791	655	612	408	282	289
Sand (µm)	763	450	405	398	318	214	117
Coarse Gravel (mm)	20	7	6	5	3	1	4

The resolution of optical microscopy images varies depending on the magnification. The smallest measurable pixel sizes for the images of large silica, small silica, and sand were 213 µm, 206 µm, and 211 µm, respectively. For large silica, 58% of the pores exceeded 800 µm, and 97% were larger than 400 µm. In the case of small silica, 93% of the pores were greater than 300 µm. As for sand, 79% of the pores measured above 300 µm. The pore sizes of coarse gravel ranged from 1 mm to 20 mm.

Based on the grain size distributions of the porous medium, the most prevalent grain size intervals for the large silica, small silica, sand, and coarse gravel are 1700-2000 µm, 1000-1100 µm, 400-800 µm, and 23-28 mm, respectively. Pore and particle size distribution of porous medium were shown in Figure 2.7.

The effective porosity (n_e) of the porous media was determined through fluorescent tracer experiments, resulting in values of 42% for large silica, 41% for small silica, 31% for sand, and 40% for coarse gravel.

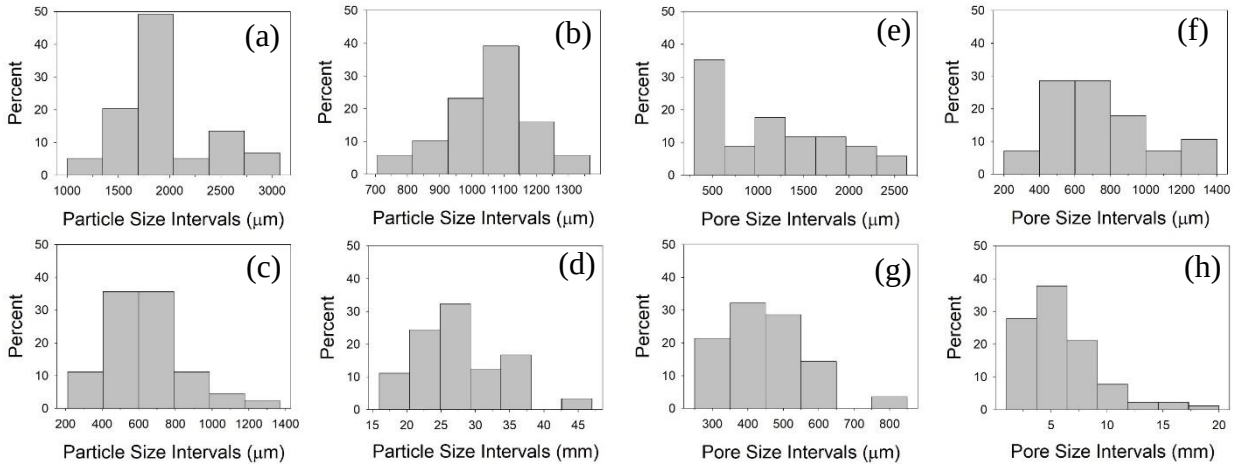


Figure 2.7. The particle size distribution histogram for the large silica balls (a), small silica balls (b), sand (c) and coarse gravel (d) and the pore size distribution histogram for the large silica balls (e), small silica balls (f), sand (g) and coarse gravel (h).

In the experiments involving PE-2, the porous media which is quartz sand was kindly provided by Esan Eczacıbaşı Industrial Raw Materials Co. (Türkiye) with a density of 2.60 g/cm^3. Particle size determination was conducted through sieve analysis, yielding a D_{50} value of 2.9 mm. A significant

portion, specifically 84% of the sand, exhibited retention on a 2 mm mesh-sized sieve (Table 2.6). The hydraulic conductivity of the sand was determined using a constant head permeameter and was found to be 11.0 ± 0.3 cm/min. The effective porosity (n_e) was calculated as 0.49 through fluorescent tracer experiments and numerical modeling.

Table 2.6. The sieve analysis measurements for quartz sand.

Mesh Size (mm)	Mass Retained (%)	Cumulative Mass Passed (%)
6.3	0.00	100
5.6	0.00	100
4	5	95
2	84	11
1	9	2
0.6	0.7	1
0.25	0.9	0.5
0.125	0.4	0.1
0.075	0.06	0.00

For the NPls experiments, the porous media was supplied by Carlo Bernasconi AG (Zürich, Switzerland) and primarily consists of silica, accounting for 97–99%. Additionally, trace amounts of other constituents are present, including Al_2O_3, K_2O, Na_2, TiO_2, Fe_2O, TiO, CaO, MgO, Fe_2O_3, and Na_2O. The size and morphology characteristics of sand grains, as determined using Camsizer (Retsch, Germany), were generously provided by the Industrial Services of Geneva. Sand grains are classified into 11 granulometric classes, primarily falling within size ranges of 2.38 to 2.83 mm, 2.83 to 3.36 mm, and 3.36 to 4.00 mm. They exhibit an ellipsoidal shape, characterized by an average width-to-length ratio of 0.655. The surfaces of these grains are notably heterogeneous, featuring an average roughness of 0.826 and an average convexity close to 1 (Table 2.6). As reported by Hul et al. (2022), sand grains exhibit a negative charge across a wide pH range, specifically ranging from pH 1.0 ± 0.1 to pH 12.0 ± 0.1. The effective porosity (n_e) of the sand was determined to be 0.41 ± 0.1 through fluorescent tracer experiments.

Table 2.7. The properties of size and shape of quartz sand grains.

Grain size (mm)	Volume proportion of particles in the range (%)	Cumulative distribution (%)	Sphericity	Aspect ratio	Convexity
0 - 0.75	0.05	0.05	0.785	0.660	0.979
0.75 – 1	0.00	0.05	0.806	0.581	0.992
1 – 1.2	0.01	0.06	0.567	0.328	0.979
1.2 – 1.5	0.07	0.13	0.577	0.310	0.982
1.5 – 2	1.54	1.67	0.708	0.437	0.986
2 – 2.38	7.26	8.93	0.774	0.529	0.988
2.38 – 2.83	24.74	33.67	0.823	0.622	0.989
2.83 – 3.36	40.64	74.31	0.845	0.692	0.989
3.36 – 4	22.98	97.29	0.848	0.728	0.987
4 – 4.76	2.67	99.96	0.826	0.761	0.982
> 4.76	0.04	100	0.654	0.742	0.956

2.1.4. Fluorescent Dyes

Fluorescent dyes used for environmental water tracing should exhibit certain properties. They should be readily soluble in water, demonstrate stability over time without deterioration in the investigated medium (water, air, and aquifer material), be easily measurable even at large dilutions, simple to detect, low in toxicity with no significant health or environmental threats, and readily available and inexpensive (Field et al., 1995).

Tracer experiments utilized fluorescent dyes in columns oriented vertically, to investigate the hydrodynamic parameters of the porous medium materials employed in the studies. The fluorescent dyes included fluorescein sodium salt (Sigma Aldrich) in powder form and rhodamine WT (Cole-Parmer) at a concentration of 25 g/L.

Rhodamine WT is categorized as an orange fluorescent dye, while fluorescein is classified as a green fluorescent dye. Sodium fluorescein ($C_{20}H_{10}Na_2O_5$; Color Index: Acid Yellow 73) is known for its high solubility in water, visibly detectable in low concentrations, and poor stability under sunlight. In Europe, it is referred to as uranine. Low pH values are unsuitable for the usage of sodium fluorescein because the fluorescence of fluorescein diminishes noticeably at pH values below 5 (Field et al., 1995; Sabatini & Austin, 1991; Smart & Laidlaw, 1977). Rhodamine WT ($C_{29}H_{29}N_2O_5Na_2Cl$) is acknowledged as the most stable fluorescent dye to sunlight and chlorine, and its fluorescence intensity remains stable when the pH is above 6 (Sutton et al., 2001). Studies suggest that rhodamine WT may not be entirely conservative, as there is potential for its sorption onto suspended sediments, porous media, silica sand, and other solid surfaces (Runkel, 2015; Sabatini & Austin, 1991). According to both batch and column studies, the level of sorption of fluorescein was determined to be significantly lower than that of rhodamine WT. (Sabatini & Austin, 1991). During the modeling of fluorescent dyes to comprehend the hydrodynamic

properties of porous media, the selection of appropriate isotherms took into consideration the sorption tendencies.

2.1.5. Surfactants

Sodium dodecyl sulfate (SDS) (AppliChem) in powder form and dish detergent with anionic surfactant (Pril, Henkel) were used in the studies.

2.2. Methods

2.2.1. Column experiments

2.2.1.1. Experimental Procedure

Three distinct experimental setups were configured for PE-1 at the University of Poitiers, France PE-2 at Eskişehir Technical University, Türkiye, and NPls at the University of Geneva, Switzerland. While the fundamental principles remained consistent across the setups, variations were introduced based on the injection mode of the particles and the column size.

Initially, plexiglass columns were filled with water to one-third of their volume. The column was then gradually packed with porous media with a bottom-up water flow using a peristaltic pump. Simultaneously, any air bubbles were eliminated by gently tapping the column. The columns designated for PE-1 and PE-2 were packed with dry porous media. Specially for PE-2, the porous media was initially washed, and then dried at 105°C for a minimum of 8 hours in an oven. The columns designated for NPls were packed with wet porous media that was solely washed. All the columns were sealed with steel screens having a mesh size bigger than plastic tracers and caoutchouc stoppers.

In the experiments involving PE-1, challenges arose in preparing a well-dispersed suspension due to the lower density of PE compared to distilled water and the hydrophobic properties of PE. This caused both the inhomogeneity of the injection suspension and the inability to inject a homogeneous concentration. Additionally, problems arose during concentration measurements because of the non-uniformity of the effluent samples. Consequently, to achieve a homogeneous distribution of PE-1 MPls suspension, the density of the liquid used was reduced. A mixture of ethanol and distilled water, with a ratio of 56% ethanol and 44% distilled water, was employed both in the saturation phase of the experiment and the preparation of injection suspensions. The resulting density of this liquid mixture was approximately 0.87 g/cm³. Successful suspension of PE-1 particles within this liquid matrix was achieved. The construction of the column and circulation system took into account measures to minimize ethanol evaporation, so a closed system

was designed due to the usage of ethanol-distilled water mixture for circulation liquid. The length (X) and the inner diameter (R_2) of the column were 100 cm and 8 cm, respectively (Figure 2.8). The column was packed with porous media and the ethanol–distilled water mixture (Reservoir 1) was circulated for a duration to saturate the porous medium. Once steady-state flow conditions were attained, the valve of Reservoir 1 was closed, and concurrently, the valve of Reservoir 2 was opened to initiate the finite-duration MPl injection. The implanted experimental conditions are presented in Table 2.8. An apart system was used for fluorescent dye experiments.

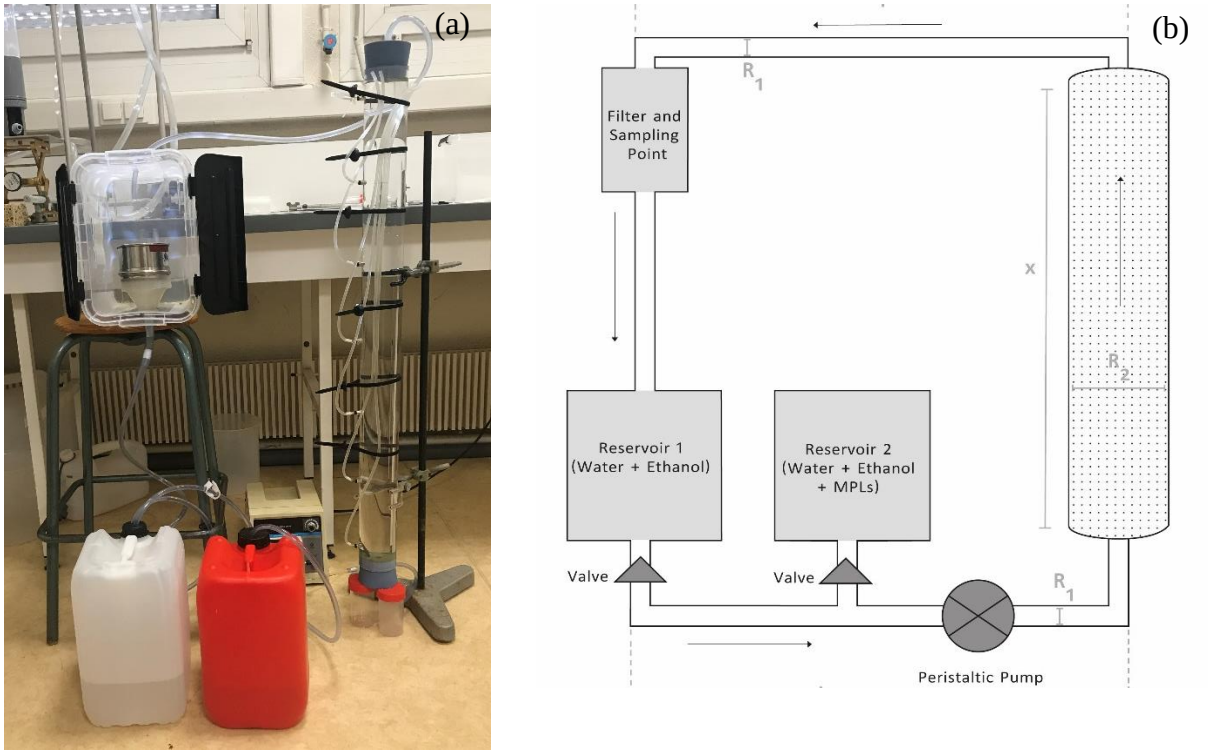


Figure 2.8. The experimental setup for the PE-1 MPls tests (a) is the actual setup and (b) is the schematic illustration of setup. X signifies the length of the porous medium, R_1 (0.3 cm) denotes the radius of the joint pipes, and R_2 (8 cm) represents the radius of the column (Location: University of Poitiers, France).

Table 2.8. Parameters of the tests with PE-1.

	Large Silica			Coarse Gravel		
Exp. No	Q (cm^3/min)	V_{inj} (cm^3)	C_{inj} (g/L)	Q (cm^3/min)	V_{inj} (cm^3)	C_{inj} (g/L)
P1	70	1120	24	41	2029	20
P2	105	524	10	154	2308	20
P3	206	2063	10	-	-	-

The fluorescent tracer experiments were performed by vertically placed columns with 80 cm length and 5.7 cm radius. Under a steady flow rate within the saturated medium, the hydrodynamic parameters of the porous medium materials used in this study were investigated with instantaneous injection of fluorescein (Table 2.9.).

Table 2.9. The flow rates (Q) and injected tracer volumes (Vinj) for the fluorescent tracer tests.

	Large Silica		Small Silica		Sand		Coarse Gravel	
Exp. No	Q (cm^3/min)	V_{inj} (mL)	Q (cm^3/min)	V_{inj} (mL)	Q (cm^3/min)	V_{inj} (mL)	Q (cm^3/min)	V_{inj} (mL)
1	29	0.19	42	0.21	51	0.17	32	0.19
2	49	0.27	22	0.10	40	0.26	60	0.39
3	21	0.30	54	0.27	29	0.15	103	0.29
4	44	0.15	29	0.14	21	0.12	-	-

Experiments with PE-2 operated with distilled water. Subsequently, the column underwent thorough flushing with distilled water, reaching a state of saturation and flushed until the effluent exhibited negligible turbidity measurements. The operational pH and electrical conductivity values were measured following each MPls transport experiment, with mean values determined as 7 ± 0.2 for pH and 57 ± 5 µS cm-1 for electrical conductivity, respectively. The Plexiglas column is 100 cm in height and 7 cm inner diameter (Figure 2.9). The fluorescent tracer experiments were conducted in the same column with instantaneous injection in contrast the injection of PE-2 was continuous.

A commercial dish detergent incorporating anionic surfactants was utilized to establish homogeneous dispersions. The preparation of injection concentrations involved MPls and surfactant at a ratio of 1:1, with a concentration of 2 g/L. Initial attempts with lower ratios were unsuccessful until reaching the 1:1 ratio, which led to successful dispersion. The injection volume targeted 1.8 times the pore volume, with one pore volume of the sand-packed column being 1678 ml. An equivalent of 1.8 pore volumes of the fluorescent dye tracer was continuously injected, subsequently followed by the utilization of at least 2 pore volumes for the fast flow rate and 5 pore volumes for the slow flow rate of distilled water to flush the column. Subsequently, this injection procedure was repeated for the continuous injection of MPls. The flow was carried out at a constant flow rate generated by a peristaltic pump. For each flow rate, samples of 4 ml were collected every two minutes at a flow rate of 65 ml/min and every three minutes at a flow rate of 31 ml/min. Replication of each flow rate condition was maintained for constant head permeameter, fluorescent dye, and MPls injected experiments.

Table 2.10. The flow rates (Q) and injected tracer volumes (Vinj) for the PE-2 and fluorescent tracer tests.

	Fluorescent Tracer			PE-2 Tracer		
Exp. No	Q (cm^3/min)	V_{inj} (cm^3)	C_{inj} (g/L)	Q (cm^3/min)	V_{inj} (cm^3)	C_{inj} (g/L)
A	31	3078	0.0004	31	3125	2
A.1	30	3094	0.0004	31	3078	2
B	65	3113	0.0004	65	3125	2
B.1	64	3148	0.0004	64	3137	2

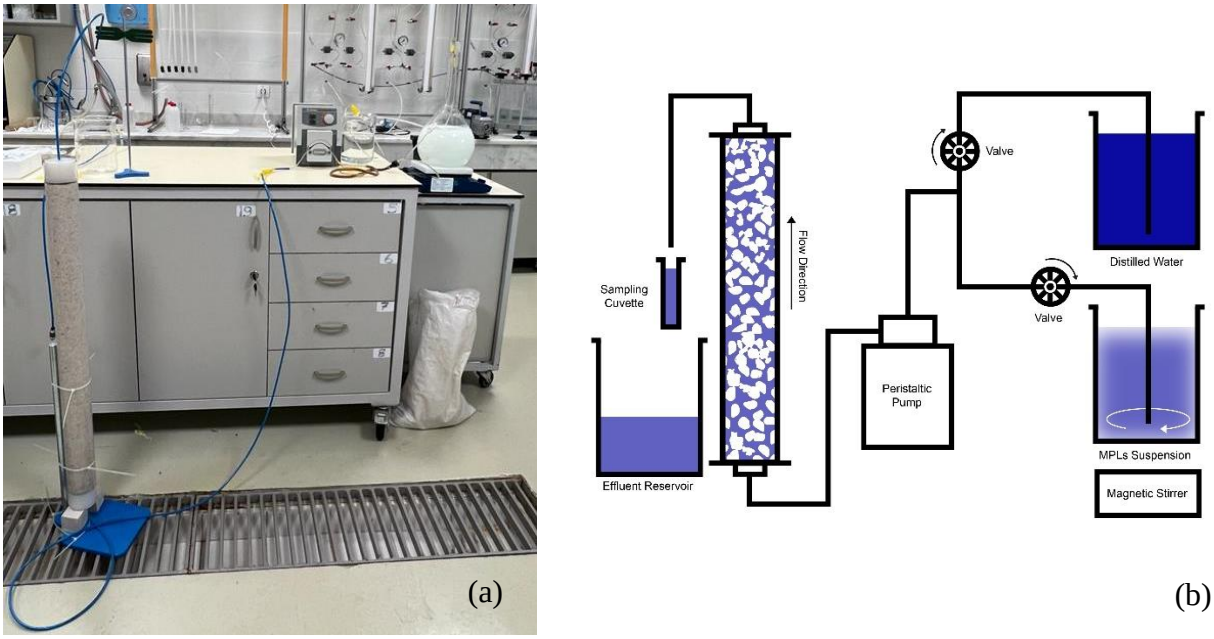


Figure 2.9. The experimental setup for the PE-2 MPls tests (a) is the actual setup and (b) is the schematic illustration of the setup (Location: Eskişehir Technical University, Türkiye).

The experimental setup utilized for NPls studies is illustrated in Figure 2.10. It consisted of an ultrapure water reservoir, silicon tubing, and an acrylic column with a 36 mm inner diameter and 200 mm length. The column was sealed with steel screens featuring a mesh size of 250 µm and caoutchouc stoppers. An upward flow of ultrapure water was initiated within the column using a peristaltic pump (Minipuls 3, Gilson, Switzerland) with the flow rate adjusted to 20 ± 1 ml min^{-1} for each experiment. Before each experiment, the column was equilibrated to a steady-state condition by pumping ultrapure water for at least 2 hours. During the experiment, 0.3 mL of NPls suspension was injected into the column, followed by the background solution. Manual sample collection was performed at intervals of every 60 seconds and 30 seconds after the injection of NPls. In specific columns, a 0.3 ml solution of SDS (Sodium Dodecyl Sulfate) was injected post the filtration stage to investigate the impact of surfactants on the remobilization of retained NPls.

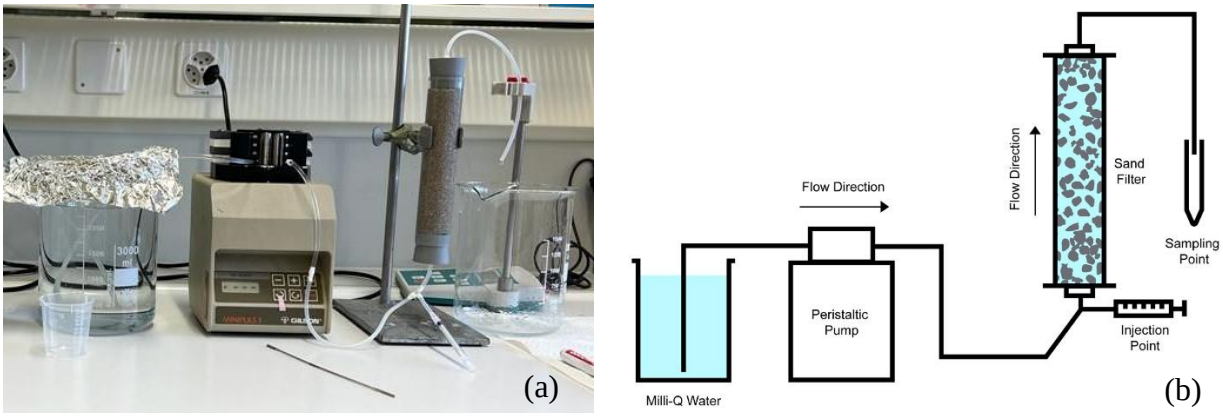


Figure 2.10. The experimental setup for the NPls tests (a) is the actual setup and (b) is the schematic illustration of setup (Location: University of Geneva, Switzerland)

2.2.1.2. One dimensional analytical and numerical modeling

Quantitative fate and transport play a crucial role in risk assessments by providing insights into the behavior of contaminant-dissolved substances within soil environments. Ongoing research is now exploring the applicability of effectively characterizing the movement and fate of particulate substances in these contexts.

Dissolved solids or suspended particles undergo advective transport, or advection, as they travel with the flowing groundwater. In conditions of pure advection both the groundwater and the dissolved solute move at the same average velocity. This synchronous movement characterizes the advective transport process, wherein the bulk flow of groundwater moves substances, contributing to the overall transport dynamics in subsurface environments.

The amount of substance being transported is influenced by both its concentration in the groundwater and the volume of flowing water. In scenarios of one-dimensional flow perpendicular to a unit cross-sectional area of porous media, the volume of water in motion per unit section equals the product of the average linear velocity (u) and the effective porosity (n_e).

The average linear velocity (u) denotes the rate at which water flux occurs across the unit cross-sectional area of pore space. It is essential to note that this is distinct from the average rate at which water molecules traverse individual flow paths, as the latter tends to be greater due to tortuosity.

The effective porosity (n_e) represents the porosity through which flow is possible. Non-interconnected and dead-end pores are excluded from the effective porosity calculation. This exclusion ensures a more accurate representation of the porous media's capability to facilitate fluid flow.

The mean transit time was determined by employing Equation (2.1) and Equation (2.2) to determine the initiation time and intervals for measuring the effluent (Fetter, 2014).

$$T = \frac{X}{u} \tag{2.1}$$

$$u = \frac{Q}{A * n_e} \tag{2.2}$$

Where T is the mean transit time (T), X is the distance from injection point (L), u is the mean velocity (L/T), Q is flowrate (L^3/T), A is the cross-sectional area of the column (L^3) and n_e is effective porosity (dimensionless, ratio).

In a scenario where all groundwater carrying the substances moves at precisely the same speed, it would displace water devoid of the substances, leading to a sudden interface between the two water types. However, due to variations in the velocity of the infiltrating solute or particle containing water, mixing transpires along the flow path. This phenomenon is termed mechanical dispersion and culminates in the dilution of the substances at the progressing front of the flow. The mixing that occurs along the direction of the flow path is denoted as longitudinal dispersion. This dispersion process plays a critical role in the overall transport and distribution of contaminants within the groundwater system.

Molecular diffusion and mechanical dispersion are so closely connected in the context of flowing groundwater that they cannot be considered independently. Instead, they are combined to create a single parameter known as the hydrodynamic dispersion coefficient (D). This coefficient essentially quantifies the collective impact of both molecular diffusion and mechanical dispersion, providing a comprehensive measure of how solutes spread and disperse in the dynamic flow of groundwater.

The foundational assumptions guiding this derivation of the Advection-Dispersion Equation (ADE) are that the porous medium under consideration is homogeneous, isotropic, and fully saturated with fluid. The derivation assumes that flow conditions adhere to the validity of Darcy's law (Fetter, 2014).

The analytical solution was employed for the interpretation of PE-1 experiments, encompassing both MPls and fluorescent tracer experiments, as well as for determining sand characteristics in experiments utilizing a fluorescent tracer. Additionally, the porosity of the sand used in NPls experiments was determined using the analytical solution. On the other hand, numerical solutions were applied for the interpretation of PE-2 experiments, covering both MPls and fluorescent tracer experiments. Transport of the fluorescent tracer was simulated using the ADE incorporating first-order reversible kinetic (non-equilibrium) sorption terms, whereas the transport of MPls was modeled with ADE incorporating first-order reversible kinetic (non-equilibrium) sorption and first-order irreversible rate reaction terms.

The longitudinal dispersivity and kinematic porosity of the porous medium were computed using the inverse solution method based on the results of the fluorescent tracer experiments. The one-dimensional ADE with and without sorption terms was employed to generate modeled breakthrough curves (BTCs). Subsequently, these calculated curves were fitted to the BTCs obtained from the fluorescent measurements of the outlet samples. The fitting process was carried out using the Solver Add-in of the Excel application for analytical solutions and Groundwater Vistas Version 7 (student license) for numerical solutions, allowing for the iterative adjustment of selected parameters to achieve the best fit. The dispersivity (α) and kinematic porosity (n_k) were determined by calculating the averages of the results from multiple experiments for each material and condition. Under steady-state flow and saturated conditions in a homogeneous porous medium, the transport of suspended particles can be described by the ADE (Bear & Cheng, 2010).

$$\frac{\partial C}{\partial t} = D\frac{\partial^2 C}{\partial x^2} - u\frac{\partial C}{\partial x} \tag{2.3}$$

Where $\partial C/\partial t$ is solute concentration change over time, C is solute concentration (M/L^3), D is longitudinal dispersion coefficient (L^2/T), x is distance between the sampling point and the injection point (L), and u is average linear water velocity (L/T).

The ADE was employed for instantaneous injection, assuming a one-dimensional, semi-infinite, isotropic, and homogeneous porous medium to generate analytical breakthrough curves (BTCs) (Kreft & Zuber, 1978).

$$C_i(x,t) = \frac{M_0\, x}{An_k u\sqrt{4\pi D t^3}} \exp\left(-\frac{(x-ut)^2}{4Dt}\right) \tag{2.4}$$

Where C_i is the concentration at the sampling point (M/L^3), M_0 is recovered mass (M) and n_k is kinematic porosity (dimensionless, ratio).

The same principles utilized in the solution method for the fluorescent tracer experiment were also applied to tests involving PE-1 (Equation (2.1), (2.2), and (2.3)) (Bear, 1988; Bear & Cheng, 2010). The one-dimensional ADE for finite-duration injection, as proposed by Ogata and Banks (1961) and based on the assumptions of 1D, semi-infinite, isotropic, and homogeneous porous medium, was employed (Equation (2.5)). A comparable procedure to the fluorescent tracer test solution for inverse modeling, using the Solver Add-in in Excel, was applied for the PE-1 tracer experiments, incorporating additional modifiable parameters such as concentration injected and injection time.

$$C_i\,(x,t) = \frac{C_0}{2}\left[erfc\left(\frac{X-ut}{2\sqrt{Dt}}\right) + \exp\left(\frac{uX}{D}\right) erfc\left(\frac{X+ut}{2\sqrt{Dt}}\right)\right] \tag{2.5}$$

where C_0 is the initial injection concentration (M/L^3).

In numerical computations, MT3DMS and MODFLOW were employed, which are commonly used in simulations for the transport of contamination into subsurface groundwater environments (Shu et al., 2023). MT3DMS is a model designed for three-dimensional multi-species solute transport. It addresses the resolution of advection, dispersion, and chemical reactions of contaminants within saturated groundwater flow systems. MT3DMS is commonly utilized in tandem with MODFLOW, a block-centered finite-difference flow model. Once a flow model is created and calibrated, the necessary information required by the transport model can be supplied, and this data can subsequently be accessed by the transport model (Zheng et al., 2013).

The transport of florescent tracer was simulated using ADE incorporating first-order reversible kinetic (non-equilibrium) sorption, while the transport of PE-2 MPls was modeled with ADE incorporating first-order reversible kinetic (non-equilibrium) sorption and first-order irreversible rate reaction terms. The numerical models were created from the observed values using Groundwater Vistas Version 7 (student license), which provides user interfaces for the MODFLOW and MT3D modules of the USGS (Zheng & Wang, 1999). The MT3D module is applied to model convection, dispersion, and chemical reactions within groundwater systems.

The partial differential equation describing the fate and transport of contaminants in one-dimensional, transient groundwater flow systems can be expressed as follows (Zheng & Wang, 1999):

$$\frac{\partial(nC)}{\partial t} = \frac{\partial}{\partial x}\left(n_k D \frac{\partial C}{\partial x}\right) - \frac{\partial}{\partial x}(n_k u C) + qC_s + \Sigma R_n \tag{2.6}$$

where C is the concentration (ML^{-3}), q is the volumetric flow rate per unit volume of aquifer representing fluid sources (positive) and sinks (negative) (T^{-1}), C_s is the concentration of the source or sink flux (ML^{-3}), and ΣRn is chemical reaction term ($ML^{-3}T^{-1}$).

In situations where the assumption of local equilibrium is deemed impractical, it is proposed that the sorption process can be accurately described through a first-order reversible kinetic reaction, as follows:

$$\partial \frac{\partial C'}{\partial t} = \beta(C - \frac{C'}{K_d}) \tag{2.7}$$

where C' is the sorbed concentration (ML^{-3}), β is the first-order mass transfer rate between the dissolved and sorbed phases (T^{-1}), and K_d is the distribution coefficient (L^3M^{-1}).

In certain scenarios, when the solute is adsorbed onto the solid phase, desorption becomes impossible. This reaction is irreversible, resulting in a mass loss of the dissolved phase. This

phenomenon can be elucidated using the first-order irreversible kinetic sorption model, described by the following equation:

$$\frac{\partial C'}{\partial t} = K_1 C \tag{2.8}$$

where K_1 (T^{-1}) is the first-order irreversible sorption rate constant.

Lee et al., (2021) utilized the first-order irreversible kinetic sorption model to analyze the movement of a toluene contaminant plume under 3D flow conditions. This kinetic model has also been employed in previous studies, such as Matthies et al., (2008), to simulate processes like radioactive decay or biodegradation. In these cases, the constant rate (K_1) is correlated with the half-life ($t_{1/2}$) of the materials in the following manner:

$$K_1 = \frac{ln2}{t_{1/2}} \tag{2.9}$$

Rhodamine WT, when applied to the quartz sand utilized in this study, may not exhibit entirely conservative behavior, as highlighted in previous research (Runkel, 2015; Sabatini & Austin, 1991). Consequently, a numerical solution incorporating sorption processes was deemed more appropriate, resulting in improved alignment between calculated BTCs and observed BTCs. Through fluorescent dye experiments, key parameters characterizing porous media properties, including kinematic porosity (n_k), dispersivity (α), distribution coefficient for the sorbed phase (K_d), and the first-order mass transfer rate (β), were estimated. The derived n_e and α values were subsequently employed as inputs for analyzing MPl transport experiments. In these MPl experiments, the parameters under investigation encompassed the distribution coefficient (K_d), first-order mass transfer rate (β), and another parameter denoted as K_1. The determination of optimal values necessitated the application of a trial-and-error approach. Iterative adjustments of the parameters K_d, β, and K_1 were performed to optimize the alignment between the calculated and observed curves. Following each adjustment, the residual sum of squares (RSS) error was scrutinized to assess model performance.

The model's sensitivity was evaluated through systematic adjustments of individual parameters, such as Q, K_d, β, and K_1, to assess their impacts on MPl filtration. Each parameter was varied independently based on the predicted outcomes of MPl A and MPl B experiments. The influence of sorption on MPl transport was analyzed using both MPl particle transport experiments and dye (solute) experiments, with the latter serving as a reference for BTCs. Furthermore, the examination of retention efficiencies aimed to understand the effects of Q and K_1 parameters on retention.

Monitoring the plastic content in the effluent reveals a breakthrough curve, where the effluent concentration, C(t), is plotted against Pore Volume (Q/V_0). V_0 represents the volume of porous media occupied by a fluid. If the incoming fluid suddenly contains a substance with a concentration

labeled as C_0, then at any given time, the proportion of this substance in the outflow is indicated by the ratio C/C_0. This breakthrough curve offers insights into the distribution of residence times within the column. For ease of comparison across different scenarios, breakthrough curves are commonly depicted using dimensionless variables. The resulting plot, C(t)/C0 vs. Pore Volume, constitutes the dimensionless breakthrough curve.

2.2.2. Constant Head Permeameter Experiment

The hydraulic conductivity (K) of the employed porous media for the PE-2 MPls was determined using a constant-head permeameter. This type of permeameter is specifically designed for non-cohesive sediments. The experimental setup consists of two main components: a column containing the saturated porous medium, and a mechanism to maintain a constant water level on the porous medium. The plexiglass column, with dimensions of 100 cm in length and 7 cm in diameter, remains consistent for all experiments. The constant head ensures a continuous water flow through the column, and measurements are taken from the bottom of the column. Prior to each tracer experiment, constant head permeameter experiments are conducted, and the mean values of three measurements are utilized for subsequent analyses.

The hydraulic conductivity of the packed sand was determined with Dacy's Law (Batu, 2005):

$$K = -\frac{Q}{A(dh/ds)} \tag{2.10}$$

K is the hydraulic conductivity (L/T), Q is discharge (L^3/T), A is the cross-sectional area of the column (L^2), and dh/ds is the hydraulic gradient.

2.2.3. Retention Efficiency

To ascertain the transported quantity, the methodology involves calculating the area under the curve. In contrast to the other experiments, the PE-2 experiments involved measuring the final experimental effluent concentration to gather data on the transported mass. The numerical modeling results were also employed to calculate the amount of transported mass. Subsequently, the retention efficiency was determined by comparing the transported mass quantities obtained through different methods. Subsequently, this initially transported quantity is subtracted from the total injected amount. This analysis provides valuable insights into the retention efficiencies of both nano and microplastics within porous media, elucidating the extent to which these particles are retained or transported through the system (Equation (2.11)).

$$m_R = Q \int_0^{\infty} C(t)\partial t \tag{2.11}$$

where m_R is recovered mass [M], Q [L^3 T^{-1}] is flow rate, C(t) is the tracer concentration by the time [ML^{-3}]. The retention efficiency was obtained with the following equation:

$$R = \frac{(m_i - m_R)}{mi} x100 \tag{2.12}$$

where R represents retention efficiency and m_i represents the total injected mass [M] of MNPls.

2.2.4. Z-Average Hydrodynamic Diameter Measurements

Dynamic Light Scattering (DLS), a widely adopted technology for sizing nanoparticles, relies on the temporal variations in scattered light resulting from the Brownian motion of suspended particles to determine their hydrodynamic size distribution (Xu, 2008).

Brownian motion is the motion exhibited by particles as a consequence of random collisions with the molecules present in the surrounding liquid. A crucial aspect of Brownian motion, particularly in the context of DLS, is that smaller particles demonstrate rapid movement, while larger particles exhibit slower motion. The relationship between the size of a particle and its velocity arising from Brownian motion is encapsulated in the Stokes-Einstein equation (Einstein, 1905).

The velocity of Brownian motion is delineated by the translational diffusion coefficient, denoted as D. The hydrodynamic radius (R_H) is determined by calculating the particle translation diffusion coefficient D, using the Stokes-Einstein equation, which assumes the particle's spherical shape. In this equation, k_B denotes the Boltzmann constant, T represents the absolute temperature, and η_0 denotes the solvent viscosity (Equation (2.13)).

$$R_H = \frac{K_b T}{6\pi\eta_0 D} \tag{2.13}$$

In this study, the measurement of the hydrodynamic radius was conducted employing a Zetasizer Nano ZS (Malvern Instruments Ltd; Malvern, UK). All measurements were performed after a 1-minute equilibration period at a temperature of 25 °C. The refractive index and absorbance parameters for both types of PS NPls were set at fixed values of 1.59 and 0.01, respectively. The calculations of ζ potential were based on five measurements, and each measurement encompassed ten individual runs.

2.2.5 Zeta Potential Measurements

The zeta potential constitutes an electrokinetic potential arising from electrokinetic phenomena, particularly evident upon interaction with a polar medium such as water, as examined in this study. When materials come into contact with such a medium, they inherently acquire a surface electrical charge spontaneously. Within a solution containing particles, an electrical double-layer (EDL) structure forms around each particle. Subsequent relative motion between the rigid and mobile components of the EDL leads to the generation of an electrokinetic potential. The zeta potential specifically refers to the electrical potential within the interfacial double layer (DL) at the slipping plane.

Utilizing zeta potential allows for the prediction of colloidal particle stability in the context of electrokinetic phenomena, particularly in electrophoresis. In instances where all particles within a suspension exhibit a markedly negative or positive zeta potential, mutual repulsion occurs, mitigating any inclination towards flocculation. Conversely, when particles possess low zeta potential values, the absence of repulsive forces facilitates their aggregation and subsequent flocculation. An often acknowledged benchmark for the zeta potential in stable aqueous suspensions is approximately 30 mV (Dukhin & Xu, 2020).

The electrophoretic mobility is directly measured, and the conversion to zeta potential is inferred based on theoretical considerations. The zeta potential through a process involving the determination of Electrophoretic Mobility followed by the application of the Henry equation (Equation (2.14) (Henry, 1931).

$$U_E = \frac{2\varepsilon\zeta f(\kappa a)}{3\eta} \tag{2.14}$$

Here, where ζ represents the measured electrophoretic mobility (μm·s^{-1}/V·cm^{-1}), ε the dielectric constant, η the zeta potential (mV), μ the medium viscosity (cm^2/s), and f(κa) the Henry's function. Henry's function is a constant unique to a specific system, exhibiting variability from 1 (referred to as the Hückel approximation) in non-polar systems to 3/2 (referred to as the Smoluchowski approximation) in ionic media, such as water (Lowry et al., 2016). The Smoluchowski approximation, specifically designed for aqueous media with a moderate electrolyte concentration, was utilized to transform electrophoretic mobility into ζ-potential.

The ζ-potential of NPls was assessed by the Zetasizer Nano ZS (Malvern Instruments Ltd; Malvern, UK). All measurements were conducted following a 1-minute equilibration period at a temperature of 25 °C. The refractive index and absorbance parameters for both types of PS NPls were standardized at 1.59 and 0.01, respectively. ζ potential calculations were derived from five measurements, with each measurement comprising ten individual runs.

2.2.6. Electron Microscopy

Electron microscopy stands out as a formidable visualization technique for characterizing nanoplastics in terms of their sizes, shapes, and morphologies. This method employs a beam of electrons to illuminate a sample positioned within a high vacuum environment, producing highly magnified images. Two primary categories of electron microscopes exist, distinguished by their imaging principles and specimen forms: transmission electron microscopy (TEM) and scanning electron microscopy (SEM).

Transmission electron microscopy is employed for observing thin specimens through which electrons can pass, resulting in the generation of a projection image. Conversely, in a scanning electron microscope, the electron beam is focused into a spot and subsequently scanned across the surface of the specimen. The interaction between the beam and the sample produces two main signals—secondary and backscattered electrons—which are collected using detectors and can be simultaneously displayed on a monitor.

Images of different types of nanoplastics were acquired using a JSM-7001FA SEM (JEOL Ltd., Tokyo, Japan) situated in the University of Geneva, Switzerland, JSM-IT500 J SEM (JEOL Ltd., Tokyo, Japan) located at the University of Poitiers, France and a Hitachi H7650 TEM (Hitachi High-Tech Corp., Tokyo, Japan) located at the Bordeaux Imaging Center, France.

The Hitachi instrument specifically applied for High-Contrast Transmission Electron Micrography (HC-TEM) under high vacuum conditions, utilized magnifications ranging from 40 k to 100 k and an accelerating voltage of 80 kilo-electron volts (keV). For characterization and fractal dimension analyses of selected effluent samples, a carbon and holey carbon support with copper grids was employed to deposit 10 µL (one drop) of NPls dispersions. Subsequently, the grids were dried under a glass cover with an infrared lamp before being introduced to the TEM.

The JSM-7001FA instrument was employed to examine sand grains and illustrate the relationship between NPls and quartz sand grains. In this process, a thin layer of a specialized adhesive was initially applied to a 5 × 5 mm silicon wafer (G3390, Agar Scientific), affixed to an aluminum stub with a diameter of 12.7 mm. Subsequently, a small number of sand grains obtained from the filtration column were carefully placed and embedded in the adhesive up to half of their height. The prepared samples were air-dried for a minimum of 48 hours and, before analysis, coated with a 10 nm layer of gold.

The morphological characterization of PE-1 was conducted using the JSM-IT500 J SEM (JEOL Ltd., Tokyo, Japan). The PE-1 in powder form was fixed to a glass slide and subsequently coated with a 1 nm thick carbon layer.

2.2.7. Fractal Dimensions

The concept of fractal geometry, pioneered by B. Mandelbrot, was developed to understand the structural features and properties of various objects, including colloidal aggregates (Mandelbrot, 1982). In this study, TEM images of aggregates obtained from the peak point effluents under selected NPLs experimental conditions were processed using the FRACLAC plugin in Image J FIJI software (Ferreira & Rasband, 2012). The box-counting method was employed, which involves estimating the area-filling properties of the boundary at different scales by counting the number of boxes, F, required to cover the object in a grid of a specified size, ε (Landini, 2011). Here, ε represents the scale, defined as the ratio of the box size to the image size, and F is the number of pixels counted per box (Karperien, 2004). This process was repeated for multiple grids with increasing spacing. The log-log plot of ε (x-axis) versus F (y-axis) produced a slope representing the fractal dimension, denoted as Df. The obtained Df value signifies the fractal dimension of the object. To validate the methodology, the Df of the Sierpinski Carpet was computed, resulting in a projected Df value of 1.88, closely aligning with its theoretical value of 1.89 (Torre et al., 2020).

2.2.8. Spectroscopic Measurements

Spectrophotometry involves quantifying the interaction between light and materials, encompassing phenomena such as reflection, transmission, scattering, or absorption of light. The selections for spectrophotometric measurements encompass spectral reflectance, transmittance, absorptance, emittance, scattering, and fluorescence. These measurements fall within the category of phenomenological optical properties characterizing the material.

Turbidimetry is a technique that quantifies the cloudiness or turbidity of a solution. In this investigation, turbidity measurements were conducted to monitor variations in the collected effluents throughout the experiments on the transport of micro and nanoplastics. Instruments calibrated in NTU (Nephelometric Turbidity Units) were aligned with standard calibration fluids, adhering to the prescribed methods outlined in the user manuals.

For tracing the PE-2 MPls, The Aquaflour® Handheld dual-channel fluorometer and turbidity device were used. Cuvettes of dimensions 10mm x 10mm, made of plastic, were employed in the study. The turbidity channel utilized a green LED with an excitation wavelength of 515 ± 10 nm and corresponding emissions. The device was initially calibrated using a 1000 NTU calibration standard then several concentrations were prepared and measured in NTU. The conversion NTU to g/L was performed with calibration curves (Figure 2.11). The calibration curve was prepared before each MPls injection.

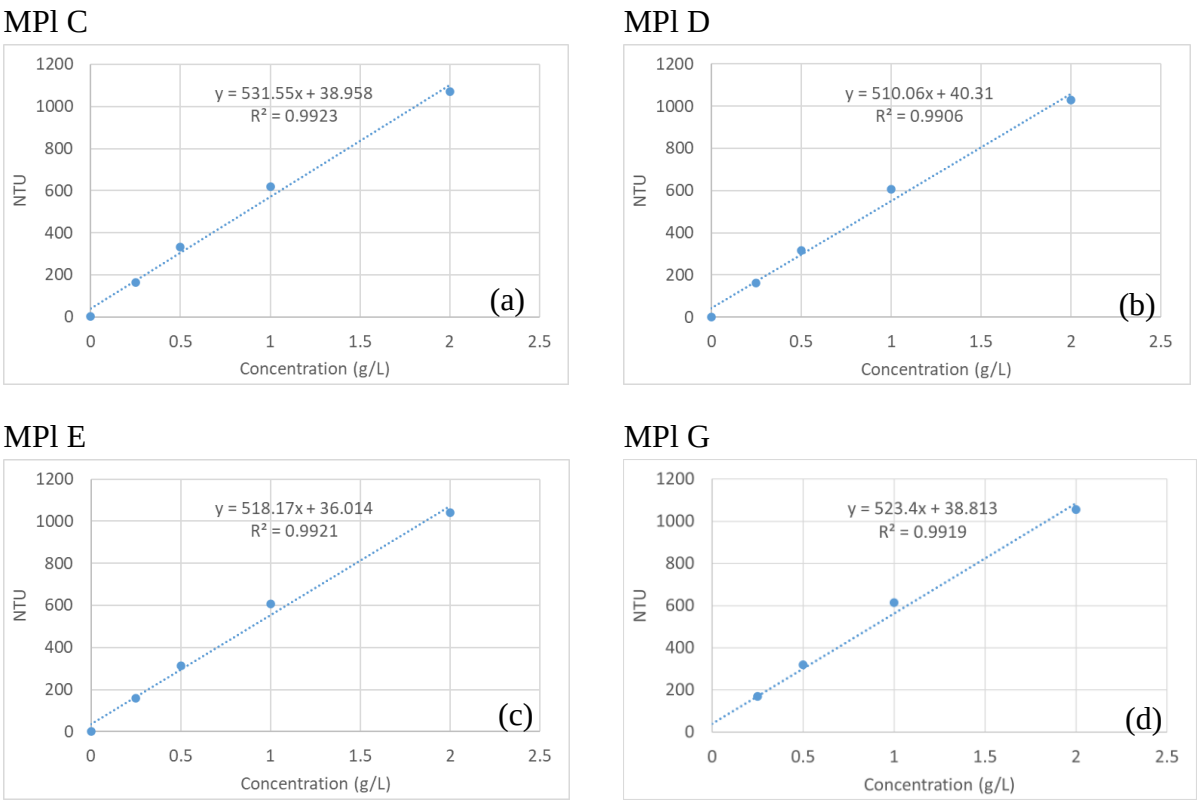


Figure 2.11. The calibration curves for PE-2 MPl experiments were used as plotting curves. NTU is the unit of turbidity. (a) corresponds to MPl C, (b) corresponds to MPl D, (c) corresponds to MPl E, and (d) corresponds to MPl G experiments.

The Turbidimeter Hach Lange TU5200, equipped with an infrared emitting laser at 850 nm, was employed to ascertain NPls concentration. Glass vials were utilized for the measurements. The instrument detects light scattered by particles at a 90° angle from the incident beam, with multiple detectors situated around the sample cell at 360°. Calibration curves were generated for each type of NPls and employed to convert the turbidity measurements in Nephelometric Turbidity Units (NTU) to concentration values in mg/L (Figure 2.12).

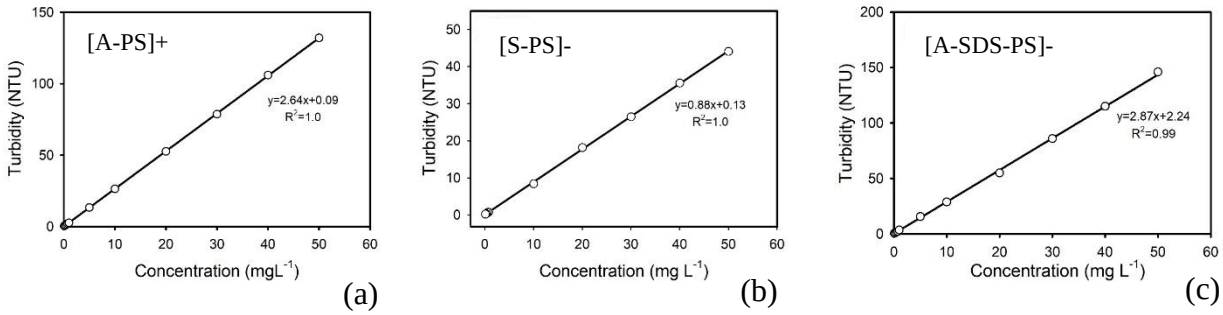


Figure 2.12 The calibration curves are employed to convert NTU measurements to concentration, and these curves are specialized for different types of NPls. Specifically, (a) is used for [A-PS]+, (b) is used for [S-PS]-, and (c) is used for [A-SDS-PS]- NPls experiments.

A fluorometer serves as a specialized instrument for the measurement of fluorescence or emitted light emanating from diverse fluorescing entities. The phenomenon of fluorescence arises when incident light of a precise wavelength interacts with and energizes electrons within a sample, prompting the immediate emission or fluorescence of light at a different wavelength. It is noteworthy that each fluorescent substance manifests a unique spectral fingerprint, signifying its characteristic pattern of excitation and emission wavelengths.

The TD-700 Laboratory Fluorometer, manufactured by Turner Design, equipped with a blue channel and utilizing glass vials, was employed for quantifying the PE-1 concentrations in the samples. The selection of a fluorometer was informed by the observed reflectance characteristics of PE-1 particles in the blue channel. Various PE-1 suspensions with known concentrations were meticulously prepared and subjected to measurement using the fluorometer. The resulting data, presenting PE-1 concentrations, were graphically represented against device measurements to construct a calibration curve. Subsequently, the established equations derived from the curve were applied to convert device measurements to corresponding PE-1 concentrations (Figure 2.13).

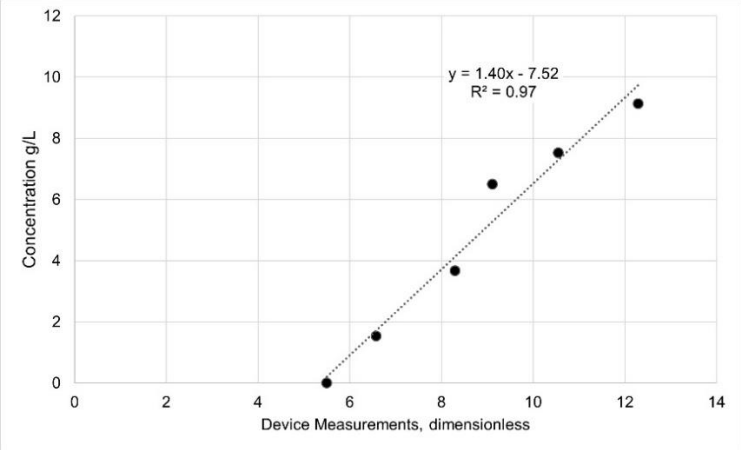


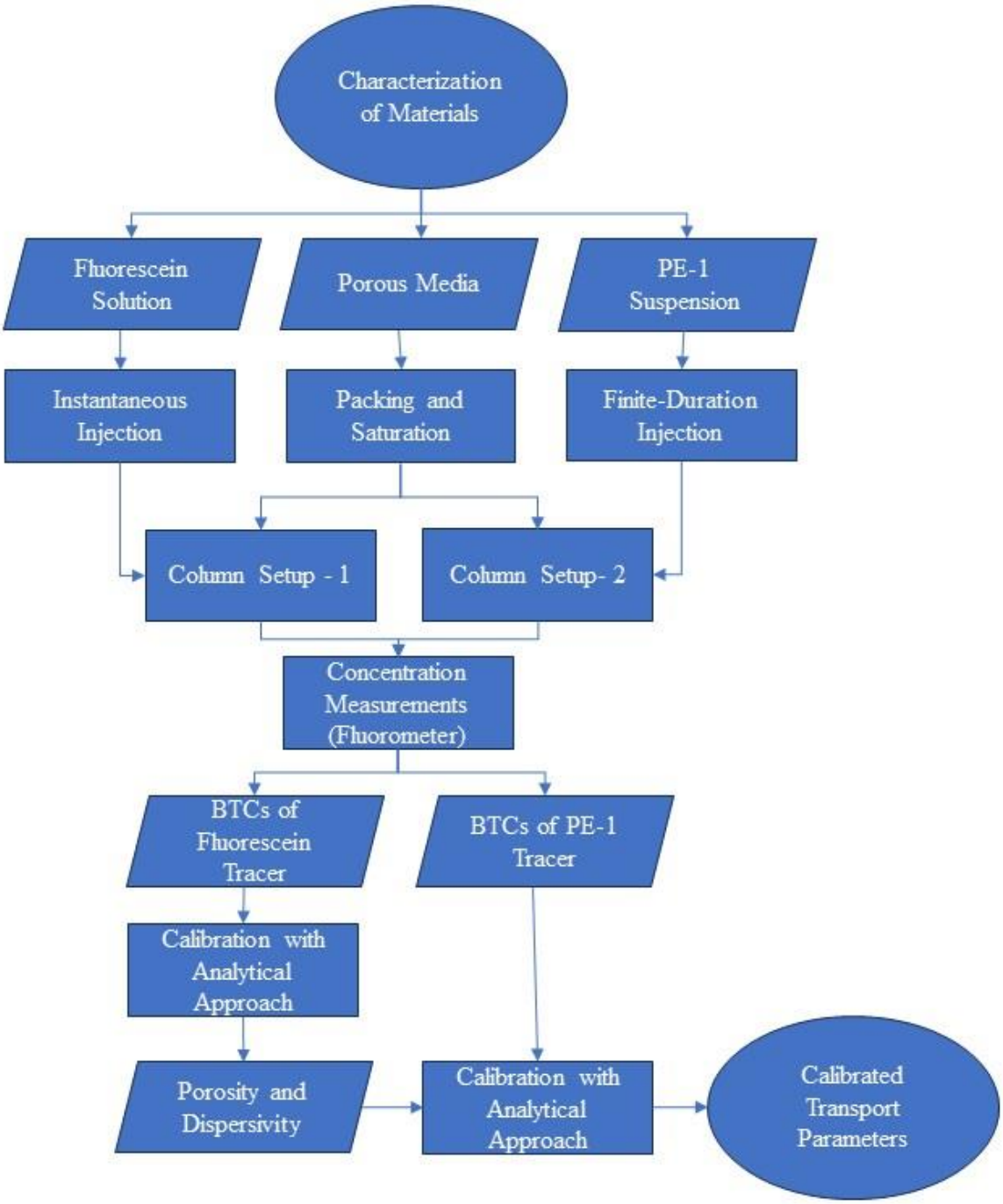
Figure 2.13. The calibration curve to calculate the concentration of PE-1 MPls from fluorometer measurements.

For tracing the fluorescent tracer, the Aquaflour® Handheld dual-channel fluorometer and turbidity device with a blue channel for fluorescein tracer (PE-1) and with a green channel for Rhodamine WT (PE-2) tracer was used with 10 mm x 10 mm plastic cuvettes.

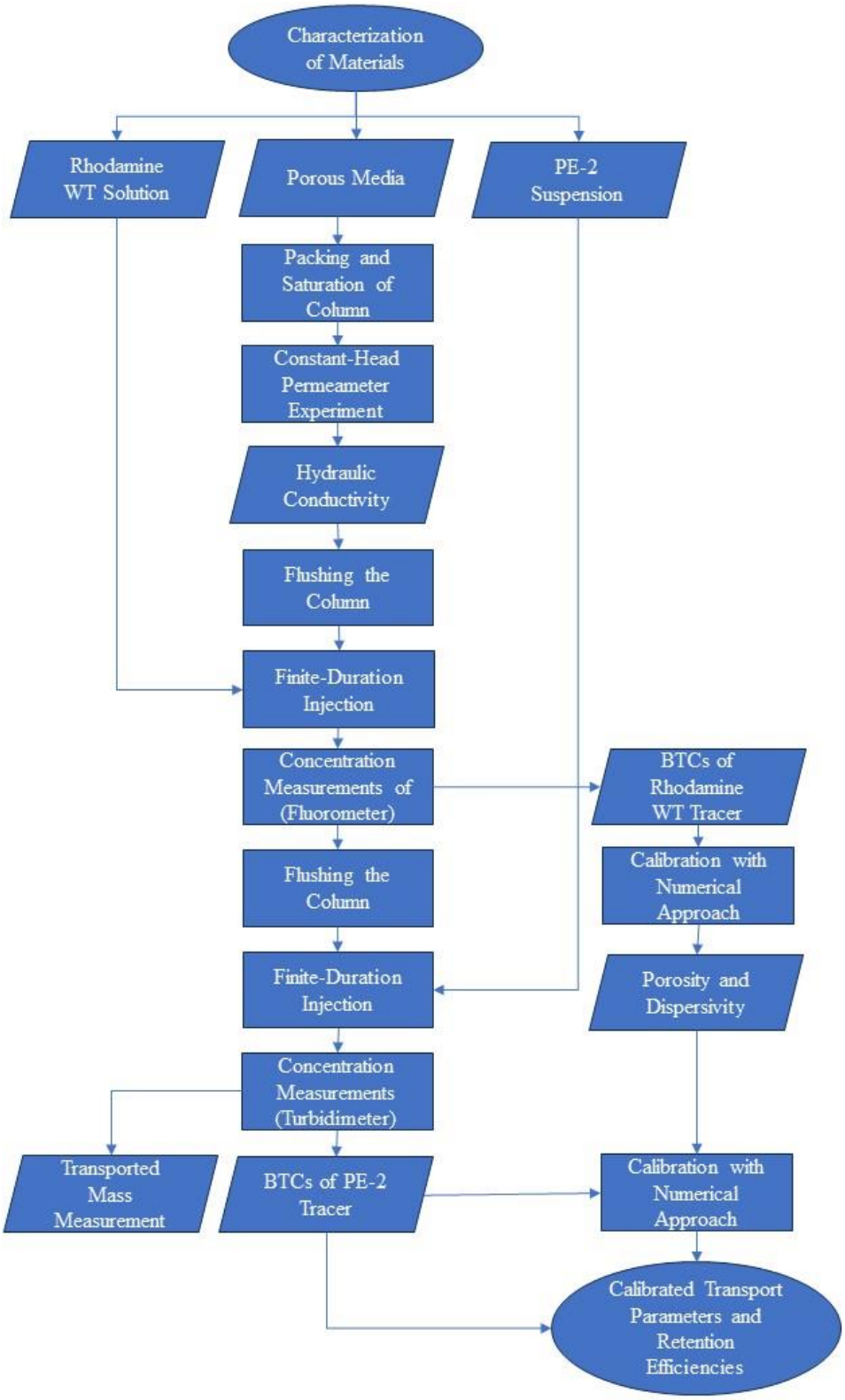
Spectrophotometry involves quantifying the interaction between light and materials, encompassing phenomena such as reflection, transmission, scattering, or absorption of light. UV-visible spectrophotometry was employed to ascertain fluorescein dye concentrations within the porous media, corresponding to experiments involving NPls. To establish a correlation between dye concentration and absorbance, a set of samples including a dye concentration range from 0 to 20 mg/L was meticulously prepared by diluting a specified quantity of stock solution in ultrapure water. Subsequently, the absorbance of each sample was measured at a wavelength of 460 nm. These measurements were conducted using a Hach Lange DR3900 spectrophotometer in a 1 cm path-length quartz cuvette at room temperature. Calibration curves were systematically developed

for all fluorescent dye measurements, facilitating the calculation of dye concentrations during experiments involving the transport of fluorescent dye.

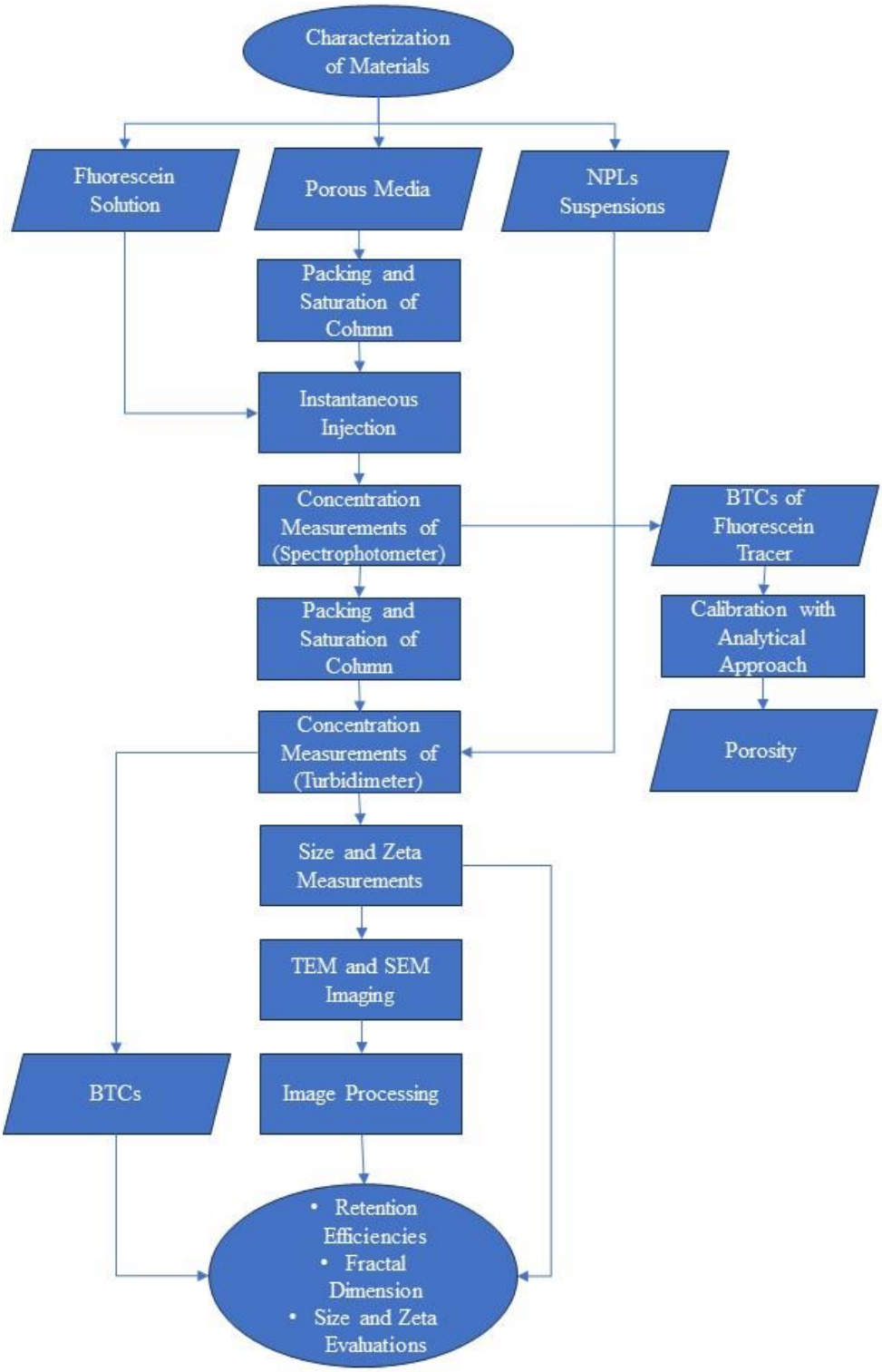
Annex 2.A – Method diagram for the Experiments with PE-1



Annex 2.B – Method diagram for the Experiments with PE-2



Annex 2.C – Method diagram for the Experiments with NPls



CHAPTER 3 - ONE-DIMENSIONAL EXPERIMENTAL INVESTIGATION OF POLYETHYLENE MICROPLASTIC TRANSPORT IN HOMOGENEOUS SATURATED MEDIUM[1]

3.1. Summary

Groundwater serves as a critical global freshwater resource, yet is increasingly threatened by contamination, including MPls pollution arising from both natural and human activities. The widespread use and persistence of MPls presents a significant environmental challenge. While much attention has been directed toward understanding MPls pollution in marine environments, research on its behavior in soil and porous media remains limited.

Addressing this gap, the present study aims to investigate the hydrodynamic transport parameters through saturated porous media with and without MPls. Specifically, it focuses on using PE as a contaminant, with densities ranging from 0.88 to 0.96 g/cm^3 and particle sizes of 200–500 µm. Various porous media, such as large and small silica balls, sand, and coarse gravel, were utilized to test different grain sizes and porosities.

All the experiments took place within the laboratories situated at the University of Poitiers, France. Column experiments were conducted under steady flow rates, with PE-1 particles injected for a finite duration using a suspension created by mixing ethanol and distilled water to lower the density. Fluorescent tracer experiments were performed alongside MPls injection tests, with a laboratory fluorometer used to measure plastic concentrations indirectly.

Analytic breakthrough curves generated by the one-dimensional advection–dispersion equation (ADE) were fitted to experimental data, allowing for the determination of hydrodynamic parameters using an inverse solution method. The results indicated that PE-1 particles of 200–500 µm size did not transport effectively through large silica, small silica, or sand due to pore size limitations, although asymmetrical porosity distribution and the presence of small pores should be considered. Coarse gravel with larger pore size showed potential for PE-1 MPls particle transport, with comparable hydrodynamic transport parameters to fluorescent tracer results.

It is emphasized that the investigation of MPls transport in groundwater is novel and crucial due to the potential risk of groundwater contamination. The study's findings suggest that mean velocity is a critical parameter influencing PE particle transport in saturated porous media, with particles

[1] This chapter was published as *"Okutan, H.M.; Sağir Ç.; Fontaine, C.; Nauleau, B.; Kurtulus, B.; Le Coustumer, P.; Razack, M.; One-Dimensional Experimental Investigation of Polyethylene Microplastic Transport in a Homogeneous Saturated Medium. Frontiers in Environmental Science 2022, 10:885875. https://doi.org/10.3389/fenvs.2022.885875"*

unable to transport effectively at mean velocities below 2.02 cm/min. Future research directions include studying retention parameters, effects of different media and solution mixtures, and implementing advanced numerical modeling for deeper analysis. Additionally, experiments using smaller PE particles with various media will be conducted to better understand transport processes, and the ratio between PE particle size and medium pore/grain size will be investigated to assess suitable transport conditions.

Overall, the study contributes to understanding the behavior of MPls porous media that may represent the subsurface groundwater environments and underscores the importance of further research in this area to mitigate the potential environmental impacts of plastic pollution.

One-Dimensional Experimental Investigation of Polyethylene Microplastic Transport in Homogeneous Saturated Medium

Hande Mahide Okutan[*1,3], Cagdas Sagir[2], Claude Fontaine[2], Benoît Nauleau[2], Bedri Kurtulus[3], Philippe Le Coustumer[1,4] and Moumtaz Razack[2]

[1]EA CNRS 4592 Géoressources & Environnement, Université Bordeaux Montaigne, Pessac, France
[2]Department of Hydrogeology, University of Poitiers, IC2MP UMR CNRS 7285, Poitiers, France
[3]Geological Engineering Department, Mugla Sitki Kocman University, Mugla, Turkey
[4] Bordeaux Imaging Center UMS 3420 CNRS-INRA, Université de Bordeaux, Bordeaux, France
***Correspondence:** Hande Mahide Okutan

Keywords: microplastics; pollution; transport; porous medium; one-dimension; tracer tests; column tests

Abstract

Plastics are widely used in every part of life. Microplastics (MPls) are classified as emerging contaminants in nature. Yet, microplastic transportation parameters in groundwater are not characterized well. In this study, microplastic transport in saturated homogeneous mediums was investigated. For this purpose, one-dimensional column tests were performed using the fluorescent and microplastic tracers to figure out the hydrodynamic conditions for the microplastic transport. Large silica, small silica, sand, and coarse gravel were the tested mediums. The hydrodynamic transport parameters were calculated by inverse solution methodology using the experimental and the analytical solution results. Only the coarse gravel medium with a minimum 1 mm and maximum 20 mm (5 mm of median) pore sizes and kinematic porosity 40.2% were found to be suitable for the transport of the used polyethylene (PE) whose particle size was between 200 and 500 µm. It is not possible to transport PE particles of selected size from fine-grained media. Transportation occurred in coarse-grained media such as coarse gravel. The calculated dispersivity values for the coarse gravel were 2.58 cm and 3.02 cm by using fluorescent and PE tracers, respectively. The experiments showed that the used PE particles cannot be transported if the mean flow velocity is lower than 2.02 cm/min in the coarse gravel medium. The microplastic accumulation might be an issue for an actual aquifer rather than the transportation of it considering the actual groundwater flow velocity is generally much lower.

3.2. Introduction

Groundwater is an important freshwater source that can be directly used as drinking water and constitutes 97% of global freshwater resources. Contamination of groundwater can be caused by the natural presence of fluoride and arsenic or by human activities such as industry, agriculture, etc. The most common groundwater pollutants that threaten human health are pathogens and chemical hazards (World Health Organization, 2006).

Plastics have become indispensable in daily life with their easy accessibility and long-term use. At the same time, its abundant usage and long life make them frequently encountered pollutants in the environment. The size classification of plastic varies depending on the studies. Microplastics are specified as smaller than 5 mm in diameter according to GESAMP (2015). Windsor et al. (2019) also defined the size distribution of microplastics as 0.0001 mm to 5 mm according to their review research. Direct releasing of the micro size-plastic products and fragmentation of large plastics are the sources of the microplastics (MPls). These sources are called primary and secondary, respectively. Primary MPls are used in personal care products, toothpaste, detergents, and hygiene products. Fragmentation and gradual deterioration of the large plastics by various organic and inorganic processes create secondary MPls. These processes include ultraviolet radiation-based photodegradation, mechanical abrasion, and biological effects (Ivar do Sul & Costa, 2014; Waldschläger et al., 2020; P. Wu et al., 2020). The effect of primary and secondary MPls and current knowledge were compiled in view of the marine environment (Ivar do Sul & Costa, 2014). The source of primary and secondary MPls and the generation of secondary MPls were explained by Waldschläger et al. (2020).

MPls are emerging contaminants. They have been detected in marine, terrestrial, and atmospheric ecosystems. The first studies about microplastics were conducted in the marine environment. The following studies dominantly discussed microplastic contamination in the marine environment (Law & Thompson, 2014; Thompson, Olson, et al., 2004). One of the first studies by Thompson et al.(2004) presented spatial distribution and accumulation of polymers while identifying their types in the marine environment, northeast Atlantic. The rising occurrence of MPls and their sources in the marine environment was mentioned and pointed out while concerning the removal of MPls by reducing their consumption. The mass of the terrestrial-sourced plastics in the oceans from the major plastic producing and consuming countries was estimated at 7.7 million tons (MT) at least (Sarkar et al., 2022). MPl pollution in groundwater is not a fully enlightened subject, but studies in this area are increasing. Panno et al. (2019) calculated the average concentration of MP as 6.4 particles per liter and the maximum concentration as 15.2 particles per liter by analyzing the samples from some karst regions in the USA. Mintenig et al. (2019) detected a maximum of 7 particles per liter for the groundwater that was treated and injected through underground.

There are some studies about the migration of MPls in porous media. Porous media makes possible the migration of small particles and dissolved materials. Besides the expected accumulation of MPls in the soil, the particles could migrate vertically by the physical and chemical effects of water

infiltration, fauna activities, and root growth (H. Li et al., 2021; Maaß et al., 2017; O'Connor et al., 2019; Rillig et al., 2017). The studies concerning in fate of MPls in the soil environment are limited and evaluation requires. More studies are needed on the transport, distribution, and degradation of MPls in the soil, especially in terms of environmental impacts in agricultural areas (Kumar et al., 2020).

Higher MPl concentration makes the particle transport higher. Also, the effect of concentration decreases upon the flow rate decrease. Researching the effect of changes in the size of MPls on transport and retention, it has been revealed that for porous media-saturated in seawater salinity, the transport decreases with the increase in the size of MPls. Mobility has weakened due to aggregation. It has been observed that the transport in environments with different salinities is directly related to the size of the MPls (Z. Dong et al., 2018).

Chu et al. (2019) and Hou et al. (2020) studied the effect of zeta potential and ionic strength of the background solution on transportation MPls in saturated media. Zeta potential becomes less negative for both MPl particles and glass balls as porous media, while the ionic strength of the background solution gets higher. The higher ionic strength leads to higher attachment efficiency of MPls (Chu et al., 2019). Studied zeta potential and ionic strength effect on transportation MPls in saturated media. Higher MPl concentration makes the particles transport higher. Also, the effect of concentration decreases upon the flow rate decrease. MPl retention is higher in a medium particle-sized porous media (1-2 mm) than in a large particle-sized porous media (2-4 mm) because of the decrease in pore sizes. As the size of the material constituting the porous medium decreases, the retention/accumulation increases because the surface area that the transported particles contact with the material during transport increases. With the increase in the ionic strength of the background solution, the penetration of the MPl particles decreases in the quartz sand porous media. The transport ability of the MPl particles decreases if there is fulvic acid in the environment. The presence of fluvic acid strengthens the double layer repulsive forces of plastic particles and porous media. Contrary, the high ionic strength decreases the double layer repulsive forces of plastic particles and porous media leading to an increase in the transport ability of the MPls (Hou et al., 2020). The high density of the MPls may cause higher retention and lower mobility depending on the increase in their gravitational sedimentation (S. Dong et al., 2021). In different ionic strength conditions, the presence of clay and organic matter (NOM), which are natural colloids, in the environment directly affects MPls transport. The presence of clay increased MPls mobility under low ionic strength conditions. However, as clay and MPls formed clusters under high ionic strength conditions, a decrease in mobility was detected. In cases where clay and NOM exist together, it is NOM that has low ionic strength and dominantly affects the transport of MPls. At high ionic strength, Clay and NOM affect the MP transport together and the NOM increases MPls transport (M. Li, Zhang, Yi, et al., 2021).The vertical penetration of the particles with water infiltration varies in saturated and unsaturated porous media. The maximum penetration depth was experimented with as ~7.5 cm (O'Connor et al., 2019). The results of the MP penetration column experiment were used in a model to forecast the potential subsurface transport of MP. The average penetration depth was found 5.24 m by using a historic weather pattern (O'Connor et al., 2019). The penetration in sandy soil and clay loam was compared for aged and new MPls. The penetration depth of MPls

was the same (30 cm) for both media, but the particles reached the same depth faster in sandy soil than in clay loam. The results indicated that there is a possibility of groundwater contamination (Ren, Gui, Wei, et al., 2021; Ren, Gui, Xu, et al., 2021). There are also biological agents to help the transport of the MPls into the soil. It is demonstrated that the presence of earthworms and collembolan species in the soil environment accelerates the vertical transport of MPls (Maaß et al., 2017; Rillig et al., 2017). The mean vertical velocity of the MPls was 0.5 cm per day. The small MPl particles reached deeper zones (Rillig et al., 2017). Li et al. (2021) investigated the effects of plant root growth. They tested several shapes and sizes of MPls particles at different depths with various types of plants. The roots can prevent the movement of MPls particles to deeper zones, which results in topsoil accumulation of MPls (H. Li et al., 2021). MPls transport in a shallow alluvial aquifer was investigated by performing well-pumping tests. The Uranine and MPls tracer experiment was carried out with an injection well and several observation points at a 200 m distance. The observations were continued for six months. The peak concentrations of MPls exceeded the peak concentrations of uranine, especially for long distances. The first detection time for shorter distances was the same for the uranine solution and MPls. When the distance increases, MPls' first arrival time is shorter than the uranine. Also, MPls can travel much more distances compared to uranine (Goeppert & Goldscheider, 2021).

The studies which are focused on the transport of PE particles in porous media often underline the effects of environmental factors, porous media properties, and plastic particle properties. According to Windsor et al. (2019), there is a lack of knowledge about the residence time of plastics in the surface waters and the quantitative assessments of the transport pathways from land to sea. Also, a significant absence of studies on microplastic presence and transport in the soil/porous environment must be underlined (Bläsing & Amelung, 2018; J. Li et al., 2020). It is essential to clarify how the MPl particles are transported and dispersed through porous media. The hydrodynamic transport parameters of the porous media need to be assessed by using MPls and compared with those found by using the common traditional tracers. That will give detailed information on the possible contamination of groundwater.

This study aims to determine the hydrodynamic transport parameters of saturated porous media by using PE to understand the transport mechanism of the plastic particles. The existing solute transport analytical solutions were used and tested to see whether they are also valid for MPls transport. For this purpose, 1-D column experiments were performed with a conventional tracer (fluorescein) and PE tracer. Then, the solute transport analytical solutions were applied. The equations were chosen according to the injection type; instantaneous and finite-duration injections for uranine and PE, respectively. At last, the inverse solution was applied to the analytical solutions to achieve the hydrodynamic parameters.

3.3. Material and Method

3.3.1. Properties of the PE Particles

The type of MP used in this study was polyethylene (PE). The density of the PE is between 0.88 and 0.96 (Hüffer et al., 2019; O'Connor et al., 2019; Rillig et al., 2017). The PE grains between 200-500 µm were set apart by using the sieves. The grain sizes of this PE were measured by Zeiss Primostar optical microscopy and ZEN 2.6 Primostar software. The grain size statistics and the histogram of the used PE particles are given in Table 3.1. and Figure 3.1., respectively.

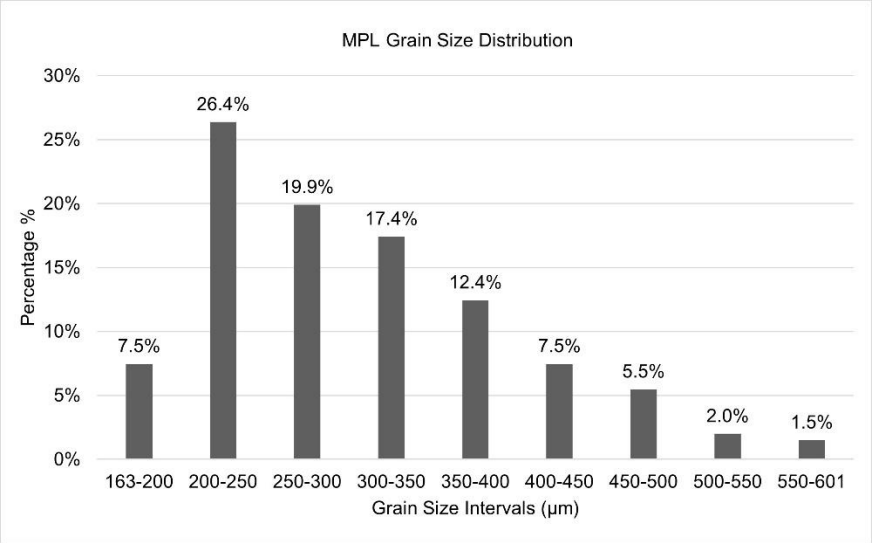


Figure 3.1. The grain size histogram of the used PE.

Table 3.1. General descriptive statistics of the grain size of the used PE, in µm.

Maximum	Quartile 3	Mean	Median	Quartile 1	Minimum	St. Deviation
601	357	308	294	233	163	91

7.5% of the grains were smaller and 3.5% of the grains were higher than the used sieve gap sizes which were a minimum of 200 µm and a maximum of 500 µm. Scanning electron microscopy (SEM) was used to identify the shape and the surface morphology of the PE particles was irregular and rough so they can be called fragments (Figure 3.2.). If the pore size and the grain size of the saturated porous medium are too small for the movement of the plastic particles, straining will occur. According to the studies on pore straining, the diameter of the particles should not exceed 5-10% of the porous medium grain diameter to avoid the pore straining (DeNovio et al., 2004).

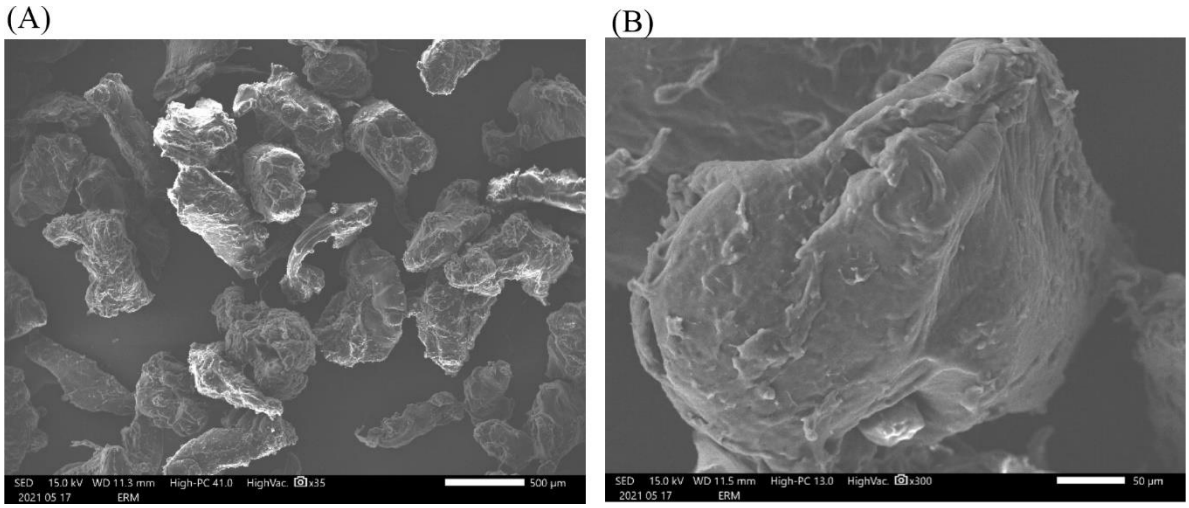


Figure 3.2. SEM micrographs of the MP: (A) shape and size distribution; (B) detail of rugged PE particles.

3.3.2. Properties of the Porous Medium Materials

In order to test different grain sizes and porosities large silica balls, small silica balls, sand, and coarse gravel materials were used in the experiments (Figure 3.3.). For the pore size and grain size measurements of large silica, small silica, and sand, the materials were mixed with resin in a plastic holder and left to dry. Then the dried samples were cut horizontally near the bottom. The bottom sides of the samples were examined with an optical microscope to measure the pore and grain sizes. The particle size of the coarse gravel was directly measured with a tape measure. For the pore size measurements of the coarse gravel, pore sizes were directly measured on the column filled with the material. Between 40-90 measurements were performed for each material to obtain reliable pore/grain size distribution of each used material.

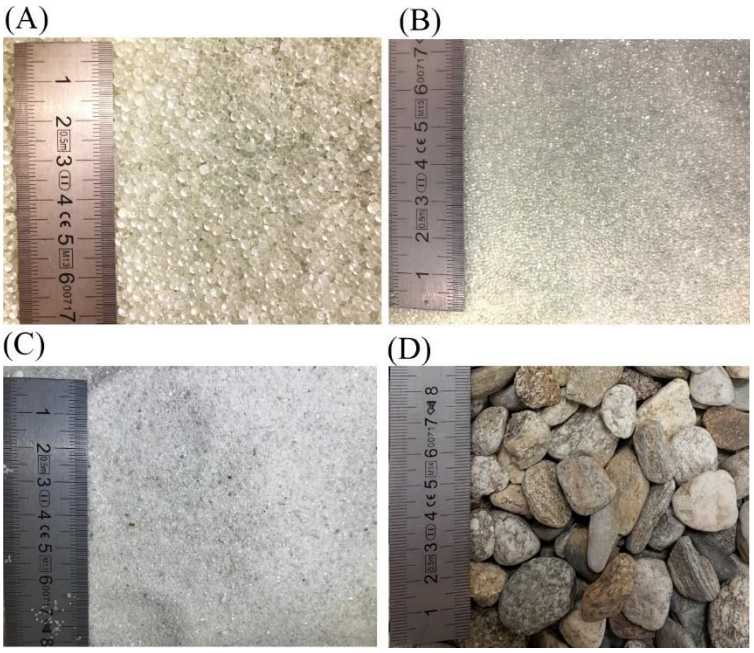


Figure 3.3. The porous medium materials for the column tests: (A) large silica balls; (B) small silica balls; (C) sand; (D) coarse gravel

Depending on the magnification of the optical microscopy, image resolution changes. The smallest measurable pixel sizes for the images of the large silica, small silica, and sand were 213 µm, 206 µm, and 211 µm, respectively. 58% of the pores were higher than 800 µm and 97% of the pores were higher than 400 µm for the large silica. 93% of the pores were higher than 300 µm for the small silica. 78.6% of the pores were higher than 300 µm for the sand. Coarse gravel pore size varied between 1 mm to 20 mm (Table 3.2. and Annex Figure 3.S1.).

Table 3.2. General descriptive statistics of the pores size of the porous medium materials.

	Maximum	Quartile 3	Mean	Median	Quartile 1	Minimum	St. Deviation
Large Silica (µm)	2634	1658	1144	1079	510	298	677
Small Silica (µm)	1295	791	655	612	408	282	289
Sand (µm)	763	450	405	398	318	214	117
Coarse Gravel (mm)	20.0	7.0	6.0	5.0	3.0	1.0	3.5

According to the grain size distributions of the porous medium, the most dominant grain size intervals for the large silica, small silica, sand, and coarse gravel are 1700-2000 µm, 1000-1100 µm, 400-800 µm, and 23-28 mm, respectively (Table 3.3. and Annex Figure 3.S2.).

Table 3.3. General descriptive statistics of the grain size of the porous medium materials.

	Maximum	Quartile 3	Mean	Median	Quartile 1	Minimum	St. Deviation
Large Silica (µm)	3075	2038	1950	1865	1716	1205	404
Small Silica (µm)	1366	1109	1051	1055	989	705	127
Sand (µm)	1372	710	627	613	505	212	204
Coarse Gravel (mm)	47.0	31.0	27.4	27.0	23.0	16.0	6.5

3.3.3. Fluorescent Tracer Column Tests

The fluorescent tracer experiments were performed by vertically placed columns under a steady flow rate within the saturated medium to investigate the hydrodynamic parameters of the porous medium materials used in this study. The experimental setup is given in Figure 3.4. The *X* indicates the distance from the injection point to the top of the material. L_1 indicates the height of the material. L_2 is for the length of the small outlet tube, which indicates the distance from the top of the material to the water sampling point. R_1 and R_2 are the diameter of the column and the diameter of the small outlet tube, respectively. The experimental system was cleaned after each experiment. The parameters of the experimental setup are given in Annex Table 3.S1.

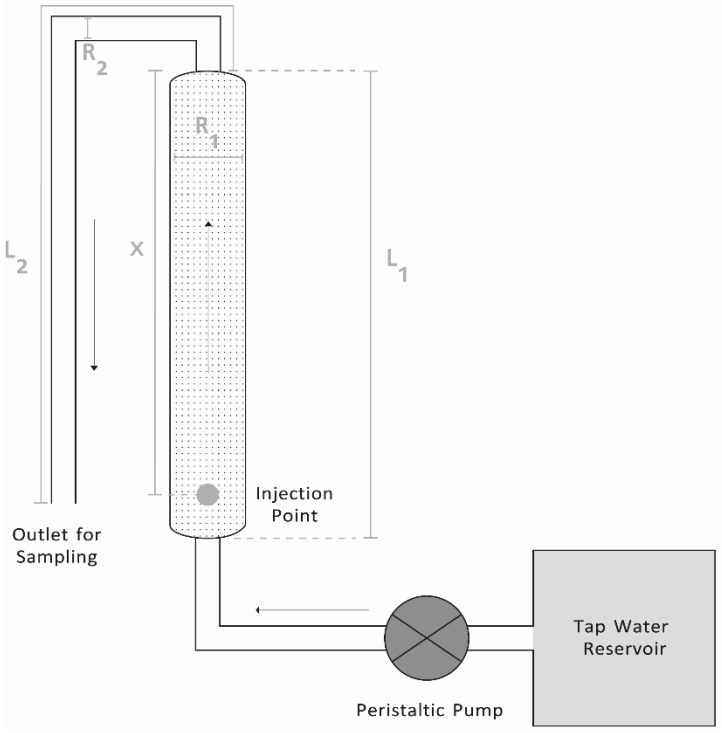


Figure 3.4. Experiment setup for the fluorescent tracer tests.

The experiment started with calculating the density of the materials and their total porosities to determine the mean transit time of the water in the column. A volumetric flask was used for the density measurements. The material of known volume was filled with water and the volume of the used water was measured then the ratio between these volumes was calculated for the total porosity measurements. The mean transit time was calculated by Equation (3.1) and Equation (3.2) in order to decide the start time and the intervals of the water sampling/fluorescent measurement (Fetter, 2014).

$$T = \frac{X}{u} \tag{3.1}$$

where;

T: Mean transit time (time)

X: Distance from injection point (distance)

u: Mean velocity (distance/time)

$$u = \frac{Q}{A * n} \tag{3.2}$$

where;

u: Mean velocity (distance/time)

Q: Flowrate (volume/time)

A: Cross-sectional area (area)

n: Total porosity (dimensionless, ratio)

AquaFluor® Handheld Fluorometer (Turner Designs) was used for the fluorescent measurements of the samples. At the beginning of each experiment day, the fluorometer was re-calibrated and the fluorescein (uranine) injection solutions were prepared. For the calibrations, 300 µg/L solutions were used and equaled 300 units on the fluorometer. The injection solution was prepared at 0.2 g/L concentration. Minimum 3 injections/experiments were done for each material. The experiments were implemented by different flow rates and volumes of injected tracer. The flow rates (Q) and injected volumes (V_{inj}) were given in Table 3.4.

Table 3.4. The flow rates (Q) and injected tracer volumes (V_{inj}) for the fluorescent tracer tests.

	Large Silica		Small Silica		Sand		Coarse Gravel	
Exp. No	Q (cm^3/min)	V_{inj} (mL)	Q (cm^3/min)	V_{inj} (mL)	Q (cm^3/min)	V_{inj} (mL)	Q (cm^3/min)	V_{inj} (mL)
1	29.13	0.19	42.20	0.21	50.82	0.17	31.86	0.19
2	49.29	0.27	22.30	0.10	39.83	0.26	60.21	0.39
3	21.02	0.30	54.36	0.27	29.15	0.15	103.31	0.29
4	44.32	0.15	29.42	0.14	20.78	0.12	-	-

The longitudinal dispersivities and the kinematic porosities of the porous medium materials were calculated using the inverse solution method. One-dimensional advection-dispersion equation (ADE) was used to have analytic breakthrough curves (BTC) (concentration/time). Then these analytically calculated curves were fitted to the BTCs that were created by the fluorescent measurements of the outlet samples. The fitting process was applied by Solver Add-in of Excel application. This application allowed to modify the dispersivity, kinematic porosity, and mean velocity to get the best fit by an iterative process. The dispersivity and kinematic porosity were achieved by calculating the average of the results of the multiple experiments for each material and condition.

Under steady-state flow and saturated conditions in a homogeneous porous medium, the transport of suspended particles can be described by the advection and dispersion equation (3.3) (Bear & Cheng, 2010).

$$\frac{\partial C}{\partial t} = D_L \frac{\partial^2 C}{\partial x^2} - u \frac{\partial C}{\partial x} \tag{3.3}$$

where;

$\partial C/\partial t$: Solute concentration change over time (concentration/time)

C: Solute concentration (mass/volume)

D_L: Longitudinal dispersion coefficient (area/time)

X: Distance (distance)

u: Average linear water velocity (distance/time)

The longitudinal dispersion coefficient is a linear function of the average velocity and dispersivity of the porous medium. It was defined as under saturated conditions by Bear (1988) and given in Equation (3.4).

$$D_L = D_e + \alpha_L v \tag{3.4}$$

where;

D_L: Longitudinal dispersion coefficient of the medium (area/time)

D_e: Effective dispersion coefficient of the medium (area/time)

α_L: Longitudinal dispersivity (distance)

v: Average flow velocity (distance/time)

The velocity of the groundwater ranges between 1 cm/day to 1 m/day. The effect of diffusion in the transport of solutes is negligible for the flow in a saturated porous medium for most of the studies (Raaijmakers, 2018). The tracer injection was implemented instantaneously. The length of the small outlet tube from the top of the material to the outlet where the samples were taken was measured and considered as only advective transport was valid there.

The recovered mass was calculated with the assumption of zero mass loss. The recovered mass was used in the analytical solution of the 1D advection-dispersion equation as initially injected mass. Equation (3.5) was used to calculate the recovered mass (Goldscheider & Drew, 2007).

$$m_R = Q \int_0^{\infty} c(t)\partial t = Q \times \sum [c(t) \times \Delta t] \tag{3.5}$$

where;

Q: Flow rate (volume/time)

c(t): Tracer concentration by time (mass/volume)

Δt: Timestep (time)

The ADE for instantaneous injection under the assumptions of the 1D, semi-infinite, isotropic, and homogeneous porous medium was used to create analytical BTCs (Kreft & Zuber, 1978) (3.6).

$$C_i(x,t) = \frac{M_0\, x}{A\, n\, u_x \sqrt{4\pi D_x t^3}} \exp\left(-\frac{(x-u_x t)^2}{4D_x t}\right) \tag{3.6}$$

where;

C_i: Concentration at the sampling point (mass/volume)

M_0: Recovered mass (mass)

x: Distance between the sampling point and the injection point (distance)

u: Mean velocity (distance/time)

D: Dispersion coefficient (area/time)

t: Time (time)

A: Cross-sectional area (area)

n: Total porosity (dimensionless, ratio)

3.3.4. Microplastic Tracer Column Tests

A new Plexiglass column and experiment setup were built for this study. The length and the inner diameter (R_2) of the column were 100 cm and 8 cm, respectively (Figure 3.5). The column was filled with the materials and then saturated. The PE particles were injected for a finite duration with a constant flow rate. The porous mediums were assumed as isotropic and homogenous. When the column is filled, X indicates the length of the porous medium. L_1 is the distance between the

sampling point and the outlet of the column. L_2 is the distance between the PE suspension reservoir and the inlet of the column. Only advective transport was considered for L_1 and L_2.

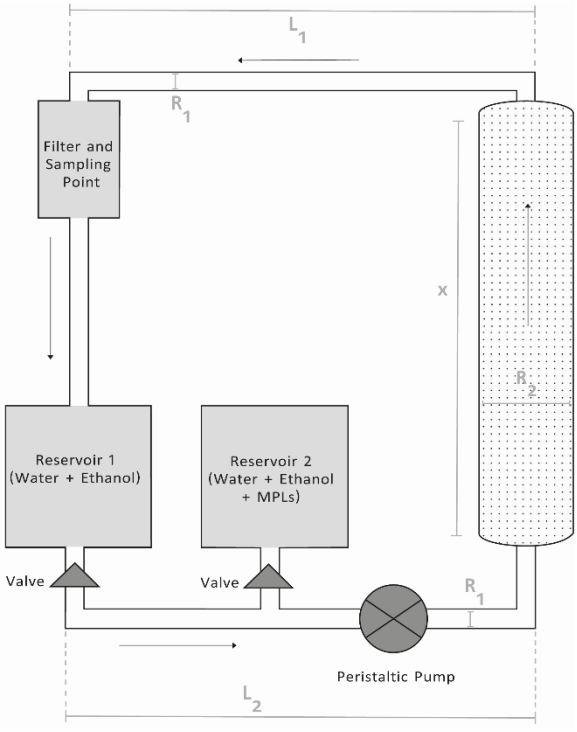


Figure 3.5. Experiment setup for the microplastic tests.

The density of the PE particles is lower than the distilled water. A suspension was needed for the homogenous injection of the MPl. Ethanol and distilled water were used to create a lower-density liquid. The ethanol and distilled water ratio were determined as 56% and 44%, respectively. The density of this liquid mixture was around 0.87 g/cm^3. PE particles were successfully suspended within this liquid matrix. The column and the circulation system were built considering to minimize the evaporation of the ethanol.

The column was filled with the material and the ethanol-distilled water mix (Reservoir 1) was circulated for a while to saturate the porous medium. After the steady-state flow conditions were achieved, the valve of Reservoir 1 was closed, and the valve of the Reservoir 2 was opened at the same time to start the finite duration MPl injection. The experimental system was cleaned after each experiment.

The PE concentration of the injection suspension injected volume, and mean flow rate for each experiment were shown in Table 3.5.

Table 3.5. Parameters of the tests with PE.

Large Silica				Coarse Gravel		
Exp. No	Q (cm^3/min)	V_{inj} (cm^3)	C_{inj} (g/L)	Q (cm^3/min)	V_{inj} (cm^3)	C_{inj} (g/L)
P1	70	1120	24	40.59	2029.5	20
P2	104.8	524	10	153.84	2307.6	20
P3	206.3	2062.8	10	-	-	-

TD-700 Laboratory Fluorometer (Turner Design) with a blue channel was used to measure the plastic concentrations of the samples. A fluorometer was used because it was determined that the PE particles have a certain level of reflectance for the blue channel. Yet, this was an indirect measurement. So, the inversion of the fluorometer measurements was performed. The inversion equations were found to convert the device measurements to the plastic concentrations. Six PE suspensions of known concentrations were prepared. These suspensions were measured by the fluorometer. The PE concentrations were plotted versus device measurements. A trendline with an equation was defined (Figure 3.6.). These equations were used to convert the device measurements to the PE concentrations. The samples were collected in tubes with a cap to avoid the evaporation of the ethanol. PE concentrations of the samples were measured after the end of the experiment.

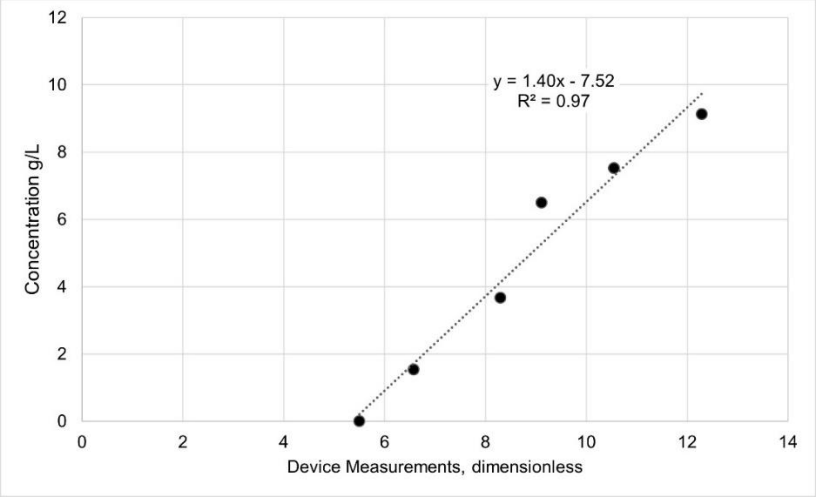


Figure 3.6. The equation for the inversion of the fluorometer measurements to PE concentrations.

The same principles with the solution method of the fluorescent tracer experiment were used also for the tests with PE (Equations (3.3),(3.4), and (3.5)) (Bear, 1988; Bear & Cheng, 2010; Goldscheider & Drew, 2007). Only the longitudinal dispersion was considered. The porous mediums were assumed as isotropic and homogeneous. The 1D ADE equation for finite duration injection by Ogata & Banks (1961) with the assumptions of the 1D, semi-infinite, isotropic, and the homogeneous porous medium was used (3.7). A similar procedure - the fluorescent tracer tests solution for the inverse modeling by using Solver Add-in on Excel - was applied for the PE tests with the additional modifiable parameters (concentration injected and injection time).

$$C = \frac{C_0}{2}\left[erfc\left(\frac{L - v_x t}{2\sqrt{D_L t}}\right) + \exp\left(\frac{v_x L}{D_L}\right) erfc\left(\frac{L + v_x t}{2\sqrt{D_L t}}\right)\right] \quad (3.7)$$

where;

C: solute concentration (mass/volume)

C_0: initial solute concentration (mass/volume)

L: flow path length (distance)

v_x: average linear water flow velocity (distance/time)

t: time since the injection of the solute (time)

D_L: longitudinal dispersion coefficient (area/time)

3.4. Results and Discussion

3.4.1. Fluorescent Tracer Column Tests

The fitted experimental and the analytical fluorescent tracer concentration BTCs for each medium and each column test were given in Annex Figure 3.S3. The recovered mass was calculated with Equation (3.5) and was used as an injected mass while doing analytical solution (Table 3.6.). The results of the fluorescent tracer column tests, kinematic porosity (n_k), and dispersivity (α) values for each medium were given in Table 3.7.

Table 3.6. Fluorescent tracer column test results: Recovered Mass, M_{rec} (µg)

	Recovered Mass, M_{rec} (µg)			
Exp. No	Large Silica	Small Silica	Sand	Coarse Gravel
T1	52.6	39.4	51.4	76.2
T2	57.9	17.5	75.3	149.3
T3	63.6	82.4	44.2	100.3
T4	32.5	31.2	35.3	-

Table 3.7. Fluorescent tracer column test results: the kinematic porosity (nk) and dispersivity (α) values for the mediums.

	Large Silica		Small Silica		Sand		Coarse Gravel	
Exp. No	α (cm)	n_k (%)	α (cm)	n_k (%)	α (cm)	n_k (%)	α (cm)	n_k (%)
T1	0.31	41.3	0.10	43.0	0.060	32.3	2.79	40.3
T2	0.25	40.8	0.11	39.5	0.060	31.5	2.67	39.6
T3	0.27	43.1	0.12	40.7	0.058	31.1	2.29	40.6
T4	0.26	42.1	0.09	39.8	0.056	29.5	-	-
Mean	0.27	41.8	0.10	40.7	0.06	31.1	2.58	40.2

Concentration measurements were initiated at the beginning of the first sample collection. However, the sampling was faster than the measurements. This caused a waiting time for most of the samples up to 10 minutes. It is expected that a certain level of fluorescent activity might have diminished during this period depending on the sensitivity of the fluorescent to the light.

The injected mass and the recovered mass were accepted as equal, based on the assumption that there wasn't any mass lost. The recovered mass was calculated using the sample measurements. The above-mentioned error in the sample measurements might have been valid for the calculations made by using recovered masses also.

3.4.2. Microplastic Tracer Column Tests

The PE particles didn't transport up to the outlet of the column in the materials of small silica and sand. The MPls settled down at the very beginning of the inlet of the column and they clogged the inlet. The MPls were transported successfully through the column in the materials of large silica and coarse gravel.

For the experiment P1 for large silica; the pumping flow rate was 70 cm^3/min, the injection duration was 16 min, the injection concentration was 0.024 g/cm^3, and the injection volume was 1120 cm^3 which was lower than the pore volume (1996.04 cm^3). The injected PE particles clogged the column entrance. There weren't any PE particles in the samples and on the filter. The PE particles didn't transport throughout the column.

In the following experiment P2 for large silica; the pumping flow rate was 104.8 cm^3/min, the injection duration was 5 min, and the injection concentration was reduced from 0.024 g/cm^3 to 0.01 g/cm^3, and the injection volume was 524 cm^3. The PE particles transported up to the first 10 cm from the bottom of the column and then stopped there. There were a very low number of particles found on the filter and in the samples.

The experiment P3 for the large silica; the pumping flow rate was 206.28 cm^3/min, the injection duration was 10 min, the injection concentration was 0.01 g/cm^3 same as the experiment P2, and the injection volume was 2062.8 cm^3. The PE particles transported up to the first 10 cm from the

bottom of the column and then stopped there same as the experiment P2. The amounts of the observed PE particles on the filter and in the samples were higher than those for experiment P2. Yet, the increase in the pumping flow rate didn't create a significant change in the transport of the PE particles.

The injection concentration could not be decreased more because the lower values than 0.01 g/cm^3 cannot be detected by the fluorometer used in this study. When the pore sizes of the porous media are evaluated, it is seen that the distribution graphs are not symmetrical. Therefore, when talking about pore sizes, they should be evaluated by considering maximum, minimum, and standard deviation values instead of average values. According to the pore size measurements of the large silica, it was seen that 97% of the pore sizes were higher than 800 µm while the PE particle size was between 200 and 500 µm. It is determined that the PE particle size and the pore size of the large silica were not suitable for the transport of the particles. The pore size measurement method might have caused a certain level of error. Also, there were not enough amount of PE particles smaller than 200-500 µm to perform further experiments. When column experiments are evaluated, Dong et al. (2021) and Chu et al. (2019) used a combination of 0.25 to 5 µm diameter MPls for 0.35 to 0.45 mm porous media and 1µm diameter MPls with 0.25 to 0.30 mm grain size, respectively. Considering the study of Hou et al. (2020) as the experiment using larger size MPls, it was seen that MPls with 40-48 µm diameter and two different porous media with 1-2 and 2-4 mm grain sizes were used. In this study, MPls with a larger diameter were used. 200 and 500 µm MPls were tested with 1.7 to 2.0 mm and 23 to 27 mm porous media.

Considering the previous results, the experiments were continued with the coarse gravel, which had larger particle and pore sizes than the other materials. The experiment P1 for coarse gravel; the pumping flow rate was 40.59 cm^3/min, the injection duration was 50 min, the injection concentration was 0.02 g/cm^3, and the injection volume was 2029.5 cm^3 which was slightly higher than the pore volume (1910.09 cm^3). The particle movement in the column was very slow. The particles mostly stopped at the bottom half of the column. The pumping flow rate was too low thus the mean velocity of the injection liquid in the column was too slow. The mean velocity of the injection liquid in the column was 2.02 cm/min. It can be said that the 2.02 cm/min and lower velocities are not enough for the transport of the PE particles.

The experiment P2 for coarse gravel; the pumping flow rate was increased to 153.84 cm^3/min, the injection duration was 15 min, the injection concentration was 0.02 g/cm^3, and the injection volume was 2307.6 cm^3 which was higher than the pore volume (1910.09 cm^3). The PE particles were successfully transported throughout the experimental system.

Equation 7 was used for the analytical solution of the P2 experiment to estimate the transport parameters. The analytical BTC was fitted to the experimental BTC by the manipulation of the injected concentration (C_0), injection duration (T_{inj}), dispersivity (α), and mean velocity (u). These four parameters had to be changed by the Solver add-in in order to get a reasonable fit. The fitted BTC were shown in Figure 3.7. The results of the parameters were given in Table 8.

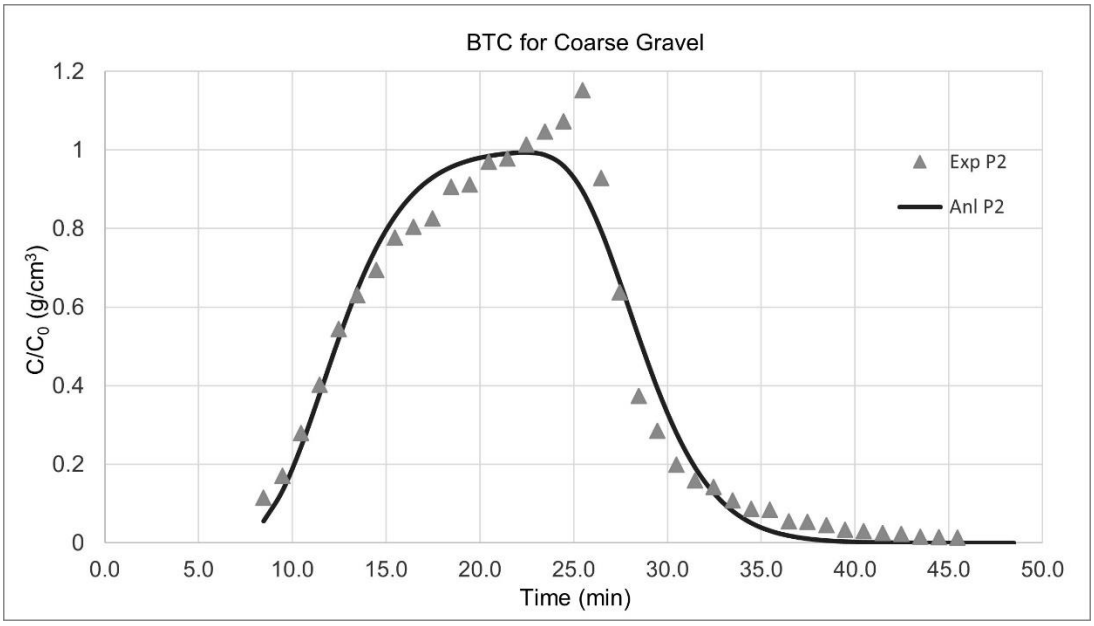


Figure 3.7. BTCs of plastic particle experiment P2 for coarse gravel

Table 3.8. The calculated values of the parameters for the plastic particle experiment P2 for coarse gravel.

Exp. No	C_0 (g/cm^3)	T_{inj} (min)	α (cm)	u (cm/min)	D (cm^2/min)
P2 for Coarse Gravel	0.01	16.4	3.02	7.50	23

The PE experiments resulted in 3.02 cm for the dispersivity of the coarse gravel while the fluorescent tracer experiments resulted in 2.58 cm for the same medium. These values are in the same decimal value, and they are quite similar in terms of assessing the dispersivity of a medium.

The ethanol-water-PE suspension was prepared for the injection in order to avoid the sedimentation of the PE particles in reservoir 2 and the column. The experimental setup was built as close as possible to minimize the evaporation of the ethanol to sustain the stable suspension of the injection. Yet, the experimental setup was open to the atmosphere during the sampling. This might have caused a certain level of evaporation of the ethanol which might change the suspension stability.

For the P2 experiment, the recovered mass was calculated by equation 5 using the measured concentration of the samples. The recovered mass was 26.7 g. According to the Solver add-in fitting, the injected PE amount was calculated as 23.1 g. It was known that the injected/pumped PE mass was 46.2 g. The coherence between the recovered mass and the Solver calculated mass indicates the consistency between the results. The difference between the known injected mass (46.2 g) and the calculated masses (26.7 and 23.1 g) points out that 58-50% of the PE particles must be retained in the porous medium. Also, the relative method for the measurements of the PE samples might have a certain level of error margin on the PE mass calculations even though the recession coefficient of the calibration was found 0.97.

The ADE (Equation 6) employed for the PE tracer test results, is often used for the investigation of the transport of very small particles like fluorescents. In the present study, the PE particle sizes were much bigger than those. The BTCs don't fully/well overlapped/fitted may lead to a discussion of the appropriateness of the ADE for the PE transport.

The transport of the PE particles might have also been affected by the zeta potential (electric charge) between both PE-PE and PE-media. If the particle and porous media have the same electric charge (positive-positive or negative-negative), that would make the PE particles easier to move through the porous medium. The change in ionic strength and pH and the presence of humic acid in the environment are factors that directly effects the zeta potential (Chu et al., 2019; S. Dong et al., 2021). The zeta potential of the particles and porous media was not examined within the scope of this research.

3.5. Conclusion

The investigation of the transport of MPls in groundwater is quite uninvestigated and thus new. According to the literature, the underlying fundamental consequence is that the vertical movement of microplastics may lead to the contamination of the groundwater.

In this study, fluorescent and MP tracers were used in 1D column experiments with different kinds of porous mediums. The 200-500 µm size PE particles were expected to pass through the large silica whose 97% of the pore size is higher than 800 µm. However, the PE particles were not transported in the experiment of the large silica with various parameters. The small silica and sand mediums had smaller size pores and they were found to be not suitable for the PE particle transport. However, the fact that the porosity distribution graphs are not symmetrical, and the presence of small pores should be taken into account. When evaluating the pore size, it needs to be considered by using the maximum, minimum, and standard deviation values.

The coarse gravel with a much larger pore size was used with the same size PE particles. The results of fluorescent tracer and MP tracer were compared. The dispersivity results showed that the values were quite close. It is found that the mean velocity (u) is an important parameter for the transportation of the PE particles in a saturated porous medium. The experiments showed that the PE particles (200-500 µm size) cannot be transported if the mean velocity is lower than 2.02 cm/min. When natural conditions like groundwater in an actual aquifer are considered, the mean velocities are usually quite lower than those in the experiments performed in this study. So, the accumulation of the PE particles in aquifers might be an additional issue and requires further investigation.

For a future perspective, the retention parameters caused by electrical charge need to be studied. Different mediums, solution mixtures, changes in pH, the presence of organic material, and the size of plastic particles need to be taken into consideration in the transportation or accumulation of microplastics. The effect of the change in these factors on transport and accumulation should be

considered individually or according to their co-existence.1D tracer experiments using a smaller size of PE particles with artificial (large silica and small silica) and natural media (sand and gravel) will be performed to further understand the transport processes of the MPls in a saturated porous medium. The ratio between the PE particle size and the pore/grain size of the medium will be investigated to assess the suitable conditions for PE particle transport. Advanced numerical modeling will be implemented to better analyze the experimental data.

Annex 3.A. Supplementary Information

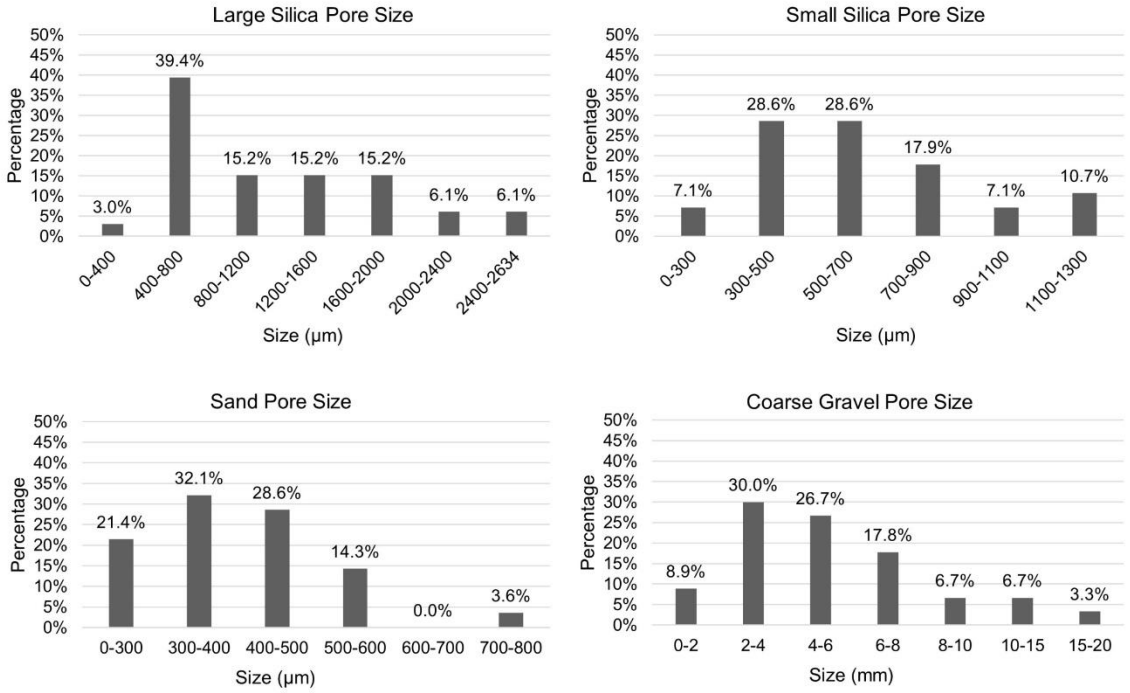


Figure 3.S1. The pore size histograms for the used porous medium materials.

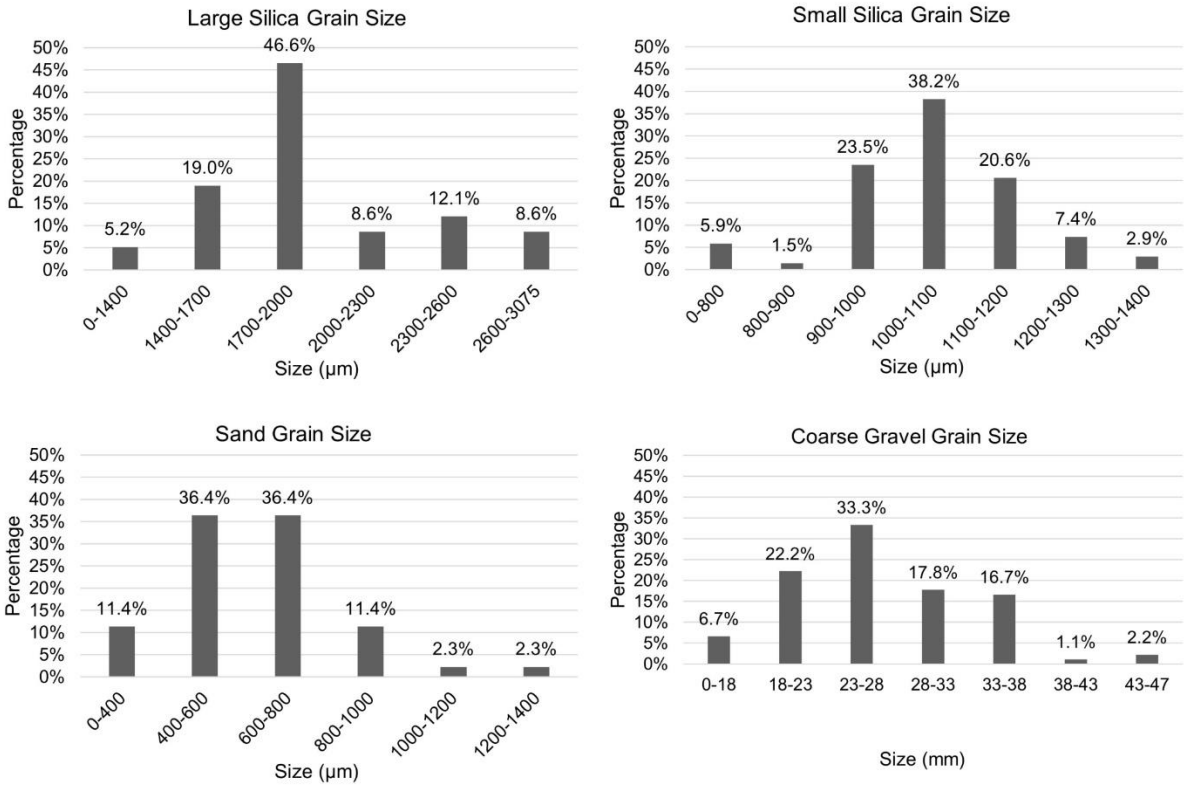


Figure 3.S2. The grain size histograms for the used porous medium materials.

Table 3.S1. Parameters of the experimental setups for the fluorescent tracer tests.

	X (cm)	L1 (cm)	R1 (cm)	L2 (cm)	R2 (cm)
Large Silica	77.3	83.5	5.7	199.5	0.30
Small Silica	76.5	82.6	5.7	200.3	0.30
Sand	77.5	83.8	5.7	199.3	0.30
Coarse Gravel	76.5	80.5	5.7	137.0	0.47

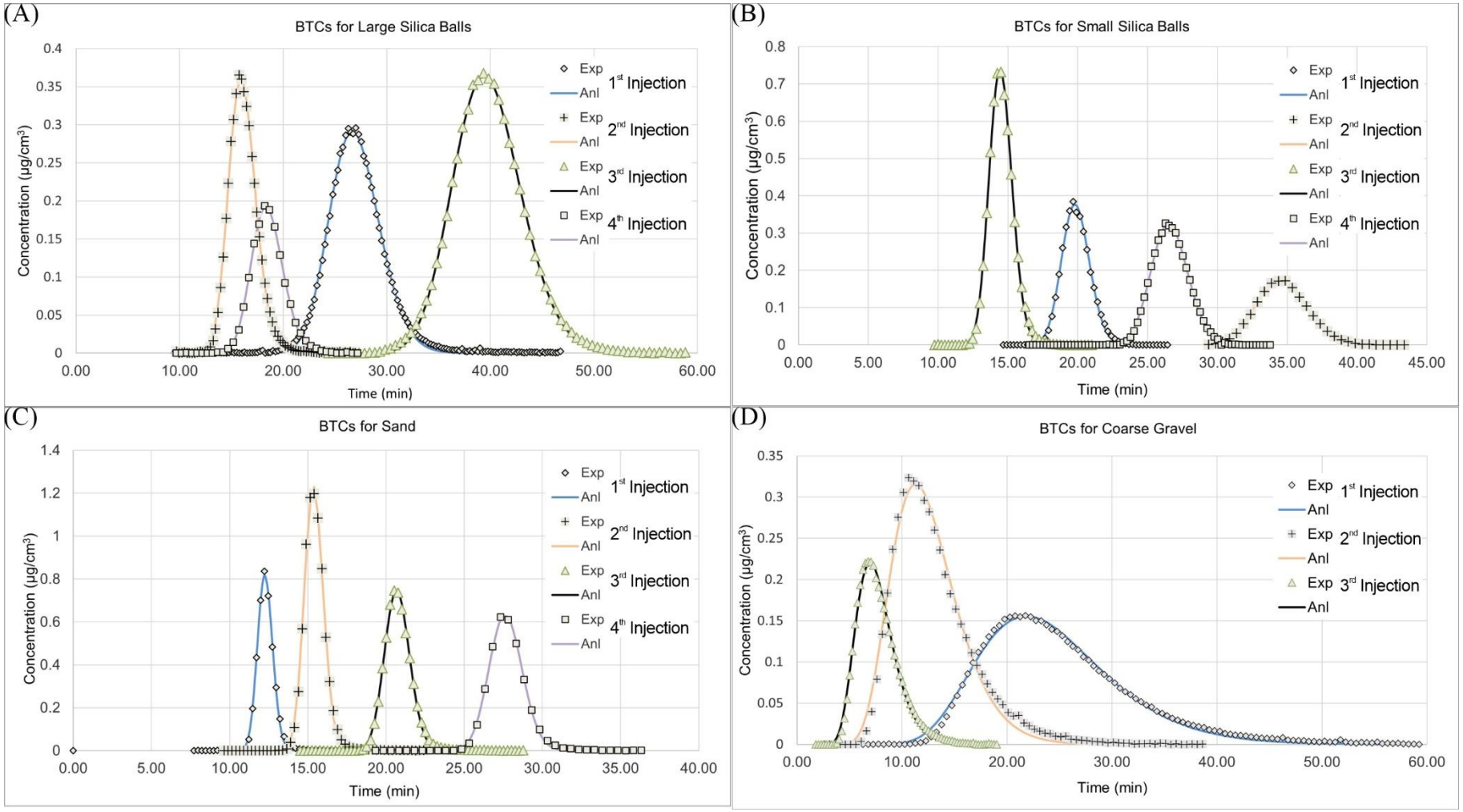


Figure 3.S3. The experimental and the analytical fluorescent tracer concentration BTCs for each medium and each column test: (A) large silica, (B) small silica, (C) sand, and (D) coarse gravel

CHAPTER 4 - UNDERSTANDING MICROPLASTICS RETENTION EFFICIENCY AND SORPTION DYNAMICS IN POROUS MEDIA[2]

4.1. Summary

Plastics have become ubiquitous in modern society, finding extensive use across various sectors. However, their inadequate recyclability, coupled with degradation and abrasion processes, often results in the fragmentation of plastics into smaller pieces, known as MPls, which then find their way into natural environments through diverse transport mechanisms such as wind, runoff, and infiltration. Once released into the environment, these MPl particles pose significant risks to natural ecosystems, including freshwater resources, potentially disrupting delicate ecological balances and harming living organisms.

Groundwater, a vital natural resource, is particularly susceptible to contamination by MPls. The filtration properties of porous media play a crucial role in regulating the quality of groundwater by removing or reducing the concentration of particles and contaminants as water moves through the subsurface. Understanding the intricate filtration mechanisms within porous media is essential for devising effective strategies to mitigate MPl contamination.

The filtration process within porous media involves three key steps: transport, attachment, and detachment. Physical mechanisms such as Brownian diffusion, deposition, direct interception, and hydrodynamics govern particle transport in filter pores. Sorption kinetics play a significant role in the attachment and detachment of particles within porous media, with factors such as flow rate and particle size influencing sorption dynamics.

The experiments were carried out at the Eskisehir Technical University, Türkiye. Experimental setups involved the use of quartz sand as the porous medium due to its widespread use and availability. The determination of sand particle size and hydraulic conductivity provided essential parameters for understanding filtration efficiency. The use of fluorescent dye tracer experiments and numerical modeling allowed for the calculation of effective porosity and dispersivity, further enhancing the understanding of porous media characteristics. Transport experiments conducted in acrylic columns followed a systematic sequence, starting with constant-head permeameter tests to ascertain hydraulic conductivity, followed by dye tracer experiments to evaluate hydrodynamic properties, and concluding with PE-2 MPls (16 ± 6 µm) transport experiments to determine sorption parameters and retention efficiencies. The experiments were conducted at different flow

[2] This chapter was submitted to Nanomaterials MDPI Journal, under review and published as preprint *"Okutan, H.; Sağır, Ç.; Kurtuluş, B.; Özmen, H.B.; Pekkan, E.; Razack, M.; Le Coustumer, P. Understanding Microplastics Retention Efficiency and Sorption Dynamics in Porous Media. Preprints 2024, 2024021670. https://doi.org/10.20944/preprints202402.1670.v1 (Submitted to Nanomaterials MDPI)"*

rates (31 ml min^{-1} and 65 ml min^{-1}) to assess the impact of flow rate on sorption dynamics and filtration efficiency. Numerical modeling using MT3DMS and MODFLOW provided additional insights into MPl transport and sorption kinetics within porous media. Sensitivity analyses allowed for the evaluation of the effects of individual sorption parameters.

The impact of flow rate on sorption was explored, revealing variations in sorption parameters such as distribution coefficient (K_d), mass transfer coefficient (β), and irreversible sorption rate (K_1). The relativity lower flow rates were associated with higher K_d and β values, indicating increased sorption and altered mass transfer rates. Increasing K_d led to more gradual sorption and increased retardation, while changes in β affected the pace of sorption and peak concentration. Flow rate also influenced retained mass, with higher flow rates leading to decreased retention efficiencies, indicating the dominance of advection over retention. Retention rates were assessed at different flow rates, showing average retention rates of 28 ± 1% and 24 ± 2% for numerical modeling and experimental measurements at a flow rate of 31 ml min^{-1}, and 17 ± 1% and 9 ± 4% respectively at a flow rate of 65 ml min^{-1}. The mean absolute error (MAE) of 6% indicated slight differences between predicted and measured retention rates.

The study addressed critical knowledge gaps regarding the transport dynamics of polydisperse, fragmental type, and non-reference PE-2 MPls in porous media. By elucidating the role of sorption kinetics and flow rate on filtration efficiency, the study contributes to the development of strategies to mitigate MPl contamination in groundwater systems. The study's findings revealed that flow rate significantly influenced sorption dynamics, with lower flow rates associated with higher sorption rates and retention efficiencies. The use of numerical models accurately estimated retention rates, albeit with slight discrepancies when compared to experimental measurements. These findings underscore the importance of considering factors such as flow rate, surfactant presence, and particle characteristics in understanding MPl transport in porous media. Understanding these dynamics is essential for developing effective filtration strategies to safeguard freshwater resources. Future studies could consider modifying water properties to better emulate natural systems, contributing to improved freshwater source protection and the development of strategies to safeguard these vital resources.

Understanding Microplastics Retention Efficiency and Sorption Dynamics in Porous Media

Hande Okutan[1,2,3], Çağdaş Sağır[4], Bedri Kurtuluş[1], Hasan Burak Özmen[3], Emrah Pekkan[3], Moumtaz Razack[5], Philippe Le Coustumer[2,6*]

[1]Department of Geological Engineering, University of Muğla Sıtkı Koçman, 48000, Muğla, Türkiye
[2]Sciences et Technologies, Ecole Doctorale, Université Bordeaux Montaigne, 33607, Pessac, France
[3]Institute of Earth and Space Sciences, Eskisehir Technical University, 26555, Eskişehir, Türkiye
[4]Geological Engineering Department, Middle East Technical University, 06800, Ankara, Türkiye
[5]IC2MP UMRCNRS 7285, Université de Poitiers,86073, Poitiers, France
[6]Bordeaux Imaging Center, CNRS UAR3420-INSERM US4, Université de Bordeaux,33076, Bordeaux, France
***Correspondance** : Philippe.le-coustumer@u-bordeaux.fr

Keywords: microplastics; porous media; retention; transport; polyethylene; retention efficiency; numerical model; MT3DMS; MODFLOW

Abstract

This study concerns the transport and retention of polydisperse micron-sized (16 ± 6 µm) of microplastics (MPls) in porous media under varying flow rate conditions. Sorption kinetics were modeled using first-order reversible and irreversible kinetic sorption models, with sensitivity analyses providing insights into each sorption parameter's effect. Both numerical modeling and experimental measurements were employed to assess sand filter retention rates. The impact of flow rate on sorption reveals variations in distribution coefficient (K_d), mass transfer coefficient (β), and irreversible sorption rate (K_1). Lower flow rates are correlated with higher K_d and β values, indicating an increase in sorption and diminished mass transfer rates. The findings revealed that an increase in K_d resulted in a more gradual sorption process with a decrease in peak concentration, whereas changes in β influenced the rate of sorption and peak concentration to a lesser extent compared to Kd. Lower K_1 values are associated with higher peak concentrations and decreased retention efficiency. Retention rates were evaluated by a numerical model and found as 28 ± 1% at a flow rate of 31 ml min^{-1} and 17 ± 1% at 65 ml min^{-1}. The introduction of MPls into soil environments has been noted to modify transport dynamics into soil. As a result, these alterations effects hydrological characteristics of soil, thereby impacting quality of groundwater and agricultural output. The mean absolute error (MAE) of 6% between modeled and observed

retention rates suggests minor discrepancies. This study highlights the importance of examining retention efficiency and the accuracy of numerical models in porous media during MPl transport.

4.2. Introduction

Plastics are extensively used across various sectors, yet their inadequate recyclability coupled with degradation and abrasion processes leads to their fragmentation into smaller pieces and release to nature. Subsequently, these plastic fragments are disseminated into natural environments through diverse transport mechanisms, including wind, runoff, and infiltration. Consequently, these plastic particles, categorized as emerging pollutants, pervade natural ecosystems, including freshwater resources, thereby posing potential risks to living organisms and natural cycles. Solid plastic particles insoluble in water, ranging in size from 1 µm to 1,000 µm are categorized as microplastics (MPls), with dimensions ranging from 1 mm to 5 mm, and are classified as large MPls. The size classification of MPls is divided into 6 classes (Annex Table 4.S1.) (ISO 24187, 2023).

MPls have been identified in marine, terrestrial, and freshwater environments (Ivar Do Sul & Costa, 2014; Koutnik et al., 2021). They have also been found in karst groundwater systems (Panno et al., 2019), alluvial sedimentary aquifers (Samandra et al., 2022), and groundwater around landfill sites (Bharath K et al., 2021). The filtration properties of groundwater environments play a crucial role in regulating the quality of groundwater by removing or reducing the concentration of particles and contaminants as water moves through the subsurface. The filtration mechanism of porous media is orchestrated through three key steps. The first is a transport step, characterized by a physical-hydraulic process. Following this, an attachment step ensues, driven by a physical-chemical process. The final step is detachment, wherein retained particles are released as long as new particles or blank water continue to be supplied. These steps collectively define the dynamic processes governing the intricate filtration mechanism of porous media (Adin et al., 1979).

Physical mechanisms that are mainly responsible for particle transport in the filter pores are Brownian diffusion, deposition, direct interception, and hydrodynamics. Diffusion assumes a critical role, especially for particles smaller than 1 micron (Banihashem & Karrabi, 2022). The deposition mechanism, governed by gravity, is linked to the sedimentation rate of particles. This process guides particles through streamlines, ultimately directing them toward the grains of porous media, known as collectors. Gravity-induced deposition holds particular significance for particles larger than 1 micron, where the density of particles becomes pivotal. Interception occurs as particles traverse streamlines closely to the collector, resulting in attachment. The hydrodynamic process, influenced by particle rotation and movement across streamlines, is intricately tied to particle shape and its interaction with the fluid (Banihashem & Karrabi, 2022).

The adaptation of the approaches used for solute transport to colloidal solution transport is an employed practice (Simunek et al., 2006). In the literature, there are models that integrate the classical advection-dispersion equation with various types of kinetic attachment models. A

majority of these transport models presume that the attachment process adheres to either one-site kinetics, involving both forward and reverse terms (Tufenkji & Elimelech, 2004), or two-site kinetics, encompassing reversible and irreversible attachment mechanisms (Compère et al., 2001). In a kinetic model, the solute transport equation describes the rate at which the solute is adsorbed onto the solid surface and desorbed from it (Fetter et al., 2018).

In recent studies, the analysis of MPls transport into porous media has predominantly involved the utilization of Class 1 (1 μm to 5 μm) MPLs, as outlined in Table S1 (Z. Dong et al., 2018; M. Li, Zhang, Rong, et al., 2021; Zhao et al., 2021). Hou et al., (2020) focused on Class 3 (10 μm to 50 μm) MPls revealed that increased particle sizes in the porous medium, along with lower ionic strength and the presence of fulvic acid, can potentially augment the movement of MPLs (40 - 48 μm) within porous media. Conversely, smaller-sized porous media and lower velocities demonstrate superior filtration performance. The highest mass recovery of MPls was determined to be 18 %. Another study involving MPLs (200 - 500 μm) which corresponds Class 5 (100 μm to 500 μm) found that velocity is a significant parameter influencing filtration (Okutan et al., 2022). Two models, namely the attachment model and the attachment-detachment model, were formulated, and it was determined that the attachment-detachment model, incorporating a time-dependent detachment coefficient, better predicts the transport of MPls (10 μm and 20 μm) which in the range of Class 3 (10 μm to 50 μm) in porous media compared to the traditional attachment model (Qi et al., 2022). This observation underscores the importance of MPls desorption in the transport process. The calculated total mass recovery under various conditions ranged from 0.08% to 35.9% (Qi et al., 2022).

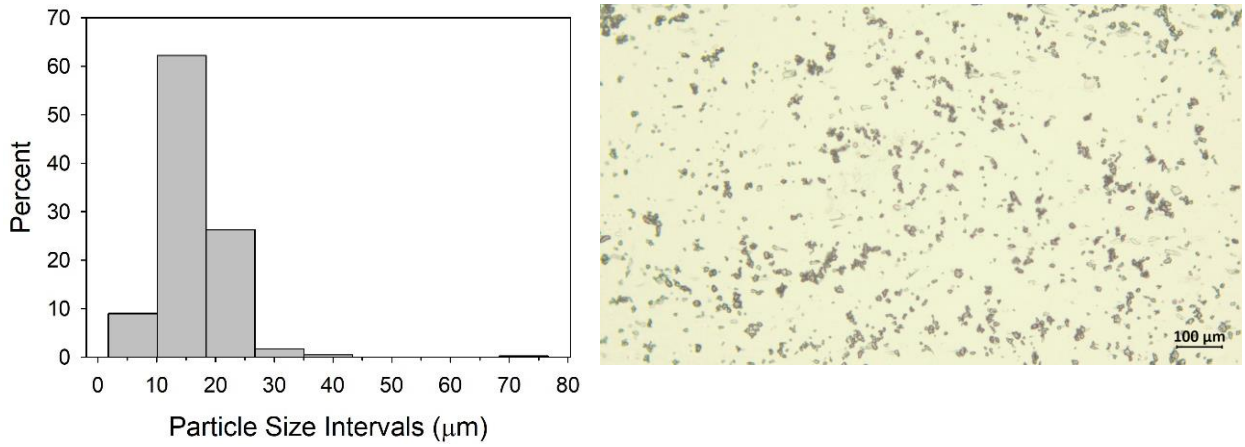
Notably, there is a lack of research concentrating on the filtration capacity of porous media for non-reference type MPls and their transport dynamics. These MPl particles, lacking the characteristics of reference material, are presumed to exhibit shapes and size distributions more akin to particles found in natural environments. This study aims to investigate the filtration capacity of porous media while transport of polyethylene-type, polydisperse, Class 3 sized MPl particles in a saturated quartz sand-type porous medium and assess its filtration efficiency using numerical models derived from flow and transport equations. This investigation encompasses the computation of sorption parameters with reversible and irreversible kinetic sorption models, the determination of retention efficiencies, and an examination of the impact of flow rate on the transport process.

4.3. Materials and Methods

4.3.1. Materials

The polyethylene (PE) type MPls are in fine powder form with a density of 0.91 g cm^{-3} were purchased from Goonvean Fibres, (United Kingdom). The PE particles are polydisperse, and their size measurements were conducted under optical microscopy, with an average particle size of 16

± 6 µm (Figure 4.1.a and Table 4.1.). The shape of MPls can be described as fragmental (Figure 4.1.b). A commercially available dish detergent containing anionic surfactant was employed to generate a uniform suspension of MPls. Injection concentrations were prepared with MPls and surfactant at a ratio of 1:1, with a concentration of 2 g/L. Prior to reaching the 1:1 ratio, lower ratios were attempted, but successful dispersion could not be achieved. Additionally, the 1:1 ratio was favored in the literature (Y. Jiang et al., 2021).



(**a**) (**b**)

Figure 4.1. The histogram of the size distribution (a) and the optical microscopy image (b) of MPls.

Table 4.1. The statistical properties of MPls size distribution (All the values are given in µm).

Size of Population	Max	Min	Median	Mean	Standard Deviation	Quantile 1	Quantile 3
400	77	2	16	16	6	13	19

A stock concentration of 25 g L^{-1} of rhodamine WT (Cole-Parmer) fluorescent dye was utilized in tracer experiments to assess the hydrodynamic characteristics of porous media. The primary concentration was diluted to 400 µg L^{-1} to perform dye tracer experiments right before starting the experiment to avoid the direct influence of sunlight.

Quartz sand was kindly provided by Esan Eczacıbaşı Industrial Raw Materials Co. (Türkiye) with a density of 2.60 g ml^{-1} and bulk density of 1.33 g ml^{-1}. The determination of particle size was accomplished via sieve analysis, resulting in a D_{50} value of 2.9 mm. A notable proportion, specifically 83%, of the sand exhibited retention on a 2 mm mesh-sized sieve (Figure 4.2.). The hydraulic conductivity of the sand was determined with a constant head permeameter and found to be 11.0 ± 0.3 cm min^{-1}. The effective porosity (θ) was calculated as 0.49 ± 0.009 with fluorescent dye tracer experiments and numerical modeling.



Figure 4.2. The grain size distribution curve of sand.

4.3.2. Methods

Transport experiments and constant head permeameter experiments were conducted in an acrylic column with 100 cm height and 7 cm inner diameter. The column has been packed with washed and dried sand at 105 ° C overnight. During the packaging process, water was pumped from bottom to top, and the column was gently tapped to prevent possible air bubbles.

The experiments adhered to a sequence commencing with constant-head permeameter tests to ascertain hydraulic conductivity. Subsequently, dye tracer experiments were conducted to evaluate the hydrodynamic properties of the porous media, and the sequence concluded with MPls tracer experiments aimed at determining sorption parameters and retention efficiencies of the porous media. This order was consistently followed for each column packing, and after completing the series of experiments, the porous media were changed for a new set of tests. In total, four sets of experiments were carried out.

4.3.2.1. Permeameter Experiments

Following the column filling process, preceding each dye tracer test, constant head permeameter experiments were conducted. The hydraulic conductivity of the packed sand was determined with Dacy's Law (Batu, 2005).

$$K = -\frac{Q}{A(dh/ds)} \tag{4.1}$$

K is the hydraulic conductivity (L/T), Q is discharge (L^3/T), A is the cross-sectional area of the column (L^2) and dh/ds is the hydraulic gradient. The hydraulic gradient was altered three times, and the average values resulting were employed in the numerical models.

4.3.2.2. Transport Experiments

Subsequently, the column underwent a thorough flushing with distilled water, reaching a state of saturation characterized by effluent exhibiting negligible turbidity measurements. The operational pH and electrical conductivity values were measured following each MPls transport experiment, with mean values determined as 7 ± 0.2 for pH and 57 ± 5 µS cm^{-1} for electrical conductivity.

The volume of one pore volume in each sand-packed column varies slightly depending on the sand height and porosity. Specifically, the average one pore volume of the sand-packed column is calculated to be 1664 ± 31 ml. The amount equivalent to 1.8 pore volume of fluorescent dye tracer was continuously injected, followed using at least 2 pore volumes for the 65 ± 0.3 ml min^{-1} flow rate, and 5 pore volumes for the 31 ± 0.4 ml min^{-1} flow rate of distilled water to flush the column. This injection procedure was followed for continuous injection of MPls. The flushing process was conducted at a constant flow rate generated by a peristaltic pump 65 ± 0.5 ml min^{-1} and 31 ± 0.2 ml min^{-1} flow rates. Relative to the flow rate employed, samples of 4 ml each were collected every two minutes, commencing from the 8^{th} minute post-injection for a flow rate of 65 ml min^{-1}, and every three minutes, beginning from the 27^{th} minute post-injection for a flow rate of 31 ml min^{-1}. Each flow rate condition was replicated.

The flow rates of 31 ml min^{-1} and 65 ml min^{-1} correspond to linear velocities (v) of 0.4 cm min^{-1} and 0.8 cm min^{-1}, respectively. Groundwater moves from higher elevations to lower elevations and from locations of higher pressure to locations of lower pressure. Typically, this movement is quite slow, ranging from less than 0.3 meters per day to a few tens of meters per day. For karst aquifers, which are not considered porous medium, it could be faster (Maurice et al., 2023). Typical groundwater velocity in a sandy or gravelly aquifer may range from approximately 0.01 to 1 cm per minute (Harter, 2003).

There is nearly a twofold difference between the two flow rates, which allows for the distinction of their effects on the experiment. When the flow rate is too fast, advective transport becomes dominant, overshadowing the dispersion and sorption effects. Therefore, a maximum flow rate of 65 ml min^{-1} was chosen. For the selection of the lowest flow rate, the reliability of operational conditions was considered, particularly focusing on the duration of the experiment, which was set to six hours for a flow rate of 31 ml min^{-1}. These selected flow rates align with the general conditions of groundwater flow.

The Aquaflour® Handheld dual-channel fluorometer and turbidity device were utilized for concentration determination. For fluorescent dye tracer experiments, the concentration measurements were calibrated using known concentrations of dye solutions in the green channel. Following the calibration of the fluorometer at a concentration of 400 µg/L rhodamine WT for effluent measurements, dilutions of rhodamine WT were prepared for each experiment by deriving calibration curves from the injection solution. (Annex Figure 4.S1.) For MPl tracer experiments, the turbidity channel was employed. The device was initially calibrated using a 1000 NTU calibration standard, followed by the creation of a calibration curve using MPls and surfactant-

containing suspension of different concentrations to convert NTU to concentration values (Annex Figure 4.S2.). The injection concentration is selected 2 g/L which is approximately equal to the 1000 NTU to reduce the measurement errors due to impurities caused by sand or water at the low concentrations in the experiment.

In simulation computations, MT3DMS where MT3D stands for the Modular 3-dimensional Transport model, and MS denotes the multi-species structure for accommodating add-on reaction packages is commonly employed alongside MODFLOW which is a block-centered finite-difference flow model. Following the development and calibration of a flow model, the required data for the transport model was retrieved accordingly. (Shu et al., 2023; Zheng & Wang, 1999). The transport of fluorescent dye was simulated using advection-dispersion equations corporation first-order reversible kinetic (non-equilibrium) sorption, while the transport of MPls was modeled with advection-dispersion equations incorporating first-order reversible kinetic (non-equilibrium) sorption and first-order irreversible sorption terms. The numerical models from the observed values were created with Groundwater Vistas Version 7 (student license) which provides user interfaces for MODFLOW and MT3D modules of USGS (Zheng & Wang, 1999). The MT3D module is applied for modeling advection, dispersion, and chemical reactions within groundwater systems.

The partial differential equation governing the fate and transport of contaminants in one-dimensional, transient groundwater flow systems can be expressed as follows (Zheng & Wang, 1999) :

$$\frac{\partial(\theta C)}{\partial t} = \frac{\partial}{\partial x}\left(\theta D \frac{\partial C}{\partial x}\right) - \frac{\partial}{\partial x}(\theta v C) + q C_s + \Sigma R_n \tag{4.2}$$

where θ is porosity (-), C is concentration (ML^{-3}), t is time (T), x is distance (L), D is hydrodynamic dispersion coefficient (L^2T^{-1}), v is linear pore water velocity (LT^{-1}), q is volumetric flow rate per unit volume of aquifer representing fluid sources (positive) and sinks (negative) (T^{-1}), C_s is concentration of the source or sink flux (ML^{-3}), and ΣRn is chemical reaction term ($ML^{-3}T^{-1}$).

In instances where the local equilibrium cannot be attained, it is posited that the sorption process may be effectively delineated through a reversible kinetic reaction of the first order as follows (Zheng & Wang, 1999):

$$\rho_b \frac{\partial C'}{\partial t} = \beta(C - \frac{C'}{K_d}) \tag{4.3}$$

Where ρ_b is bulk density (M/L^3), β is the first-order mass transfer rate between the dissolved (C) and sorbed (C') phases (T^{-1}), and K_d is the distribution coefficient (L^3M^{-1}).

The bulk density ρ_b is calculated from the density ρ of sand grains (M/L^3) which is calculated with a pycnometer. Then the bulk density is calculated as follows (Batu, 2005):

$$\rho_b = (1 - \theta)\rho \tag{4.4}$$

In some situations, once the solute is sorbed on the solid phase, it cannot be desorbed. The reaction is irreversible and leads to a mass loss of the dissolved phase. This process can be described through the first-order irreversible kinetic sorption model, with the following equation (Fetter, 1999):

$$\frac{\partial C'}{\partial t} = K_1 C \tag{4.5}$$

where K_1 (T^{-1}) is the first order irreversible kinetic sorption rate constant.

The first-order irreversible kinetic sorption model was used by Lee et al., (2021) to analyze the migration of toluene contaminant plume in 3D flow conditions. This last kinetic model was also applied to simulate radioactive decay or biodegradation (Matthies et al., 2008). In such cases, the constant rate (K_1) is related to the half-life ($t_{1/2}$) of the materials as follows:

$$K_1 = \frac{\ln 2}{t_{1/2}} \tag{4.6}$$

where $t_{1/2}$ is conventionally denoting half-life (T^{-1}), was employed to signify the retained mass rather than its conventional application to represent the temporal duration associated with the decay of a substance by half.

Rhodamine WT might not behave entirely as a conservative tracer, especially when applied to the used quartz sand (Runkel, 2015; Sabatini & Austin, 1991). Consequently, a numerical solution incorporating sorption was chosen as a better fit, enhancing the alignment of calculated BTCs with observed BTCs. Through fluorescent dye experiments, kinematic porosity (θ), dispersivity (α), distribution coefficient for the sorbed phase (K_d), and the first-order mass transfer rate (β) values that characterize properties of porous media were estimated. The obtained θ and α values were subsequently utilized as inputs for analyzing MPl experiments. In the MPl experiments, the parameters under investigation include the distribution K_d, β, and K_1. The identification of optimal values necessitates the utilization of a trial-and-error approach. The parameters K_d, β, and K_1 were adjusted iteratively to align the curve with the calculated values to the curve with observed values. Following each parameter adjustment, the residual sum of squares (RSS) error was scrutinized.

4.3.2.3. Retention Efficiencies

The quantity of MPls transported through the porous media was assessed through numerical model mass calculations and by measuring the mass of particles at the conclusion of experiments. The numerical model evaluation involves accounting for mass released from storage as a result of a decrease in sorbed concentration and mass accumulation in storage due to an increase in sorbed concentration, incorporating considerations for first-order irreversible reactions.

Experimental measurements were conducted by collecting the transported effluent with a known volume at the conclusion of experiments. The concentration of accumulated particles was determined using a turbidimeter and then converted to concentration units. By utilizing the known

volume, the transported mass was calculated. Subsequently, the initially transported quantity was subtracted from the total injected amount, thereby yielding insights into the retention rates of MPls in porous media.

The Mean Absolute Error (MAE) was calculated by comparing the retention values obtained numerically with those measured experimentally, aiming to evaluate the precision of the numerical model. MAE provides a direct measure of the average absolute deviation between predicted and actual values. It is frequently employed in scenarios where all errors carry equal significance, rendering it more resilient to the influence of outliers compared to other metrics such as RMSE. Additionally, MAE shares the same unit of measurement as the original data, further enhancing its interpretability.

4.3.2.4. Sensitivity Analyses

The sensitivity of the model was applied by systematically altering the input of one parameter at a time, including Q, K_d, β and K_1, to evaluate their effects on the filtration of MPls. In the sensitivity analyses, each variable was individually modified based on the predicted values of the MPl A and MPl B experiments. The influence of sorption on MPls' transport was assessed based on both the MPl particle transport experiment and the dye (solute) experiment. The dye experiment serves as a reference transport breakthrough curve (BTC). The impact of retention efficiencies was assessed to comprehend the influence of Q and K_1 parameters on retention.

4.4. Results and Discussions

4.4.1. Permeameter Experiments

In this study, a constant head permeameter and a dye experiment were conducted under consistent conditions for each MPls experiment. This allowed for the observation of the transport behavior of MPls in comparison to the solute. Hydraulic conductivity values were determined with Equation 1 and shown in Table 4.2. for each packed sand column by conducting constant-head permeameter tests to be used in the numerical model. Minor disparities in hydraulic conductivity values are evident, likely attributed to the utilization of freshly packed sand for each experiment. Variations in the arrangement of sand grains, discrepancies in grain sizes, and the presence of angular shapes could account for these observed differences.

Table 4.2. Hydraulic conductivity (K) values corresponding to each experimental series. (For the A series, tracer experiments were conducted at a flow rate of 31 ml min^{-1}, while for the B series, tracer experiments were conducted at a flow rate of 65 ml min^{-1}.)

Experiment Name	K (cm min^{-1})
A	11.3 ± 0.4
A.1	10.7 ± 0.1
B	10.9 ± 0.1
B.1	11.3 ± 0.3

4.4.1.1. Transport Experiments

Breakthrough curves (BTCs) are depicted by a normalized concentration, defined as the outlet concentration (C) divided by the constant inlet concentration (C_0), as a function of pore volume, which represents the volume of voids within the packed porous media. The pore volume is computed by multiplying the volume of the packed column (or the volume can be calculated for each sample while multiplying sampling time with flow rate) by the porosity of the porous media.

The observed and computed BTCs were shown for 31 ml min^{-1} and 65 ml min^{-1} in Figure 4.3. a and b, respectively. The values for α, θ, β, and K_d were obtained through modeling and adjusting the computed results to align with the observed outcomes of the dye tracer experiments, are presented in Table 4.3. Upon analysis of the average values, the dispersivity was determined to be consistent at 0.1 across all experiments, while the porosity value was calculated as 0.49 ± 0.009. Regarding sorption parameters, the K_d values were observed to be 0.08 ml g^{-1} for a flow rate of 31 ml min^{-1} and 0.125 ± 0.075 ml g^{-1} for a flow rate of 60 ml min^{-1}. Additionally, for β values, a slight increase was noted with increasing flow rate, with values measured at 0.0009 ± 0.0001 min^{-1} for a flow rate of 30 ml min^{-1} and 0.0025 min^{-1} for a flow rate of 65 ml min^{-1}.

Subsequently, α and θ were employed as constant input parameters for modeling the corresponding MPls experiments. Dye concentrations swiftly reach a relative concentration close to unity after the arrival of the solute. This concentration level was maintained until the conclusion of the solute concentration. When assessing the study conducted with MPls, there is an observable gradual increase in particle concentration. This gradual increase is more prominent at 31 ml min^{-1} flow rate (Figure 4.3.)

Table 4.3. The dye experiment results for porosity (θ), dispersivity (α), distribution coefficient (K_d), and mass transfer rate (β) values.

Experiment Name	Q (ml min^{1})	θ (%)	α (cm)	K_d (cm^3g^{-1})	β (min^{-1})
DYE A	31	0.49	0.1	0.08	0.0008
DYE A.1	30	0.49	0.1	0.08	0.0010
DYE B	65	0.49	0.1	0.20	0.0025
DYE B.1	64	0.47	0.1	0.05	0.0025

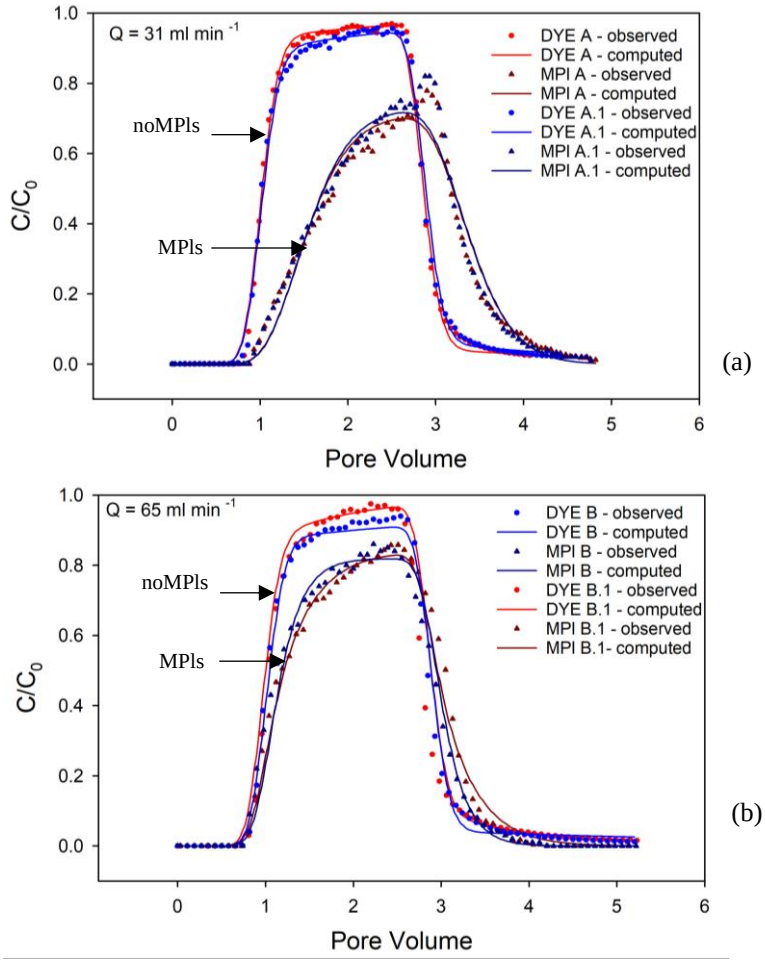


Figure 4.3. The breakthrough curves observed and computed data for low (a) and high (b) flow rates. In each plot, the y-axis is denoted as C/C_0, while the x-axis corresponds to pore volume.

The sorption which is expected between MPl particles and sand grains causes the suspension to appear later than expected at the column outlet. If the displacing of solute is held back within the column due to some chemical or physical process, the BTC will shift to the right (Nielsen & Biggar, 1962). The BTCs for MPls at 31 ml min^{-1} exhibit a shape more indicative of transport involving sorption reactions compared to the BTCs for 65 ml min^{-1} (Figure 4.3.). Upon examining studies conducted at the relatively high flow rate, it is observed that the transport of MPls forms a curve closer to the reference transport of dye.

Sorption is characterized through the values of K_d, β and K_1, as presented in Table 4.4. At the lower flow rate, the average K_d was computed as 0.2 ml g^{-1}, whereas at the higher flow rate, the average Kd was determined to be 0.07 ± 0.02 ml g^{-1}. A reduction in flow rate corresponded to an increase in the K_d value. The β values were observed to be 0.05 min^{-1} for the lower flow rate and 0.02 min^{-1} for the higher flow rate. The bulk density of sand was determined to be 1.33 g ml^{-1}, and this value was utilized by the model for the calculation of β values. Increased flow rates were associated with a decrease in β values, indicative of altered mass transfer rates. The irreversible sorption of MPls

into the column was referred to as K_1. The calculated K_1 value was 0.006 ± 0.0003 min^{-1} for the experiments conducted at a relatively slow flow rate of 31 ml min^{-1}. The calculated K_1 value was 0.007 ± 0.0004 min^{-1} for the experiments at a relatively fast flow rate of 65 ml min-1. The increase in the flow rate was followed by an increase in K_1 values. (Table 4.4.).

Table 4.4. The computed parameters for distribution coefficient (K_d), , and mass transfer rate (β) , and irreversible kinetic sorption rate (K_1) were determined for each flow rate, with the $C/C_{0\ peak}$ representing the ratio of MPls concentration at the peak point.

Experiment Name	Q (ml min^{-1})	K_d (ml g^{-1})	β (min^{-1})	K_1 (min^{-1})	$C/C_{0\ peak}$
MPl A	31	0.2	0.05	0.006	0.78
MPl A.1	31	0.2	0.05	0.006	0.82
MPl B	65	0.05	0.02	0.008	0.86
MPl B.1	64	0.09	0.02	0.007	0.86

4.4.1.2. Retention Efficiencies

The retained mass within the porous media was determined through both numerical simulations (R_1) and experimental measurements (R_2). Analyzing the percentage of retained mass enabled the assessment of the retention efficiency of MPls within the utilized porous media, particularly in response to variations in flow rate. For a flow rate of 31 ml min^{-1}, the average retention rates are measured at 28 ± 1% for R_1 and 24 ± 2% for R_2, respectively. For a flow rate of 65 ml min^{-1}, the average retention rates are measured at 17 ± 1% for R_1 and 9 ± 4% for R_2, respectively. For a flow rate of 65 ml min^{-1}, the average retention rates are determined to be 17 ± 1% for R_1 and 9 ± 4% for R_2, respectively (Table 4.5.). An observed trend indicates a decrease in retention efficiency with an increase in flow rate. The standard deviation of R_2 is notably higher for the flow rate of 65 ml min^{-1} may be attributed to non-homogenized effluent suspension. This could be explained by the higher flow rate leading to increased flow heterogeneity.

Table 4.5. The numerically calculated retention rates for each experiment, varying according to the flow rate, are shown as R_1, while the experimentally measured retention rates are indicated as R_2.

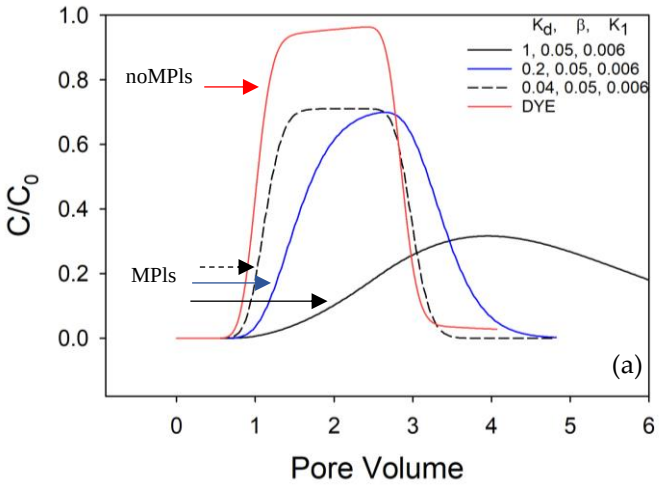
	Q (ml min^{-1})	R_1 (%)	R_2 (%)
MPl A	31	29	26
MPl A.1	31	27	22
MPl B	65	18	13
MPl B.1	64	16	5

The Mean Absolute Error (MAE) is calculated as 6%, indicating that, on average, the model's predicted retention rates (R_1) differ by 6% from the experimentally measured retention rates (R_2). This can give information on the accuracy of the numerical model simulation based on experimentally measured retention rates. It is important to acknowledge that sampling homogeneously from MPl effluent reservoirs is challenging, which may contribute to slight measurement errors that need to be accounted for while considering model accuracy.

4.4.1.3. Sensitivity Analyses

The impact sorption parameters can be uncovered through sensitivity analysis. The sensitivity analyses were conducted for 31 ml min^{-1} and 65 ml min^{-1} flow rate (Figure 4.4. and Annex Figure 4.S3.)

The variations in the K_d value have been modeled while keeping β fixed at 0.05 min^{-1} and K_1 fixed at 0.006 min^{-1}. In the context of nonequilibrium transport, the phenomena of sorption are contingent on time and occur gradually (Skaggs & Leij, 2002). The increase in K_d has led to a more gradual sorption over an extended period and increased retardation. When K_d and K_1 are held constant at values of 0.2 ml g^{-1} and 0.006 min^{-1}, respectively, and the impact of β variation is examined, a decrease tends to approximate solute transport and leads to a reduction in peak concentration. Conversely, as the β values increase, the sorption process occurs more gradually (Figure 4.4b.). Finally, to examine the impact of K_1, the K_d, and β values were held constant at 0.17 ml g^{-1} and 0.06 min^{-1}, respectively. The effect of K_1 is proportional to the retained mass, with a decrease leading to an increase in the concentration peak value, and an increase resulting in a decrease. (Figure 4.4c.). Since it is irreversible kinetic sorption rate, K_1 directly influences the retained mass, with a decrease in K_1 resulting in a decrease in retention efficiency (Table 4.6.)



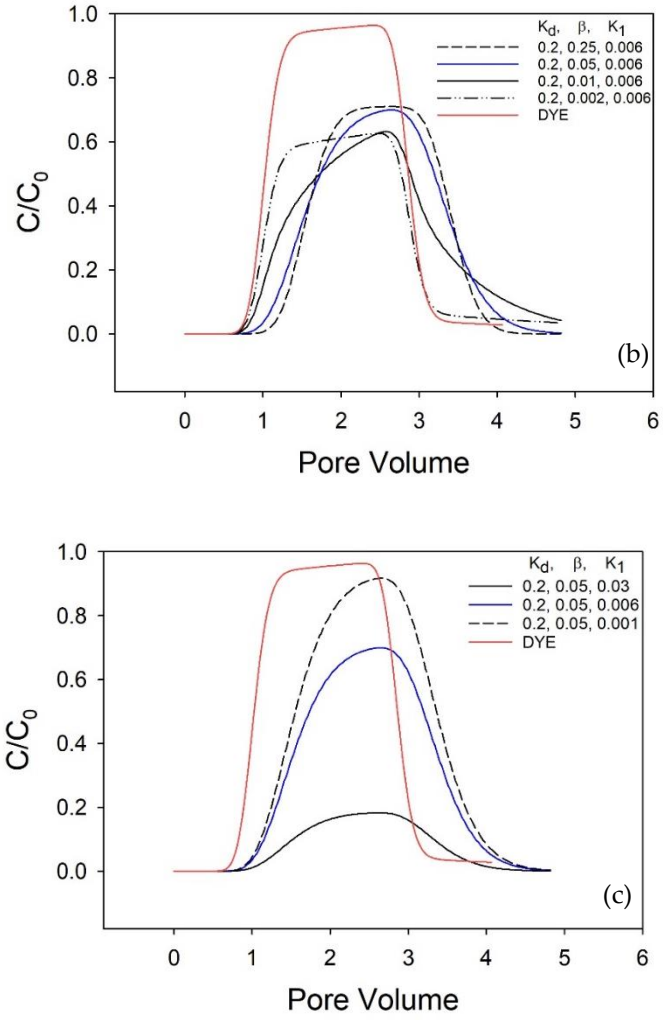


Figure 4.4. The BTCs of the sensitivity simulations for the distribution coefficient, K_d (a), mass transfer rate, β (b), and kinetic sorption rate, K_1 (c), were analyzed. The computed BTCs of the MPl A and DYE A experiments are represented by a blue line and a red line, respectively. In the legend, the parameters are listed in the order of K_d, β, and K_1. (This sensitivity analyses corresponds to MPl A experiments where 1 pore volume is equal to 1688 ml)

Table 4.6.The retention efficiency values calculated numerical solution due to change in irreversible kinetic sorption rate (K_1).

Q (ml min^{-1})	K_d (ml g^{-1})	β (min^{-1})	K_1 (min^{-1})	Retention Efficiency (%)
31	0.2	0.05	0.006	29
31	0.2	0.05	0.03	81
31	0.2	0.05	0.001	7
65	0.25	0.02	0.01	18
65	0.05	0.02	0.04	63
65	0.05	0.02	0.002	4

Upon evaluating the sensitivity of flow rates while keeping the sorption parameters (K_d, β, and K_1) constant, the impact of flow rate changes on retention efficiencies was examined (Table 4.7.)

As the flow rate decreases, there is an increase in the retention of MPls within porous media. This is attributed to the higher velocity associated with increased flow rates, leading to a stronger advection process. Consequently, when flow rates are higher, advection predominates over retention, resulting in lower retention rates. (Annex Figure 4.S4.).

Table 4.7. The retention efficiency values calculated numerical solution due to change in flow rates, Q, with constant sorption parameters which are distribution coefficient (K_d), mass transfer rate (β), and irreversible kinetic sorption rate (K_1). The sorption parameters of experiment MPl A, conducted at a flow rate of 31 ml min^{-1}, remained constant.

K_d (cm^3/g)	β (min^{-1})	K_1 (min^{-1})	Q (ml min^{-1})	Retention Efficiency (%)
0.2	0.05	0.006	155	7
0.2	0.05	0.006	65	15
0.2	0.05	0.006	31	29
0.2	0.05	0.006	6	82

4.5. Conclusion

The study aimed to fill the knowledge gap regarding the transport of 16 ± 6 µm, polydisperse MPls in porous media under different flow rate conditions. The hydrophobic nature of polyethylene poses challenges for dispersing MPls in water. Surfactants proved instrumental in facilitating their dispersion in distilled water. Additionally, surfactants commonly found in natural environments are frequently employed in cleaning products.

Sorption kinetics were modeled with first-order reversible kinetic (non-equilibrium) sorption and first-order irreversible kinetic sorption models. The sensitivity analyses provided information about the effect of each sorption parameter. The retention rates of the sand filter were revealed in both numerical modeling and experimental measurements. The accuracy of the model was calculated with the error between modeled and observed retention efficiencies.

The study explored the impact of flow rate on sorption, examining the distribution coefficient (K_d), mass transfer coefficient (β), and irreversible sorption rate (K_1). The BTCs for dye tracer experiments showed consistent behavior, while those for MPls exhibited gradual increases in particle concentration, particularly at lower flow rates, indicating sorption effects. Sorption parameters varied with flow rate, with lower flow rates associated with higher K_d and β values, suggesting increased sorption and altered mass transfer rates.

Increasing K_d led to more gradual sorption and increased retardation, while variations in β affected the pace of sorption and peak concentration. Changes in K_1 influenced retained mass with lower K_1 values associated with higher concentration peak values and decreased retention efficiency

when the flow rate is constant. Another significant parameter affecting the retained mass in porous media is the flow rate. When keeping the sorption parameters constant, an increase in flow rate led to a decrease in retention efficiencies. That indicates advection becomes preponderant compared to retention.

Retention rates were assessed at different flow rates with numerical model (R_1) and experimental measurement (R_2). For a flow rate of 31 ml min^{-1}, the average retention rates are 28 ± 1% for R_1 and 24 ± 2% for R_2, respectively. At a flow rate of 65 ml min^{-1}, the average retention rates are 17 ± 1% for R1 and 9 ± 4% for R_2. Similarly, for a flow rate of 65 ml min^{-1}, the average retention rates are found to be 17 ± 1% for R_1 and 9 ± 4% for R_2. The mean absolute error (MAE) of 6% was found and that indicates the model's predicted retention rates differed slightly from experimental measurements.

The current study focuses on examining the retention efficiency of porous media during the transport of MPls with the presence of surfactant into saturated porous media. The utilization velocities (Okutan et al., 2022), properties of porous media(Hou et al., 2020), size of particles, water chemistry (S. Dong et al., 2021; Z. Dong et al., 2018) and co-existence with natural (M. Li, Zhang, Yi, et al., 2021) or pollutant components (Ling et al., 2021) need to be considered for an efficient filtration process. In this study the flow rate and co-presence of MPls with surfactant were assessed. It is important to note that the quantities of surfactant and injected MPls do not precisely mirror natural conditions. Nonetheless, the study addresses existing gaps in understanding non-reference MPls, prompting further exploration into filtration efficiency and transport dynamics by integrating solute transport principles with kinetic attachment models.

Filters constructed using sand, as demonstrated in this study, provide insights into the effectiveness of sand filtration processes in drinking water treatment plants and the contamination of subsurface groundwater environments, both of which are vital sources of freshwater. Sand filtration is a common and conventional phase in drinking water treatment plants, and it is crucial to evaluate its efficiency in removing microplastics (MPls), which can be observed at all treatment stages (Negrete Velasco et al., 2022). Soil-groundwater interactions are the primary pathway for the migration of MPls into groundwater. These particles have various toxic effects on terrestrial ecological systems, including microorganisms, plants, and animals, impacting their growth and reproduction (Shi et al., 2024). Additionally, humans may ingest microplastics in groundwater directly through drinking water or indirectly via the food chain, posing significant health risks (Wei & Chen, 2023). For future perspective, the studies could consider modifying water properties to better emulate natural systems, such as introducing organic materials and various types of salt ions and reducing the concentration of injected MPls. These conditions can contribute to an improved understanding of freshwater source protection and aid in the development of strategies to safeguard these vital resources.

Annex 4.A. Supplementary Information

Table 4.S1. Particle size classification of MPls (adapted from (ISO 24187, 2023))

Classification	Microplastics						Large Microplastics
	Class 1	Class 2	Class 3	Class 4	Class 5	Class 6	
Particle size (μm)	1 to < 5	5 to < 10	10 to < 50	50 to < 100	100 to < 500	500 to < 1000	1000 to < 5000

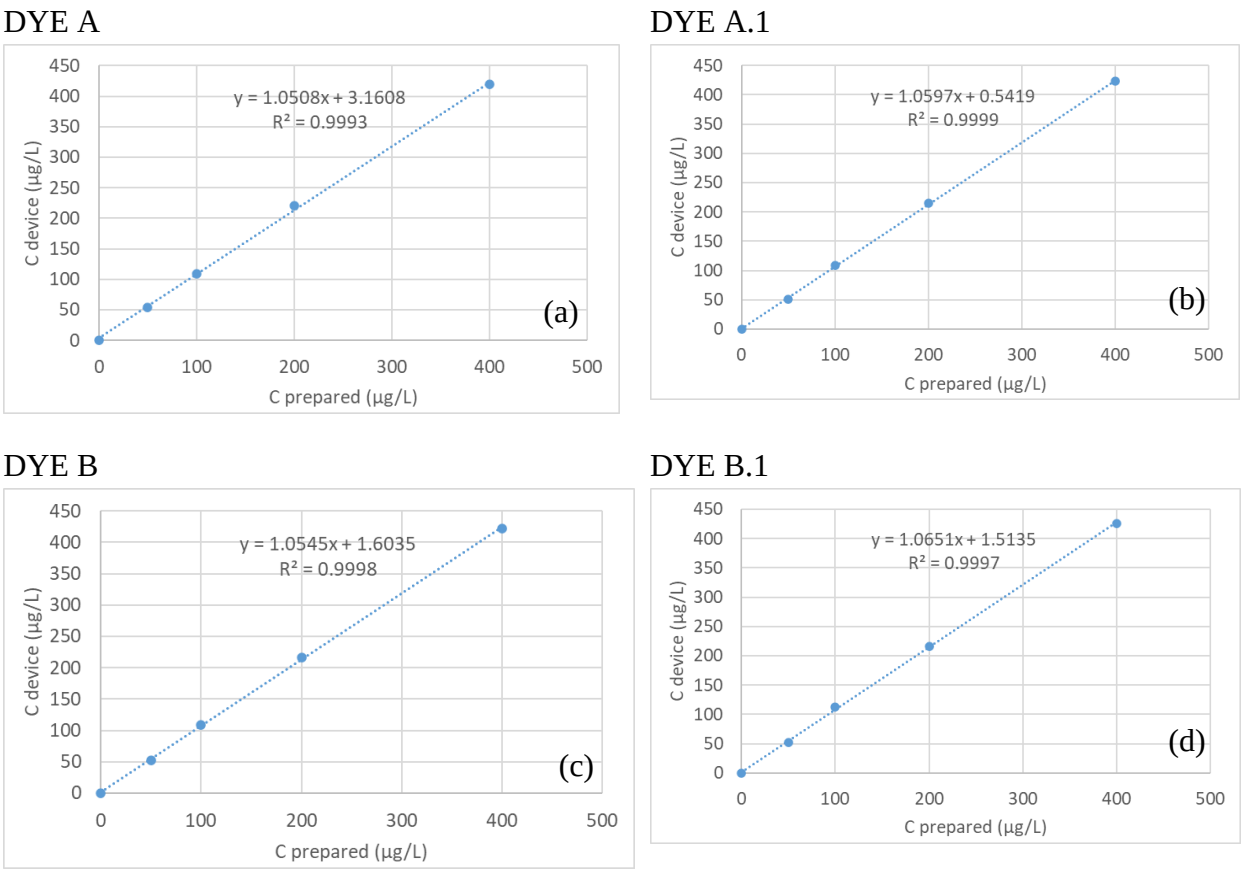
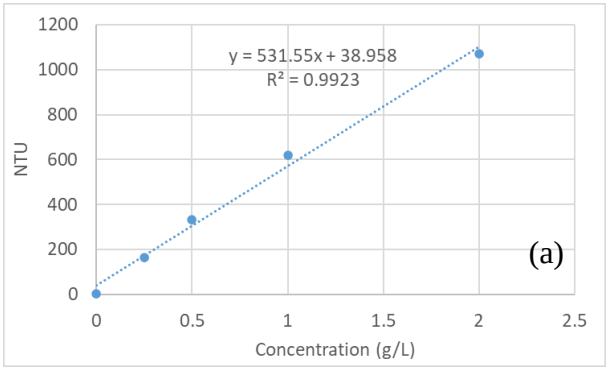
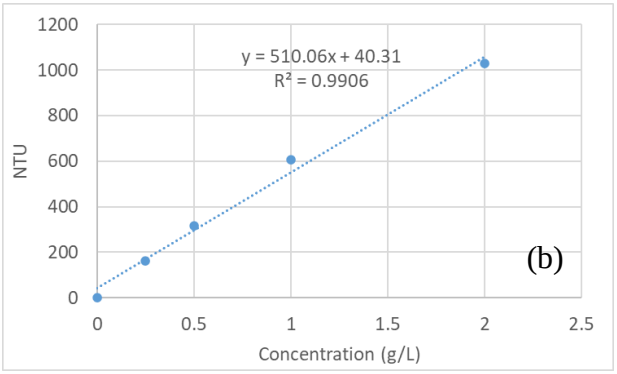


Figure 4.S1. The calibration curves for dye experiments which were used for plotting BTCs. (a) is for DYE A, (b) is for DYE A.1, (c) is for DYE B and (d) is for DYE B.1 experiments

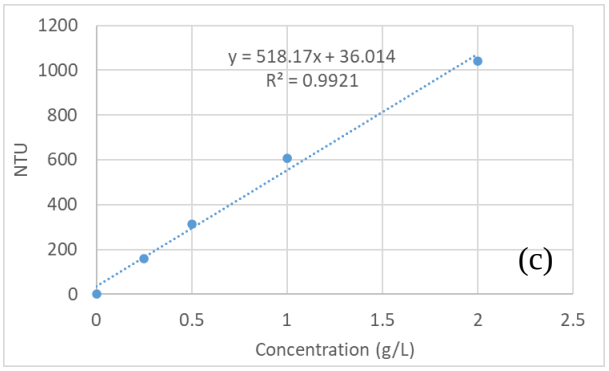
MPl A



MPl A.1



MPl B



MPl B.1

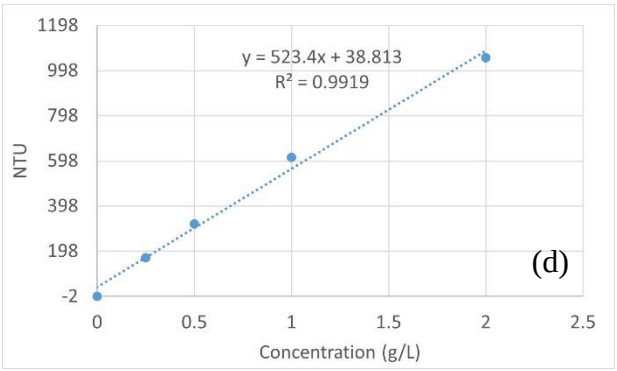
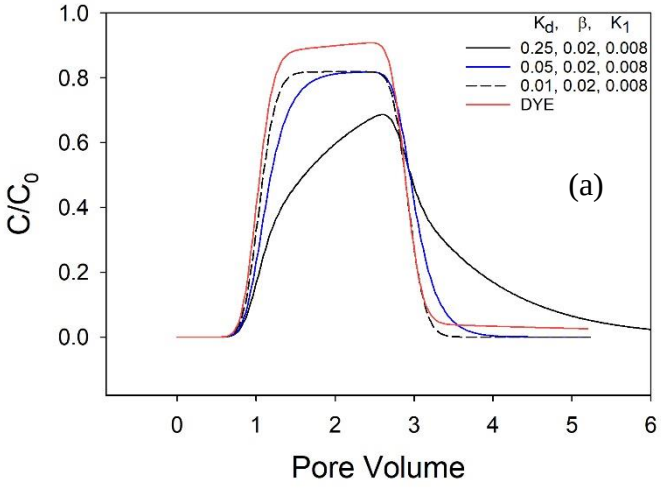


Figure 4.S2. The calibration curves for MPl experiments which were used plotting curves. NTU is the unit of turbidity. (a) is for MPl A, (b) is for MPl A.1, (c) is for MPl B and (d) is for MPl B.1 experiments



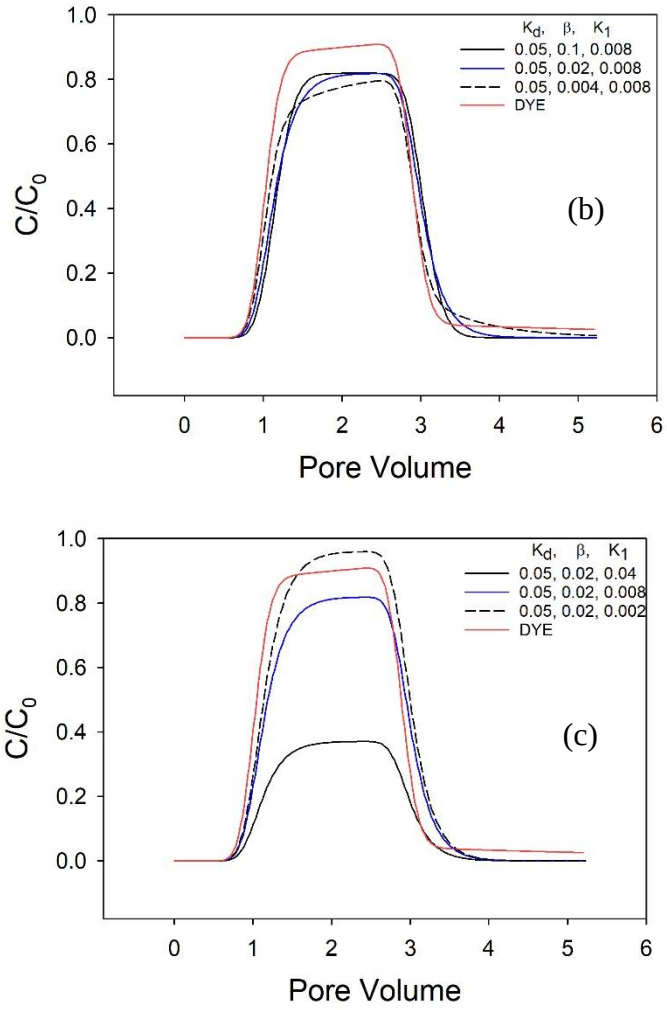


Figure 4.S3. The BTCs of the sensitivity simulations for the distribution coefficient, K_d (a), mass transfer rate, β (b), and kinetic sorption rate, K_1 (c), were analyzed. The computed BTCs of the MPl B and DYE B experiments are represented by a blue line and a red line, respectively. In the legend, the parameters are listed in the order of K_d, β, and K_1. (This sensitivity analyses corresponds to MPl B experiments where 1 pore volume is equal to 1678 ml)

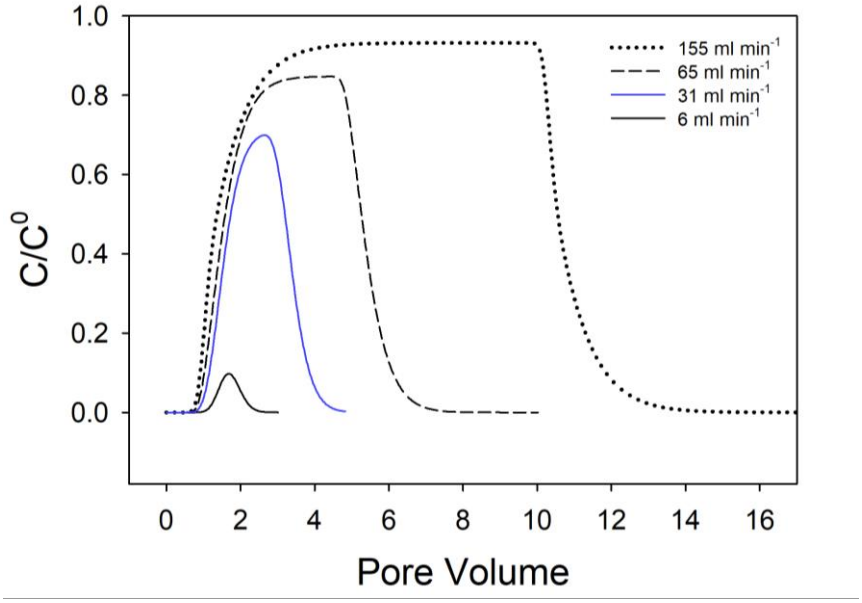


Figure 4.S4. The BTCs of the sensitivity simulations for the flow rates were analyzed. The computed BTCs of the MPl B experiment are represented by a blue line. In the legend, the parameters are listed in the order of Kd, β, and K1. (This sensitivity analyses correspond to MPl A experiments where 1 pore volume is equal to 1688 ml).

CHAPTER 5 - RETENTION AND TRANSPORT OF NANOPLASTICS WITH DIFFERENT SURFACE FUNCTIONALITIES IN A SAND FILTRATION SYSTEM[3]

5.1. Summary

Nanoplastics (NPls) pose significant challenges in environmental samples, particularly in water treatment plants (DWTPs), where ensuring their removal is crucial to safeguard drinking water quality. However, detecting and differentiating NPls from other pollutants in natural samples remains problematic due to their small size (less than 1 µm) and lack of standardized detection methods. Among the various treatment processes in DWTPs, sand filtration plays a pivotal role in removing both dissolved and particle-based contaminants. Despite its effectiveness, studies have shown that sand filtration may not eliminate NPls smaller than 1 µm, highlighting the need for a deeper understanding of their retention and transport mechanisms. To address this gap, laboratory-based sand filtration experiments were conducted with operational conditions similar to DWTPs in Geneva, Switzerland. Polystyrene NPls with positive amidine functional groups ([A-PS]+) and sulfate polystyrene NPls with negative sulfate functional groups ([S-PS]−) were employed. The impact of surface functionality, variation of NPls concentration, as well as the presence of surfactants in the coating of [A-PS]+ and solution forms, on NPls' adsorption and desorption in porous media was investigated.

Experimental results revealed that surface charges of NPls, influenced by various surface functionalities or coatings with surfactant molecules, significantly affected their retention behavior within porous media. Electrostatic interaction forces played a major role, with NPls exhibiting distinct retention efficiencies based on their surface charges. The retention efficiencies of NPls were ranked as functionalized with amidine [A-PS]+ > with sulfate [S-PS]− > with surfactant-coated amidine [SDS-A-PS]−. Charge heterogeneities caused negatively charged particles to attach to the corners of clay minerals, while positively charged particles were attached to quartz minerals. Moreover, the ζ potential measurements indicated a notable increase in positively charged particle retention with rising concentrations, while the effect on negatively charged particles was less pronounced. With the injection of surfactant into the sand filter containing adsorbed [A-PS]+ NPls, a charge inversion occurred, causing the positively charged particles present in the media to

[3] This chapter was published as *"Okutan, H.; Hul, G.; Stoll, S.; Le Coustumer, P. Retention and Transport of Nanoplastics with Different Surface Functionalities in a Sand Filtration System. Nanomaterials 2024, 14, 32. https://doi.org/10.3390/nano14010032"*

undergo transport in a negatively charged state and led to NPls' remobilization, highlighting potential transport into subsequent treatment phases.

Fractal dimension analysis from Transmission Electron Microscopy (TEM) imaging provided insights into aggregation properties, with smaller aggregate sizes associated with decreased retention efficiencies. Aggregate characteristics were found to correlate with retention efficiencies. [A-PS]+ NPls formed more compact aggregates, leading to higher retention efficiencies.

The experiments were conducted in the laboratories at the University of Geneva, Switzerland. Only the TEM imaging was performed at Bordeaux Imaging Center, France.

The findings underscored the importance of sand filtration in DWTPs, serving as a protective barrier against suspended particles and contributing to cost-effective and environmentally friendly water treatment practices. Understanding NPls' retention effects in sand filters is vital for refining sand filter performance and guiding research on enhancing retention in other treatment stages. Moving forward, exploring the development of sand filter media that closely mimics natural environmental conditions presents an intriguing avenue of research. Additionally, investigating the impact of other contaminants on NPls' retention and transport behaviors warrants further inquiry to ensure comprehensive water treatment strategies.

The study sheds light on the complex interplay between surface functionalities, surfactants, and porous media in influencing NPls' retention and transport in sand filtration systems. These insights not only contribute to improving the efficiency of sand filtration in removing NPls but also inform the development of more effective water treatment strategies to safeguard drinking water quality.

Retention and Transport of Nanoplastics with Different Surface Functionalities in a Sand Filtration System

Hande Okutan[1,2,3], Gabriela Hul[2], Serge Stoll[2] and Philippe Le Coustumer[1,4,5,*]

[1]Ecole Doctorale, Sciences et Technologies, Université de Bordeaux Montaigne, 33607 Pessac, France; hande-mahide.okutan@etu.u-bordeaux-montaigne.fr
[2]Department F.-A. Forel for Environmental and Aquatic Sciences, University of Geneva, 1205 Geneva, Switzerland; gabriela.hul@unige.ch (G.H.); serge.stoll@unige.ch (S.S.)
[3]Department of Geological Engineering, Mugla Sitki Kocman University, Mugla 48000 Türkiye
[4]Earth Sciences Department, Université de Bordeaux, 33615 Pessac, France
[5]Bordeaux Imaging Center, Université de Bordeaux, CNRS-UAR3420–INSERM US4, 33000 Bordeaux, France
[*]Correspondence: philippe.le-coustumer@u-bordeaux.fr

Keywords: drinking water; nanoplastics; transport; retention efficiency; sand filtration; saturated column

Abstract

The efficiency of sand filtration was investigated in terms of the behavior of the nanoplastics (NPls) with different surface functionalities. The initial condition concentrations of NPls were varied, and their effects on retention and transport were investigated under a constant flow rate in saturated porous media. The behavior of NPls in this porous system was discussed by considering Z- average size and zeta (ζ) potential measurements of each effluent. The retention efficiencies of NPls were ranked as functionalized with amidine [A-PS]+ > with sulfate [S-PS]− > with surfactant-coated amidine [SDS-A-PS]−. The reversibility of the adsorption process was revealed by introducing surfactant into the sand filter system containing adsorbed [A-PS]+ at three different initial state concentration conditions. The deposition behavior on sand grain showed that positively charged NPls were attached to the quartz surface, and negatively charged NPls were attached to the edge of the clay minerals, which can be caused by electrical heterogeneities. The homoaggregates made of positively charged NPls were more compact than those made of negatively charged NPls and surfactant-coated NPls An anti-correlation was revealed, suggesting a connection between the fractal dimension (D_f) of NPL aggregates and retention efficiencies. Increased D_f values are associated with decreased retention efficiencies. The findings underscore the crucial influence of NPL surface properties in terms of retention efficiency and reversible adsorption in the presence of surfactants in sand filtration systems.

5.2. Introduction

The ubiquity of plastics in common use constitutes an environmental pollutant attributed to the deficiency in implementing suitable recycling methodologies (Geyer et al., 2017). Nanoplastics (NPls) and microplastics (MPLs) are emerging contaminants, and MPLs have been detected in freshwater sources such as surface water, groundwater, and wastewater (Koelmans et al., 2019; Mintenig et al., 2017; Velasco et al., 2020). The release of NPls into the environment can occur either in their original nano-sized form during the manufacturing of cosmetic and cleaning products, paints, pharmaceuticals, and electronics or through the degradation and weathering of MPLs (Birch et al., 2020). Therefore, NPls can be present in natural water resources in their pristine, coated, or aged form, depending on their origin.

The size criterium of NPls is plastic particles smaller than 1 µm in at least one of its dimensions (da Costa et al., 2016). Due to the dimensional characteristics of NPls, differentiating them from other pollutants, such as MPls, present in natural samples, the determination of their polymer type can be a challenging task. There is no standardized detection method for NPls dispersed in natural matrices, leading to a lack of information about NPl concentrations in environmental samples (Birch et al., 2020). In water treatment plants supplying drinking water, determining the NPls removal efficiency is vital because of the possible exposition of drinking water consumers to NPl particles.

The water treatment process is specific and depends on the drinking water treatment plant (DWTP) design. The main processes to remove dissolved and particle-based contaminants are coagulation/flocculation, sand filtration, activated carbon filtration, and disinfection (Y. Li et al., 2022; Negrete Velasco et al., 2022; Y. Zhang et al., 2020). Studies have been conducted to examine the effects of each process, individually or in combination, on the retention of NPls.

Coagulants (polyaluminum chloride) were found to be more efficient, and their lower amounts were sufficient to successfully aggregate polystyrene (PS) NPls of 90 nm (Ramirez Arenas et al., 2020). The removal efficiency for NPls was evaluated for the processes of coagulation/flocculation combined with sedimentation (CFS) and filtration. It was observed that the removal efficiency of NPls (180 nm) with CFS treatment is insufficient (Y. Zhang et al., 2020). The removal efficiency of sand filtration and activated carbon filtration processes for PS NPls of 110 nm was found to be 88.1% (Ramirez Arenas et al., 2022). The efficiency of sand filtration increased when the coagulation process was present. The removal capacity of the activated carbon filter was found to be more efficient than the one of the sand filter (Ramirez Arenas et al., 2022). In contrast, the retention of sand filtration was found to be more prone to retain the NPls than the activated carbon filter in the pilot-scale filtration unit. The difference may be caused by a biological active scum layer (schmutzdecke) in full-scale DWTPs (Pulido-Reyes, Magherini, Bianco, Sethi, Von Gunten, et al., 2022). It was revealed that by modifying granular activated carbon with zinc chloride ($ZnCl_2$), the adsorption capacity of PS NPls (100 nm) on granular activated carbon was significantly enhanced in the presence of lake water (Xing et al., 2023). As for the disinfection

process, it was stated that PS NPls (100 nm) have resistance to chlorination, but they can be degradable with ozonation (Y. Li et al., 2022). Ozonation with suitable doses at DWTPs resulted in negligible effects on the retention of NPls during the subsequent filtration steps (Pulido-Reyes, Magherini, Bianco, Sethi, Von Gunten, et al., 2022). The studies show that the contribution of the filtration phases is undeniably high, which serves as an initial barrier, complementing other processes in the treatment plant (Pulido-Reyes, Magherini, Bianco, Sethi, Von Gunten, et al., 2022; Ramirez Arenas et al., 2022; Y. Zhang et al., 2020). Nevertheless, there is still a high probability of the presence of particles smaller than 1 μm in tap water, which cannot be retained by DWTP (Y. Li et al., 2022). In order to prevent the presence of particles of such dimensions in potable water sources, it is crucial to examine the effects of different treatment processes with a specific emphasis on the sand filtration process that retains NPls (Pivokonsky et al., 2018). To manage and remediate the transport and fate of NPls, which are in the environmental pollutant class, it is necessary to achieve a better understanding of the processes behind this event.

The retention and transport mechanism of NPls in the sand filtration is expected to be controlled by (i) a collision mechanism: hydrodynamic forces, sedimentation, straining, interception, and Brownian diffusion; (ii) attachment mechanism: surface interactions potentials (van der Waals attraction and double layer repulsion); and (iii) detachment mechanism: change in flowrate and fluid chemistry (Compère et al., 2001; T. Zhang et al., 2015). The retention and transport behavior of NPls in a saturated porous medium is usually investigated with column experiments, which can represent the sand filter of DWTPs. The increase in the ionic strength, particle size, and heterogeneity of porous media leads to an increase in the retention of negatively charged PS NPls (Z. Dong et al., 2018). The initial concentration of positively charged PS NPls played a crucial role in the adsorption capacity of sand grains (G. Hul, Martignier, et al., 2024). The co-existence of NPls with other contaminants and natural materials will affect the behavior of transport and deposition in subsurface environments or filter systems (Y. Wang et al., 2022). The pH and ionic strength conditions of the solution are also directly bonded to the behavior of materials co-existing with NPls (Ling et al., 2021). The clay minerals can be found as a part of porous media that causes an increase in the retention of negatively charged NPls in quartz sand-type porous media (Liang et al., 2022; Lu et al., 2021). The presence of surfactants in the water environment inhibits aggregation and affects the mobility of NPls and MPLs by changing their charge (Y. Jiang et al., 2021, 2022; Peng & Wang, 2022).

The determination of fractal dimensions (D_f) in this study serves to clarify the condition of particle aggregations. Fractal geometry has emerged as a valuable tool for elucidating the intricately irregular structures present in aggregated systems. It is commonly recognized that the application of the fractal concept offers a valuable understanding of how aggregation mechanisms affect the structure of aggregates (Praetorius et al., 2020). The captured images from transmission electron microscopy (TEM) were used to analyze the fractal attributes of aggregates, and the D_f of nanoparticles was found in a range of 1.65 to 1.80 (Kanniah et al., 2012). The study by Chakraborti et al. [28] involved a fractal dimension analysis employing image processing techniques for the time-dependent change in aggregation of monodisperse PS latex microspheres with the addition of coagulation. This analysis unveiled the D_f in a range of values between 1.94 and 1.48.

The sand filtration stage is a common process in treatment facilities. There are limited studies investigating the impact of sand filtration solely on the retention of NPls with different surface functionalities. The assessment of the retention of NPls with positive and negative surface functionalities during sand filtration, as well as the evaluation of the influence of surfactants—which constitute the primary raw materials of most cleaning agents—on both the retention and re-transportation of retained NPls, highlight the unique contribution of this research. The assessment of the aggregation of the NPls' particles with fractal dimension calculations is another novelty of this study. Furthermore, obtaining comparable results for the behaviors of different NPls within the same environment underscores the originality of this study.

Driving our research is the fundamental hypothesis that the efficiency of sand filtration in retaining NPls is influenced by their surface functionalities, and this influence is further modulated by the presence of surfactant in the filtration system. The experimental conditions were integrated from the sand filtration system of the DWTP of Geneva (Switzerland) and were established under laboratory conditions with similar sand and flow rates conducted to explore the retention efficiency of the DWTP's sand filtration with the presence of different surface functional groups, coating, and concentration of PS latex NPls. The effect of surfactant on both adsorption and desorption processes was investigated. The emphasis of this study was particularly on (i) the effect of different surface properties of PS NPls on their transport in porous media, (ii) the behavior of surfactant-coated PS NPls during transport through the sand column, (iii) the reversibility of adsorption of positively charged PS NPls with surfactant introduction into the sand filter, and (iv) the aggregation properties were examined with TEM images and assessed with fractal dimension calculations.

5.3. Materials and Methods

5.3.1. Materials

Surfactant-free PS latex NPls with positive amidine functional groups -$C(NH_2)(NH_2)$+ on their surfaces were kindly provided by the Institute of the Analytical Sciences (ISA) affiliated with the National Centre for Scientific Research (Paris, France) and the University Claude Bernard (Lyon, France). The suspension contained 50 g/L of styrene transformed into PS with a conversion rate of 86%. The size of the positively charged amidine PS latex NPls ([A-PS]+) was determined by dynamic light scattering (DLS), and TEM was equal to 177 ± 4 nm and 147 ± 17 nm, respectively. Surfactant-free sulfate latex NPls with negative sulfate functional groups ($-SO_4^{2-}$) on their surfaces were purchased from Invitrogen (ThermoFisher Scientific, Basel, Switzerland). According to the manufacturer, they are characterized by a primary diameter of 0.1 µm, a density equal to 1.055 g/cm^3 at 20 °C, and a specific surface area of 5.9 x 10^5 cm^2/g. The size measurements of the negatively charged sulfate PS latex NPls ([S-PS]−) performed using DLS and TEM were comparable with the provider's specification and equal to 114 ± 1 nm and 109 ± 10 nm, respectively. Both stock solutions were kept in a dark place at a temperature of 4 °C and were used

to prepare solutions of lower concentrations. All dilutions were prepared in ultrapure water (Milli Q water, Millipore, Switzerland, with resistivity > 18 MΩ·cm and total organic carbon (TOC) < 2 ppb). A pH–titration curve was established for both types of NPls to determine their characteristics in changing pH conditions. A 50 mg/L suspension of each NPl type was titrated with diluted 1 M HCl and 1 M NaOH solution (Titrisol, Merck, Schaffhausen, Switzerland) in a pH range of 3.0 ± 0.1 to 11.0 ± 0.1. pH changes were controlled using a Hach Lange HQ40d portable meter (Hach Lange, Geneva, Switzerland).

Sodium dodecyl sulfate (SDS; AppliChem, purity > 99%, Darmstadt, Germany) solutions were prepared by dissolving the surfactant in ultrapure water and used without further purification to prepare SDS-8-coated PS amidine latex NPls ([SDS-A-PS]−). The latter was prepared by mixing PS amidine latex NPls solution of a given concentration with an SDS solution of a given concentration. Critical SDS concentrations were determined experimentally to obtain a complete coating of NPls surfaces and to avoid having free surfactants in the solution. Further information is given in Section S1 of Annex 5.A.

Fluoresceine sodium salt (Sigma Aldrich, Buchs, Switzerland) was used as an inert dye tracer to characterize the hydrodynamic parameters of porous media. A total of 1 g/L dye solution was prepared by dissolving a given amount of powder in ultrapure water. The stock solution and its dilutions were prepared right before use and protected from the direct influence of sunlight.

Quartz sand samples were provided by Carlo Bernasconi AG (Zürich, Switzerland), and they are composed of silica, i.e., 97–99%, along with other constituents in trace amounts, including Al_2O_3, K_2O, Na_2, TiO_2, Fe_2O, TiO, CaO, MgO, Fe_2O_3, and Na_2O. The size and morphology characteristics of sand grains determined using Camsizer (Retsch, Haan, Germany) were kindly provided by the Industrial Services of Geneva (Table S1). As reported before, sand grains carry a negative charge in a wide range of pH, i.e., from pH 1.0 ± 0.1 to pH 12.0 ± 0.1 (G. Hul et al., 2022). The sand samples were not submitted to any chemical treatment or purification and were thoroughly rinsed with ultrapure water before use. No special cleaning procedure was applied to better reflect conditions prevailing in the industrial sand filters and the natural environment. The sand porosity was found at a value of 0.41 ± 0.1 with fluorescent dye tracer experiments and calculated with advection and dispersion equations. The details can be found in the section S3 of Annex 5.A.

5.3.2. Methods

5.3.2.1. Z-Average Hydrodynamic Diameter and Zeta (ζ) Potential Measurements

Z-average hydrodynamic diameter and zeta (ζ) potential of [A-PS]+, [S-PS]−, and [SDS-A-PS]− NPls were determined with a Zetasizer Nano ZS (Malvern Instruments, Worcestershire, UK) using dynamic light scattering (DLS) and laser doppler velocimetry (LDV), respectively. All samples were measured after 1 min equilibration and at a temperature of 25 °C. The refraction index and absorbance for both types of PS NPls were set to 1.59 and 0.01, respectively. Z-average

hydrodynamic diameter and ζ potential calculations were based on five measurements, and each measurement consisted of ten runs. NPls size was calculated using the Stokes–Einstein relationship (Einstein, 1905), whereas ζ potential values were derived using the Smoluchowski approximation model (Smoluchowski, 1921).

5.3.2.2. Turbidity Measurements

The turbidity of the effluents was measured using a Hach Turbidimeter model TU 5200 (Hach Lange, Geneva, Switzerland) in NTU units. A relation between NPl concentration and turbidity was established by plotting turbidity vs. a known concentration of NPls A set of samples with PS NPls concentrations in the range of 0.1 mg/L to 50 mg/L was prepared for each type of NPls by diluting a given amount of stock solution in ultrapure water. The turbidity of each sample was verified after 15 min of stabilization at room temperature. In parallel, z-average hydrodynamic diameters and zeta potentials of NPls were verified with the ZetaSizer Nano ZS (Malvern Panalytical, Chipping Norton, Australia).

5.3.2.3. Scanning Electron Microscopy (SEM) and Transmission Electron Microscopy (TEM) Imaging

A JSM-7001FA (JEOL Ltd., Tokyo, Japan) scanning electron microscope (Department of Earth Sciences, University of Geneva, Geneva, Switzerland) and a Hitachi H7650 (Hitachi High-Tech Corp.,Tokyao,Japan) transmission electron microscope (Bordeaux Imaging Center, Bordeaux, France) were used to obtain images of different types of NPls The Hitachi instrument was employed for High-Contrast Transmission Electron Micrography (HC-TEM) within a high vacuum, employing magnifications ranging from 40 k to 100 k and an accelerating voltage of 80 kilo-electron volts (keV). A detailed description of the sample's preparation can be found in section S5 Annex 5.A.

5.3.2.4. UV-Vis Spectrophotometry

UV-vis spectrophotometry was used to determine fluoresceine sodium salt concentrations. To find a relation between dye concentration and absorbance, a series of samples with dye concentration in a range of 0 to 20 mg/L was prepared by diluting a given amount of stock solution in ultrapure water, and the absorbance of each sample was measured at the wavelength of 460 nm. All measurements were performed in a 1 cm path-length quartz cuvette at room temperature by using a DR3900 spectrophotometer (Hach Lange, Geneva, Switzerland). A calibration curve was established according to the Beer–Lambert law and subsequently used to calculate dye concentrations during column experiments (Annex Figure 5.S2.).

5.3.2.5. Column Experiments

The transport of different types of NPls in porous media was explored through wet-packed column experiments. As shown in Annex Figure 5.S5., the experimental setup consisted of the ultrapure water reservoir, silicon tubing, and acrylic column (36 mm inner diameter, 200 mm length of column) sealed with steel screens of mesh size of 250 µm and caoutchouc stoppers. An upward flow of ultrapure water was induced within the column using a peristaltic pump (Minipuls 3, Gilson, Mettmenstetten, Switzerland). The flow rate was adjusted to 20 ± 1 mL·/min for each experiment. While filling the column with wet sand grains, the sides of the column were gently tapped with a stick to avoid air bubble entrapment and to help the stationary phase settle tightly and correctly. Prior to each experiment, the column was equilibrated to the steady state condition by flushing ultrapure water for at least 2 h. During the experiment, 0.3 mL of NPls solution was injected into the column and followed by the background solution. The samples were collected manually every 60 s and 30 s after the NPls injection. After the experiment, a 1 cm layer of sand was collected near the inlet, the middle, and the outlet of the column to characterize changes on the sand surface with SEM imaging. In selected columns, 0.3 mL of SDS solution was injected into the columns after the filtration stage to examine the influence of surfactants on the remobilization of retained NPls The effluent concentration of NPls was determined with a turbidimeter, and the breakthrough curves were obtained by plotting the normalized concentration (C/C_0) versus time. All experiments were performed at least in triplicate. Breakthrough curves were then used to calculate recovered mass according to the following equation (Goldscheider & Drew, 2007):

$$m_R = Q \int_0^\infty C(t)\partial t \tag{5.1}$$

where m_R is recovered mass [M], Q [$L^3 \cdot T^{-1}$] is flow rate, and $C(t)$ is the tracer concentration by the time [$M \cdot L^{-3}$]. The retention efficiency was obtained with the following equation:

$$R = \frac{(m_i - m_R)}{mi} \times 100 \tag{5.2}$$

where R represents retention efficiency, and m_i represents the total injected mass [M] of NPls.

5.3.2.6. Aggregate Assessment with Fractal Dimension

The concept of fractal geometry was developed by B. Mandelbrot to understand the structural features and properties of various objects, such as colloidal aggregates (Mandelbrot, 1982). Utilizing fractal geometry to analyze different characteristics of aggregates presents a valuable avenue for deepening our understanding of aggregation processes and refining modeling techniques. Fractal dimensions can be delineated in linear, planar, or volumetric terms, yielding corresponding one-dimensional, two-dimensional, or three-dimensional values, respectively (Chakraborti et al., 2003). The two-dimensional TEM images of aggregates obtained from the peak point effluents of selected experimental conditions were used and treated with the FRACLAC

plugin of Image J FIJI 1.53t software (Ferreira & Rasband, 2012; Karperien, 1999). The box-counting method was used, which consists of estimating the area-filling properties of the boundary at various scales by counting how many boxes, F, are required to cover the object in a grid of a given size, ε (Landini, 2011). In other words, ε refers to the scale, which is the ratio of the box size to the image size. F is the number of pixels counted in per box (Karperien, 2004). This process is then repeated for multiple grids with increasing spacing. The slope of the log–log plot of ε (x-axis) versus F (y-axis) refers fractal dimension, $-D_f$. The D_f value obtained expresses the two-dimensional fractal dimension value. To verify the methodology, the D_f of the Sierpinski Carpet was computed, yielding a projected D_f value of 1.88, while its theoretical value stands at 1.89 (Torre et al., 2020).

5.4. Results

5.4.1. Characterization of NPls with Different Surface Functionalities

First, titration curves were established to characterize NPls behavior in different pH conditions and are presented in Annex Figure 5.S6. Annex Figure 5.S6a shows that [A-PS]+ NPls are positively charged until reaching the point of zero charge, where the adsorbent's net surface charge becomes neutral. This transition occurred at a pH value of 10.7 ± 0.1. Before charge neutralization, the mean z-average hydrodynamic diameter of [A-PS]+ NPls varies around 177 ± 6 nm, and the mean ζ potential is equal to 43 ± 2 mV. After charge neutralization, the z-average hydrodynamic diameter increases to approximately 600 nm, and the ζ potential becomes negative and equal to -21 ± 1 mV. Figure 5.S6b. demonstrates that [S-PS]− NPls are stable and carry a negative charge for the whole range of pH. The mean z-average hydrodynamic diameter of [S-PS]− NPls is equal to 116 ± 1 nm, and the mean ζ potential is equal to −43 ± 3 mV (Annex Table 5.S2.).

[A-PS]+ NPls were coated with SDS for selected experiments. The required amount of SDS for coating was estimated with batch experiments. According to the results, 1000 mg/L, 500 mg/L, and 100 mg/L [A-PS]+ NPls were completely coated in the presence of 500 mg/L, 400 mg/L, and 300 mg/L SDS concentrations, respectively.

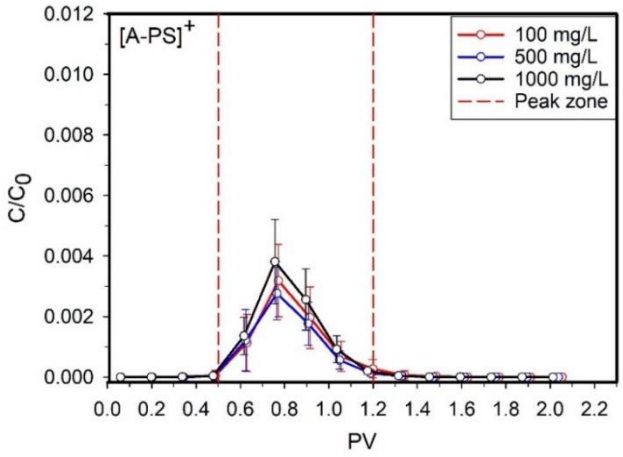
When the NPls are examined in terms of size according to TEM image analysis, the particles' long and short axis ratio is close to 1. The short axis was preferred for calculations. [S-PS]− NPls were observed as the smallest NPls with a diameter of 109 ± 10 nm, followed by [A-PS]+ NPls with a diameter of 147 ± 17 nm and [SDS-A-PS]− NPls with a diameter of 168 ± 17 nm (Annex Figure 5.S7. and Annex Table 5.S3.).

5.4.2. NPls Transport and Retention Behavior in Sand Filter

The transport of NPls was presented with normalized effluent concentration (C/C_0) as a function of the effluent solution volume pore volume (PV) in Figure 5.1. The z-average hydrodynamic diameters and ζ potentials versus the effluent solution volume of each effluent of selected injection concentration were measured. The peak zone of C/C_0 was shown at 0.5 and 1.2 PV for [A-PS]+ NPls and at 0.5 and 1.4 PV for [S-PS]− and [SDS-A-PS]− NPls In the overall curve, this is the range where the most transportation of NPls particles occurred (Figure 5.1.).

The variation of injection concentration affected the retained NPls amount in the porous media. When comparing the relationship between the retained mass percentages of [A-PS]+ NPls and the injected concentrations, there was an uneven trend. In general, their retention percentages are close to each other. Here, the highest mass retention was observed for 500 mg/L injection with 79%, while the lowest retention was observed for 1000 mg/L injection with 71% (Table 5.1). The intermediate experiments with 150 mg/L and 200 mg/L were performed to know the correlation of retained mass values (Annex Table 5.S4. and Annex Figure 5.S8.).

When the negatively charged particles were discussed, the effect of retention depending on the injected concentration was more noticeable than [A-PS]+ NPls The retention efficiency increased while increasing the injection concentration of both [S-PS]− and [SDS-A-PS]− NPls [SDS-A-PS]− NPls were also observed to have higher transportation than [S-PS]− NPls The maximum retention was equal to 55% for [S-PS]− NPls and 30% [SDS-A-PS]− NPls for 1000 mg/L. At the minimum injection concentration of 100 mg/L, all the injected [SDS-A-PS]− NPls were transported through the filtration column.



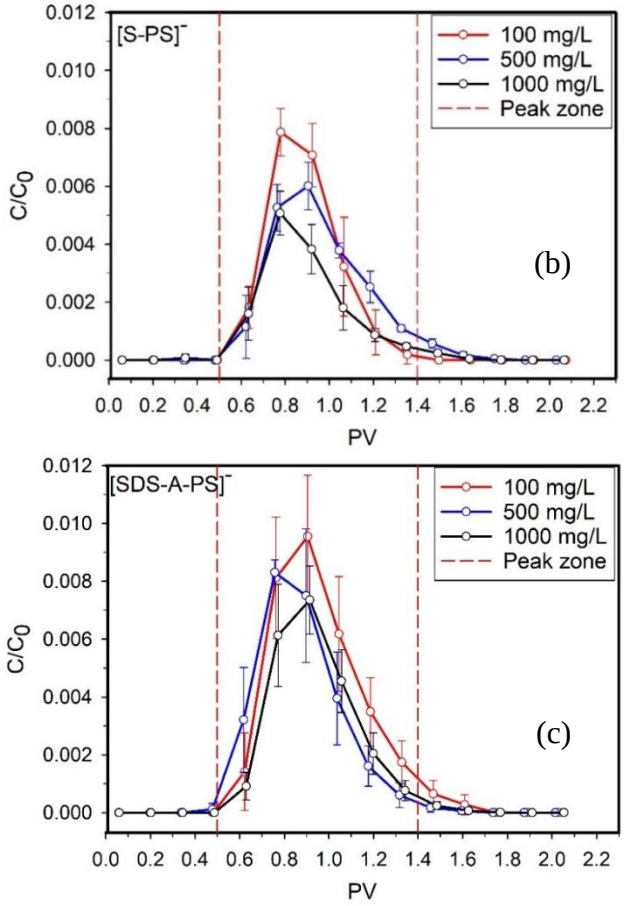


Figure 5.1. Breakthrough curves for 100 mg/L, 500 mg/L, and 1000 mg/L injection concentration (C_0) are shown for [A-PS]+ (a), [S-PS]− (b), and [SDS-A-PS]− (c) NPls

Table 5.1. Summary of injection conditions, maximum effluent concentrations (MEC), and retained mass values.

Type	Injection Concentration (mg/L)	MEC (mg/L)	Retention Efficiency (%)
[A-PS]+	100	0.4 ± 0.2	76 ± 9
	500	1.4 ± 0.4	79 ± 6
	1000	3.8 ± 1.2	71 ± 9
[S-PS]−	100	0.8 ± 0.1	32 ± 4
	500	3.1 ± 0.2	34 ± 2
	1000	5.1 ± 0.6	55 ± 3
[SDS-A-PS]−	1000	1.0 ± 0.1	3 ± 11
	100	4.4 ± 0.4	9 ± 10
	500	7.4 ± 1.0	30 ± 13

5.4.2.1. Effects of Injection Concentration

As particles approaching the sand grain surface experience no repulsive forces, they come into physical contact with the sand grain surface and become immobilized. Favorable attachment conditions cause fast particle deposition. These particles typically do not detach as the strong, attractive forces exceed the hydrodynamic drag forces (Molnar et al., 2015). Unfavorable

attachment conditions due to the presence of repulsive energy barriers lead to much slower particle deposition (Tufenkji & Elimelech, 2004). The breakthrough curves of [S-PS]− and [SDS-A-PS]− NPls are shown in Figures 5.2. and 5.3. The retention was observed in breakthrough curves significantly higher for [A-PS]+ than [S-PS]− and [SDS-A-PS]− NPls (Figure 5.1.).

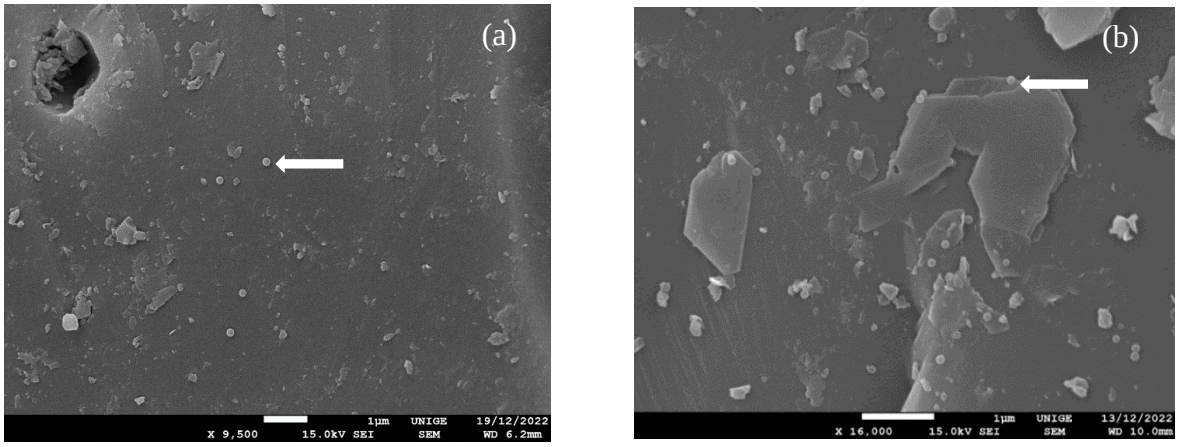
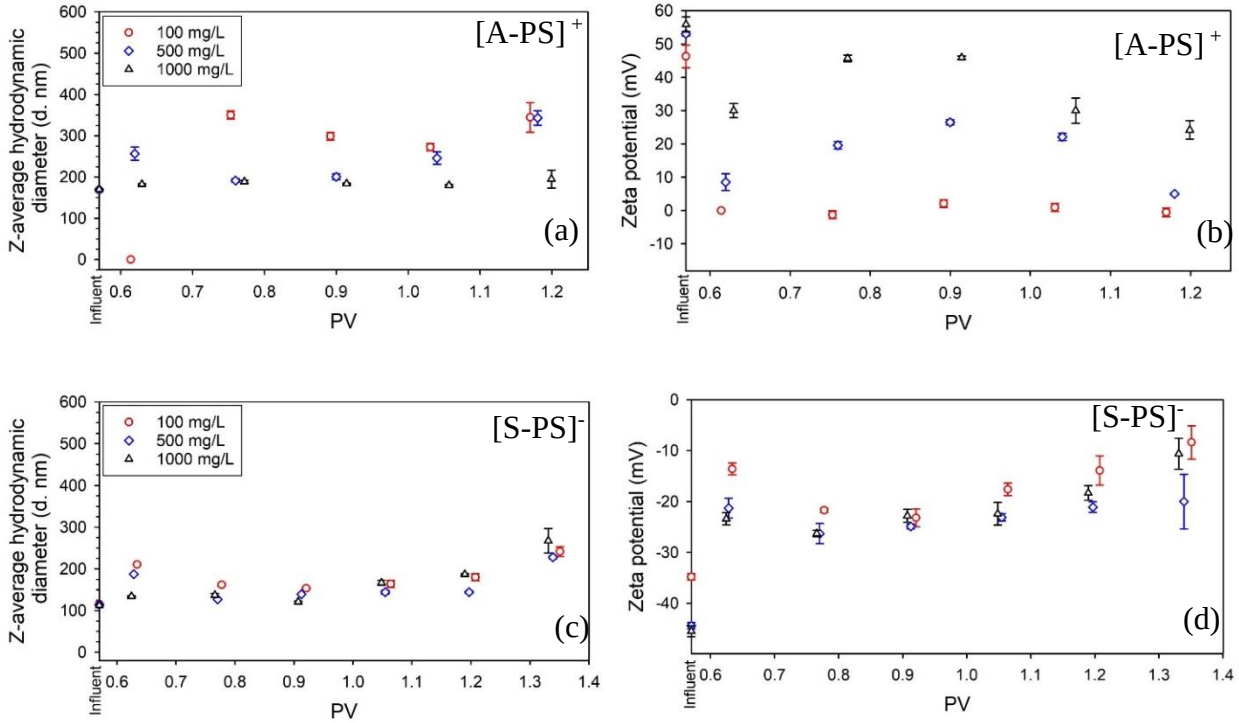


Figure 5.2. SEM micrography from the sand grain collected after the transport experiment. (a) Attachment of [A-PS]+ NPls onto the quartz surface and (b) attachment of [S-PS]− NPls onto clay minerals (white arrows).



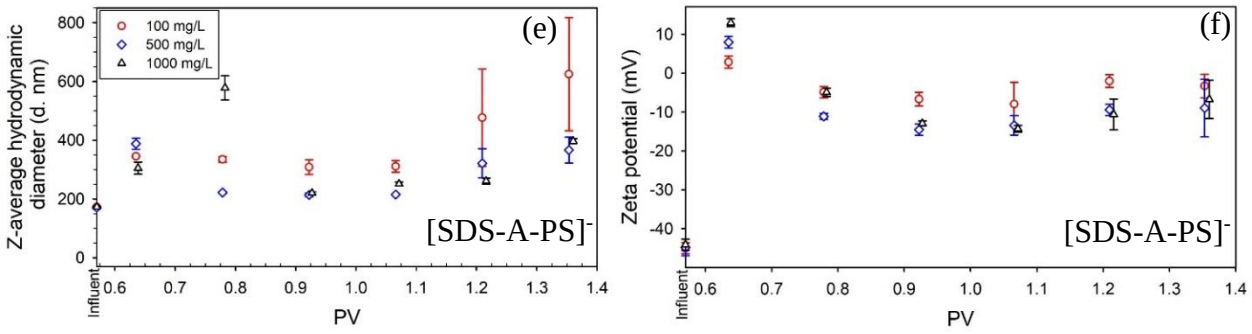


Figure 5.3. Collective representation of hydrodynamic diameter and zeta (ζ) potential vs. PV graphs of experiments performed with [A-PS]+ (a,b), [S-PS]− (c,d), and [SDS-A-PS]− (e,f).

For unfavorable attachment conditions, the increase in retention in porous media was caused by increasing the injection concentration of nanoparticles. It can be caused by the high collision probability, which occurs at high injection concentrations, and by the fact that already deposited NPls provide additional retention sites (Hou et al., 2017; P. Sun et al., 2015).

In contrast, our results indicated that an elevated injection concentration leads to a decline in retention. This trend is commonly observed in micrometer-sized particles, as reported by Hou et al. (Hou et al., 2020) and under the consideration of the straining effect (Bradford & Bettahar, 2006; Y. Sun et al., 2015). It was explained that the surface-active sites were filled more rapidly at higher concentrations, and progressive surface saturation caused a reduction in MPl retention in porous media (Hou et al., 2020). In theory, when the ratio between the diameter of the particle and the median size of sand grains decreases, the mobility of particles decreases in saturated porous media. The effect of straining can be considered if this ratio is higher than 1.7×10^{-3} as the threshold (Bradford et al., 2002). In our investigation, the straining process may be deemed less efficient, primarily attributed to the size of the calculated threshold based on individual particles. However, it is essential to acknowledge that the formation of homo or heteroaggregates could potentially induce this type of straining effect.

5.4.2.2. Effect of the NPls Surface Properties

Z-average hydrodynamic diameter and ζ potential measured for NPls present in the effluents are shown in Figure 5.3. For the [A-PS]+ NPls, which is a favorable aggregation condition, there is an increase in ζ potentials while increasing the injection concentration (Figure 5.3b.). The same phenomenon was observed for [S-PS]− and [SDS-A-PS]− NPls for absolute values, which incorporate previous findings (M. Zhang et al., 2023).

With the arrival of [A-PS]+ NPls concentration, 0.75 PV, for 100 mg/L injection conditions, an increase in particle size was observed from 168 ± 3 nm to 350 ± 10 nm. For ζ potential measurements, a constant trend is observed at the natural level. It can be stated that when the electrostatic attraction between sand and NPls decreases, transport rather than deposition of

particles is expected. Charge neutralization can cause instability and the settling of the particles on the grain surface as homo- or heteroaggregated particles that can explain the observation of more retention according to the 1000 mg/L injection concentration (Figure 5.3a–b.).

The impurities caused by the presence of clay minerals may influence the retention behavior of particles. Although the net charge of clay minerals is negative, the retention of NPls increases due to the occurrence of positive or less negative deposition zones resulting from charge heterogeneities on clay minerals (Lu et al., 2021). The clay minerals and their interactions with NPls on the sand surface were imaged with SEM. The [A-PS]+ NPls were generally deposited onto the quartz sand surface (Figure 5.2a). [S-PS]− NPls were observed to be attached to the edge of clay minerals (Figure 5.2b). It should be noted that the used sand contains a low percentage of impurities, about 1–3%. Depending on whether the porous medium contains trace amounts of clay minerals, NPls and clay particles can form heteroaggregates. In previous studies, it was observed that clay minerals adsorb at the MPLs surface and make charge differences in their surfaces in low ionic strength conditions (M. Li, Zhang, Yi, et al., 2021). The adsorption phenomena may lead to the measurement of neutrally charged values that we see at low injection concentrations of [A-PS]+ NPls Heteroaggregates can result in measuring a higher particle size.

For the injection concentration of 500 mg/L [A-PS]+ NPls, the size of particles in injection suspension was 170 ± 2 nm. At the first arrival of particles, 0.62 PV, an increase in particle size (256 ± 16 nm) was observed, then sizes decreased to 200 ± 7 nm for the peak point and increased again. In terms of ζ potential, the charge, which was 53 ± 1 mV for the initial condition, reached a maximum of 26 ± 1 mV at the peak point and decreased up to 5 mV with a decrease in concentration. The trend in the ζ potential is reflected in the opposite way to the size values.

For the highest injection concentration, the initial injected size was 170 ± 2 nm, and at the peak point, it was measured at 184 ± 1 nm. Regarding the change in ζ potentials, 56 ± 2 mV was measured for the injection suspension, 30 ± 2 mV was measured at 0.63 PV, increasing to 46 ± 1 mV at 0.9 PV, and the lowest 24 ± 3 mV was measured at 1.2 PV. When the size and electrical charge are evaluated together, it can be said that a high electrical charge prevents aggregation and retention in the sand filter (Y. Li et al., 2019). The lower stability observed for lower concentrations can be related to the lower magnitude of the particles' ζ potentials (Farrokhbin et al., 2019).

Considering the measurements with negatively charged NPls, the measured size of [S-PS]− NPls in the injection suspensions is 115 ± 1 nm, 114 ± 1 nm, and 112 ± 1 nm for 100 mg/L, 500 mg/L, and 1000 mg/L, respectively (Figure 5.3c.). For the three types of injection concentrations, an increase in size was observed with the first measurement of the concentration, a decrease in size at the peak, and an increase again with the decrease in the concentration. The size closest to the initial values was measured for the peak point with the injection concentration of 1000 mg/L. For ζ potential measurements, −35 ± 1 mV, −44 ± 1 mV, and −45 ± 1 mV, a strengthening trend with increasing concentration compared to the initial state. At 100 mg/L injection concentration, measurements started at −13 ± 1 mV and reached −23 ± 2 mV, PV 0.92, at the peak point (Figure 5.3d). The slight increases in z-average hydrodynamic diameter correspond with slight decreases

in ζ potentials due to a reduction in electrostatic repulsion, as explained by DLVO theory (J. Wang et al., 2021).

Experiments with two intermediate concentrations, 150 mg/L and 200 mg/L, are available for [A-PS]+ and [S-PS]−. For [A-PS]+, the ζ potential measurements of these two values vary between 2 and 4 mV. The z-average hydrodynamic diameter measurements for 150 mg/L and 200 mg/L are close to the initial case and follow a similar behavior with 500 mg/L. For [S-PS]−, there is a similar trend between 100 mg/L, 150 mg/L, and 200 mg/L injection concentrations for ζ potentials. In size measurement, there is an increase according to the initial injection concentration conditions (Annex Figure 5.S9.).

5.4.3. Effects of Surfactant Coating

In the case of [SDS-A-PS]− where negatively charged particles were formed by coating with SDS, initially, the sizes 172 ± 2 nm, 171 ± 2 nm, and 173 ± 2 nm were measured for 100 mg/L, 500 mg/L, and 1000 mg/L, respectively. As for the ζ potential measurements, the values measured for the injected suspension were −45 ± 1 mV, −45 ± 2 mV, and −44 ± 1 mV, respectively, from low to high injection concentrations (Figure 5.3e–f.).

For 100 mg/L injection concentration, at 0.63 PV, the determined size was equal to 345 ± 2 nm, and at the peak point of 0.92 PV, it was equal to 308 ± 25 nm. After the peak point, the size increased. For 500 and 1000 mg/L injection concentrations, the same trend was observed, but the size increase was less and, at the peak, 0.92 PV, equal to 214 ± 6 d. nm for 500 mg/L and 220 ± 4 nm for 1000 mg/L. Unlike [S-PS]−, more differences were observed at 100 mg/L conditions compared to the other two conditions.

Positive values were measured in the first concentration measurements, then at peak concentrations, 0.92 PV, −7 ± 2 mV, −14 ± 1 mV, and −13 ± 1 mV for 100 mg/L, 500 mg/L, and 1000 mg/L were measured, respectively. The positive values can be explained by the presence of uncoated [A-PS]+ NPls The surfactant coating on NPls may undergo desorption when diluting the surfactant-NPls suspension.(Jódar-Reyes et al., 2006). If the electrostatic force was greater than the adhesion force of the SDS molecules on the PS surface, this could be caused by the detachment of SDS molecules from the PS surface (Y. Jiang et al., 2022).

When the transport of NPls injected with negative ζ potentials in two different ways is compared, it is observed that [S-PS]− NPls are more strongly negatively charged than [SDS-A-PS]−, but in terms of transport, [SDS-A-PS]− was more transported. It could be concluded that the adhesive work of SDS and the decrease in surface tension increased the mobility of the NPls

5.4.4. Remobilization

The favorable attachment condition was examined in terms of desorption while injecting SDS solution into the sand filter after transport experiments at 100 mg/L, 500 mg/L, and 1000 mg/L initial concentrations of [A-PS]+ NPls

The recovery rates after both [A-PS]+ NPL and SDS solution injection were calculated. The maximum total recovered mass was measured for 100 mg/L injection conditions as 47%. The comparison between [A-PS]+ NPls injection and SDS solution injection is shown in Table 5.2. The breakthrough curves of each condition are presented in Annex Figure 5.S10.

Table 5.2. Total recovered mass from the experiments and the percentage of this total mass recovered after [A-PS]+ injection and SDS injection are shown. Recovered mass 1 represents the recovered mass percentage after NPL injections. Recovered mass 2 represents the recovered mass percentage after SDS solution injection, which is expected to cause remobilization of the sorbed NPls The total recovered mass percentage shows the recovered percentage according to initial conditions after both injections.

Injected NPL Concentration (mg/L)	Recovered Mass 1 * (%)	Recovered Mass 2 ** (%)	Total Recovered Mass (%)
100	31 ± 6	16 ± 4	47 ± 8
500	20 ± 6	10 ± 2	30 ± 5
1000	34 ± 8	7 ± 2	42 ± 6

* After [A-PS]+ NPL injection, ** After SDS solution Injection.

In the case of 100 and 500 mg/L concentrations, 16% and 10% were recovered after SDS solution injection. For the 1000 mg/L concentration, the recovered mass after the SDS solution injection is 7% of the retained mass were recovered.

After the injection of the SDS solution, the effluent samples initially consisted of positively charged particles, followed by negatively charged particles. As a result of the SDS solution injection, [A-PS]+ NPls became coated with SDS. This is followed by desorption due to the development of repulsive forces caused by negatively charged particles and sand (Figure 5.4a.). Considering the z-average hydrodynamic diameter evolution, values close to the first case are observed for the peak zone for 500 mg/L and 1000 mg/L. For 100 mg/L, it can be assumed that aggregates or impurities are transported (Figure 5.4b.). In addition, the low mass presence may have reduced the precision of the measurement. The increases in the standard deviations for all three concentrations examined indicate that larger impurities and possibly aggregates may have been transported at the end of the experiment due to the continuous flow.

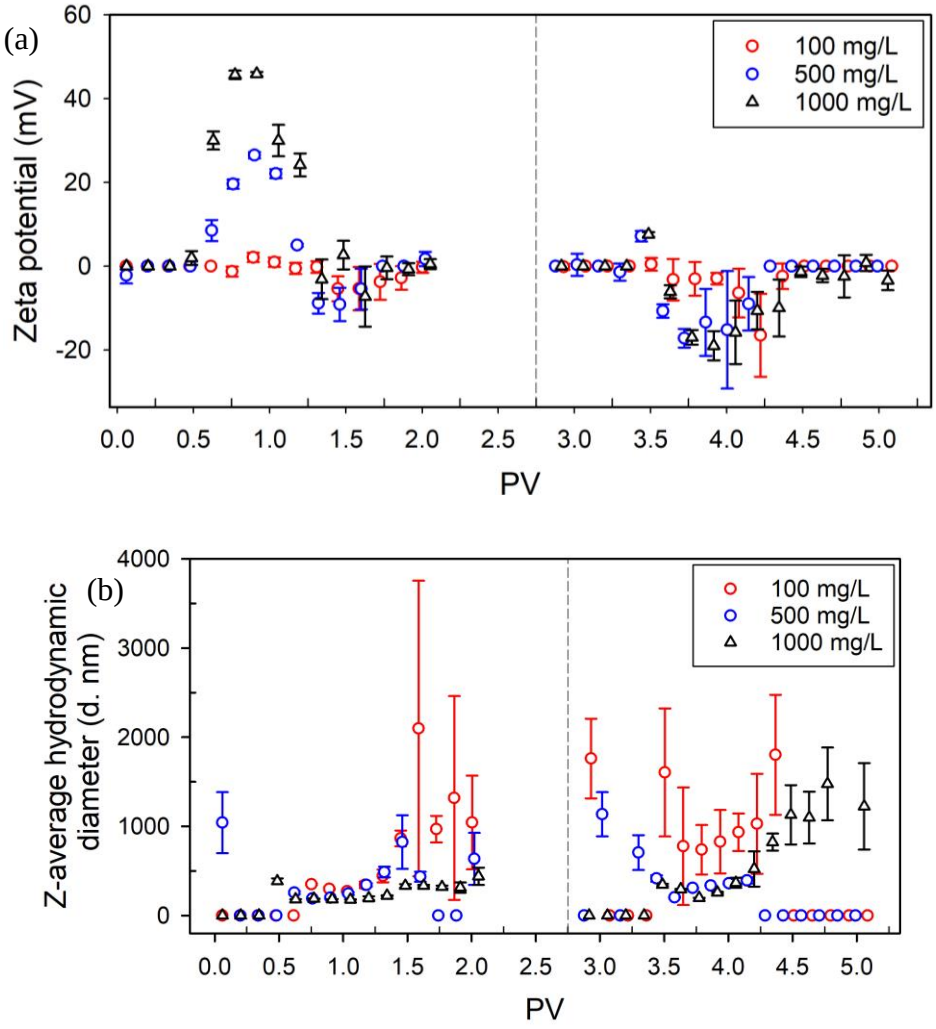


Figure 5.4. ζ potential measurements (a) and z-average hydrodynamic diameter (b) of effluents. The dashed line represents the SDS solution injection.

5.4.5. Aggregate Properties

Samples were collected corresponding to the peak points at which experiments conducted with initial concentrations of 100 mg/L, 500 mg/L, and 1000 mg/L reached their maximum concentration. These selected samples were examined using TEM, and images describing the homoaggregates of NPls were captured and utilized for the analysis of fractal dimensions.

In Figure 5.5., the relation of D_f values between injection concentration and NPL type was plotted, which were calculated from the slope of the log–log plot of ε vs. F (Annex Figure 5.S11.). Given the studies indicating the fractal geometries exhibited by nanoparticle aggregates (Chakraborti et al., 2003; Kanniah et al., 2012), fractal analyses were conducted to ascertain the presence of two-dimensional fractal geometries in the observed aggregates of NPL effluent samples examined via TEM.

In the case of [A-PS]+ NPls, higher injection concentrations led to the formation of denser fractal aggregates. Conversely, for [S-PS]− and [SDS-A-PS]− NPls, increased injection concentrations resulted in less compact fractal aggregates. This suggests that NPls with varying ζ potentials exhibit contrasting aggregation behaviors in terms of compactness. For the lowest concentration, 100 mg/L, [S-PS]− and [SDS-A-PS]− NPls showed denser aggregates than [A-PS]+ NPls When examining two negatively charged particles, the most notable distinction was evident in the scenario of 500 mg/L initial injection conditions. Here, it was observed that [S-PS]− aggregates exhibited higher compactness compared to [SDS-A-PS]− aggregates (Figure 5.5.). The changes in D_f values observed during remobilization experiments involving the introduction of an SDS solution into the sand filter with adsorbed [A-PS]+ NPls followed a nearly linear trend. As a result, in cases of remobilization, it can be deduced that alterations in the concentration of injected NPls do not have a discernible impact on the outcome.

The phenomenon of homoaggregation is recognized to influence transport processes, leading to retention through straining effects and deposition on collector surfaces (G. Hul et al., 2021). Considering the relationship between fractal dimension values and retained mass ratios, the impact of homoaggregation on retention was evaluated for the same type of NPls (Table 5.3.). For [S-PS]− and [SDS-A-PS]− NPls, the variations in retained mass ratios ($R_{\%}C_0$) and fractal dimension values (D_f-C_0) in relation to injection concentrations (C_0) are outlined as follows: $R_{\%1000} > R_{\%500} > R_{\%100}$ and $D_{f100} > D_{f500} > D_{f1000}$, respectively. When both of these assessments are considered collectively, it is observed greater retention efficiency in cases with less compact aggregates. In the case of [A-PS]+ NPls, as with negatively charged particles, an increase in aggregate density led to a decrease in retention. However, in contrast to negatively charged particles, an increase in injection concentration resulted in higher compactness and lower retention in this context. The variation for [A-PS]+ NPls can be shown as follows: $R_{\%500} > R_{\%100} > R_{\%1000}$ and $D_{f1000} > D_{f500} > D_{f100}$. It is relevant to mention that the retained mass percentages exhibited a minimal difference between the 500 and 100 mg/L injection concentrations for [A-PS]+ NPls The increase in aggregate density, resulting in a decrease in aggregate size, subsequently led to a reduction in the retention percentage.

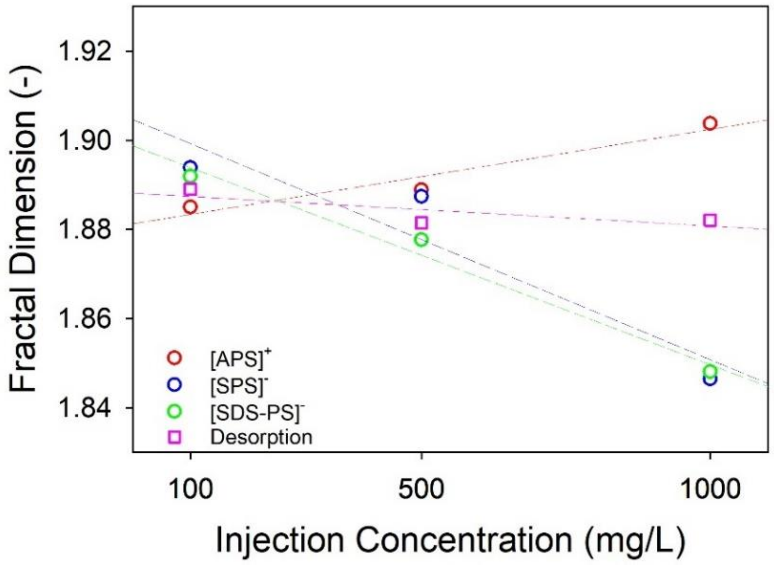


Figure 5.5. Fractal analyses results for each concentration, type of NPL, and desorbed sample. Three images of aggregates were used for each condition.

Table 5.3. The overall presentation of retention efficiency and fractal dimension values.

Type	Injection Concentrations	Fractal Dimension, D_f	Retention Efficiency, %
[A-PS]+	100	1.885 ± 0.017	76 ± 9
[A-PS]+	500	1.889 ± 0.019	79 ± 6
[A-PS]+	1000	1.904 ± 0.003	71 ± 9
[S-PS]−	100	1.894 ± 0.026	32 ± 4
[S-PS]−	500	1.887 ± 0.012	34 ± 2
[S-PS]−	1000	1.846 ± 0.005	55 ± 3
[SDS-A-PS]−	100	1.892 ± 0.005	3 ± 11
[SDS-A-PS]−	500	1.878 ± 0.015	9 ± 10
[SDS-A-PS]−	1000	1.848 ± 0.017	30 ± 13
Desorption	100	1.889 ± 0.022	52 ± 8
Desorption	500	1.881 ± 0.014	70 ± 5
Desorption	1000	1.882 ± 0.015	58 ± 6

5.4.6. Summary of Mechanism

The mechanisms of NPls retention in sand filters are schematically illustrated in Figure 5.6. In a stable state, three different types of NPls were introduced into quartz sand-type saturated porous media representing the sand filtration phase. Due to the attractive forces between the quartz sand and [A-PS]+ NPls resulting from their opposite charges, the retention of [A-PS]+ NPls was higher compared to [S-PS]− and [SDS-A-PS]− NPls, which have repulsive interactions. Surfactant-coated negatively charged [SDS-A-PS]− NPls were retained less than function group-dependent negatively charged [S-PS]− NPls Due to charge heterogeneities, negatively charged particles are

attached to the corners of clay minerals. Positively charged particles, on the other hand, are attached to quartz minerals. With the injection of surfactant into the sand filter containing adsorbed [A-PS]+ NPls, a charge inversion occurred, causing the positively charged particles present in the media to undergo transport in a negatively charged state.

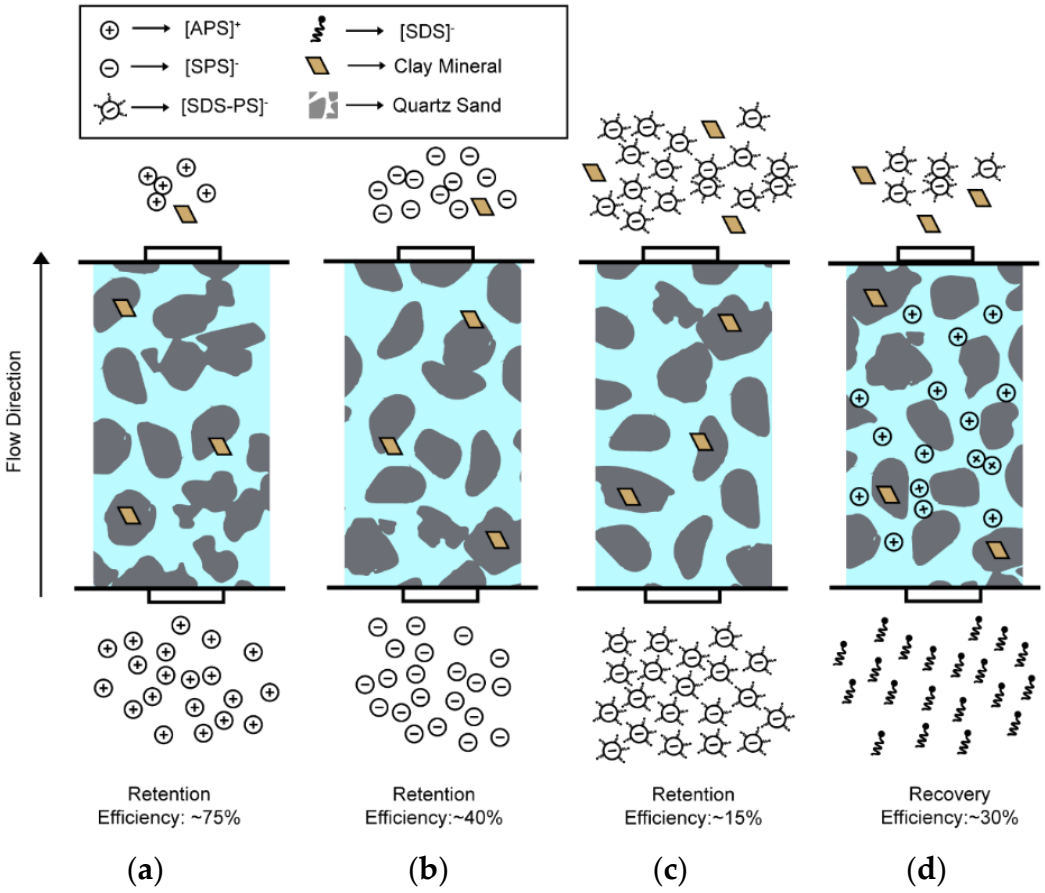


Figure 5.6. The schematic overview depicts the transport and retention process of NPls within a sand filtration column which is quartz sand and characterized as a saturated porous medium. Panels (a), (b), and (c) illustrate the retention efficiencies for [A-PS]+, [S-PS]−, and [SDS-A-PS]− NPls, respectively. Panel (d) presents the re-mobilization of adsorbed [A-PS]+ upon the introduction of an SDS solution.

5.5. Conclusions

Transport experiments were performed to investigate the behavior of NPls in a laboratory-based sand filtration column with similar sand and flow rate properties of the DWTPs of Geneva (Switzerland). The impact of surface functionality, as well as the presence of surfactant in both coating and solution forms, on adsorption and desorption in porous media was examined through measurements of z-average size and ζ potential. The breakthrough curves were established with turbidity measurements for the calculation of retention and transport efficiencies. The aggregation definition and comparisons were made with fractal dimension analysis from TEM imaging.

Our research highlights that the surface charges of NPls, resulting from various surface functionalities or coatings with surfactant molecules, yield distinct and crucial impacts on the retention behavior within porous media. In cases where the NPls surface charge is identical to the porous media (here, quartz sand grains) or the presence of a surfactant surface coating, retention is limited if the comparison is made with oppositely charged NPls The average retention efficiency of [A-PS]+, [S-PS]−, and [SDS-A-PS]− NPls were 75%, 40%, and 15%, respectively, across all injection concentrations. This means that electrostatic interaction forces play a major role. Different surface functionalities of NPls result in varying degrees of retention within saturated porous media during sand filtration. Despite both [S-PS]− and [SDS-A-PS]− NPls initially bearing a negative charge, those particles coated with an anionic surfactant, [SDS-A-PS]−, exhibited lower retention in the sand filter. The compactness of aggregates has effects that correspond to the retention efficiencies. The density of aggregates exhibits effects that align with retention efficiencies. The results interpretation of the homoaggregation of the NPls in the effluents showed that [A-PS]+ NPls are forming more compact aggregates than the [S-PS]− and [SDS-A-PS]− NPls For NPls with similar characteristics, an increase in fractal dimension values, which signifies greater aggregate compactness, was observed to lead to a decrease in retention efficiencies. This increased compactness can be attributed to the smaller aggregate sizes, providing an explanation for the decrease in retention efficiencies.

The ζ potential demonstrated an obvious rise in positively charged particles as particle concentrations increased. However, in contrast, the effect of concentration variations on the negatively charged particles was less noticeable compared to positively charged particles. This may have also increased the retention of positively charged particles. It has been shown that particles retained in the sand filter can be released by the introduction of surfactant in the sand filter with retained NPls This remobilization was observed as a maximum transport of 35% from the retained [A-PS]+ NPls compared to the initial situation.

The sand filtration phase is essential for eliminating suspended particles and constitutes an integral component of DWTPs. It serves as a protective barrier, preventing particles from entering more delicate treatment processes like disinfection, where they might block or diminish the effectiveness of these procedures. This phase is not only cost-effective but also aligns with sustainable water treatment practices, as it operates through a natural process without reliance on chemicals, making it an environmentally friendly choice. Investigating the retention effects of sand filters on NPls holds significant importance, both for refining sand filter performance and for guiding research toward enhancing the retention of unretained components in other stages of DWTPs. Additionally, it has come to light that the remobilization rate of retained NPls, which may be transported into the subsequent phase with the introduction of pollutants such as surfactants, is a noteworthy consideration. Exploring whether other contaminants induce similar behavior warrants further inquiry. From a future perspective, developing a sand filter media with physical and chemical conditions closer to the natural environment presents an intriguing avenue of exploration.

Annex 5.A. Supplementary Information

S1. Sodium dodecyl sulfate (SDS) critical concentration determination

A critical SDS concentration, for which all surfactant molecules present in the solution are adsorbed on the nanoplastics surface, was estimated for different polystyrene amidine latex nanoplastics (NPls) concentrations. A solution of given polystyrene amidine latex NPls concentration and of given SDS concentration was prepared and mixed using an orbital shaker (IKA KS 260, Germany) for at least 15 min. The z-average hydrodynamic diameter and the zeta (ζ) potential of NPls were subsequently measured using ZetaSizer Nano ZS. The SDS critical concentration corresponds to the first concentration for which ζ potential of NPls stops changing and has roughly the same value. A formation of a plateau of ζ potential values for 100 mg/L, 500 mg/L, and 1000 mg/L PS NPls was observed for 300 mg/L, 400 mg/L, and 500 mg/L SDS concentration, respectively (Annex Figure 5.S1.). These concentrations were subsequently used to prepare SDS-coated PS amidine latex NPls.

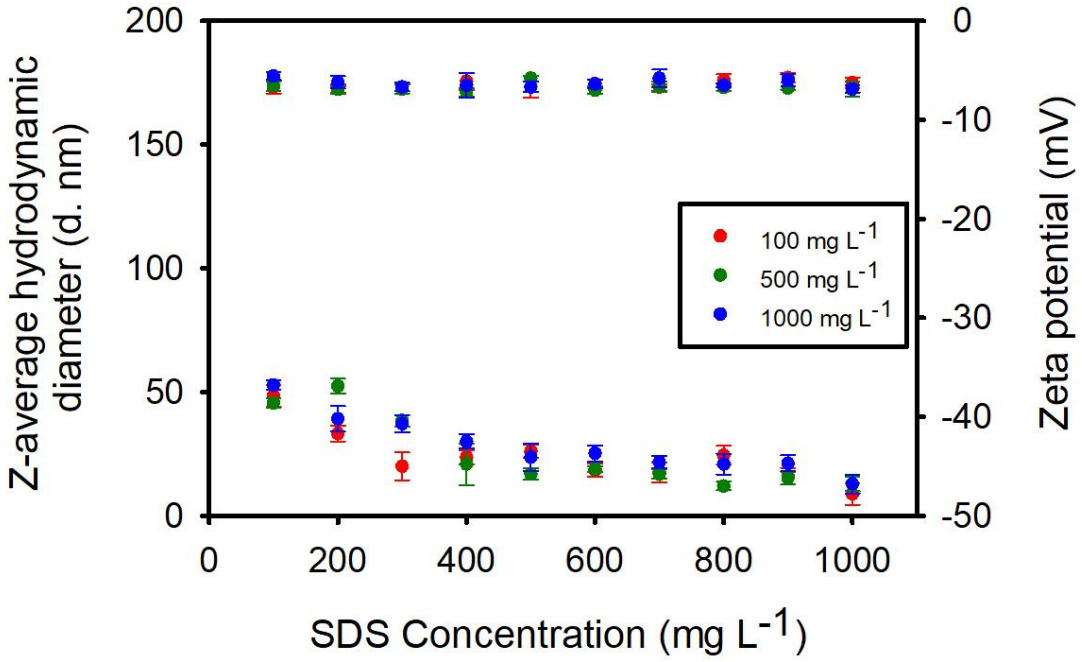


Figure 5.S1. SDS critical concentrations for different polystyrene amidine latex nanoplastics concentrations. Experimental conditions: ultrapure water.

S2. Sand grains characteristics provided by the Industrial Services of Geneva (SIG)

Table 5.S1. Sand grains characteristics determined with Camsizer (Retsch). Sand grains belong to 11 granulometric classes and mainly have sizes comprised between 2.38 and 2.83 mm, 2.83 and 3.36 mm as well as between 3.36 and 4.00 mm. They are of ellipsoidal shape, with an average width-to-length ratio equal to 0.655, and their surfaces are rather heterogenous, with an average roughness equal to 0.826 and an average convexity close to 1.

Grain size (mm)	Volume proportion of particles in the range (%)	Cumulative distribution (%)	Sphericity	Aspect ratio	Convexity
0 - 0.75	0.05	0.05	0.785	0.660	0.979
0.75 – 1	0.00	0.05	0.806	0.581	0.992
1 – 1.2	0.01	0.06	0.567	0.328	0.979
1.2 – 1.5	0.07	0.13	0.577	0.310	0.982
1.5 – 2	1.54	1.67	0.708	0.437	0.986
2 – 2.38	7.26	8.93	0.774	0.529	0.988
2.38 – 2.83	24.74	33.67	0.823	0.622	0.989
2.83 – 3.36	40.64	74.31	0.845	0.692	0.989
3.36 – 4	22.98	97.29	0.848	0.728	0.987
4 – 4.76	2.67	99.96	0.826	0.761	0.982
> 4.76	0.04	100	0.654	0.742	0.956

S3. Porosity calculations of sand

The porosity properties of quartz sand were investigated with a fluorescein tracer experiment and its mathematical equation was implemented with 1D Advection and Dispersion Equations which are described for the solute transport in a flow channel as follows:

$$\frac{\partial C}{\partial t} = D_L \frac{\partial^2 C}{\partial x^2} - u \frac{\partial C}{\partial x} \quad (5.S1)$$

Where C is solute outflow concentration [ML^{-3}], t is time variable [T], x is the distance [L], D_L [L^2T^{-1}] and u [LT^{-1}] are the dispersion coefficient and mean velocity, respectively (Maloszewski et al., 1992).

Its analytical solution for instantaneous solute injection in a semi-infinite medium was expressed by Kreft and Zuber (Kreft & Zuber, 1978) and used for porosity calculations while doing inverse modeling between experimental and model values.

The used analytical equation is for instantaneous solute injection in a semi-infinite medium follows:

$$C_i(x,t) = \frac{M_0\, x}{A\, n_e\, u_x \sqrt{4\pi D_x t^3}} \exp\left(-\frac{(x-u_x t)^2}{4D_x t}\right) \quad (5.S2)$$

where Ci is Concentration at the sampling point [ML^{-3}], M_0 is recovered mass [M], x is the distance between the sampling point and the injection point [L] u is the mean velocity [LT^{-1}], DL is dispersion coefficient [L^2T^{-1}], t is time [T], A is the Cross-sectional area of column [L^3] and n_e is effective porosity [-].

The fluorescein sodium salt concentration was measured in 460 nm with spectrophotometer both establishing calibration curve and column experiment effluents. The correlation coefficient, intercept and slope are found as 0.99, -0.007 and 0.076, respectively.

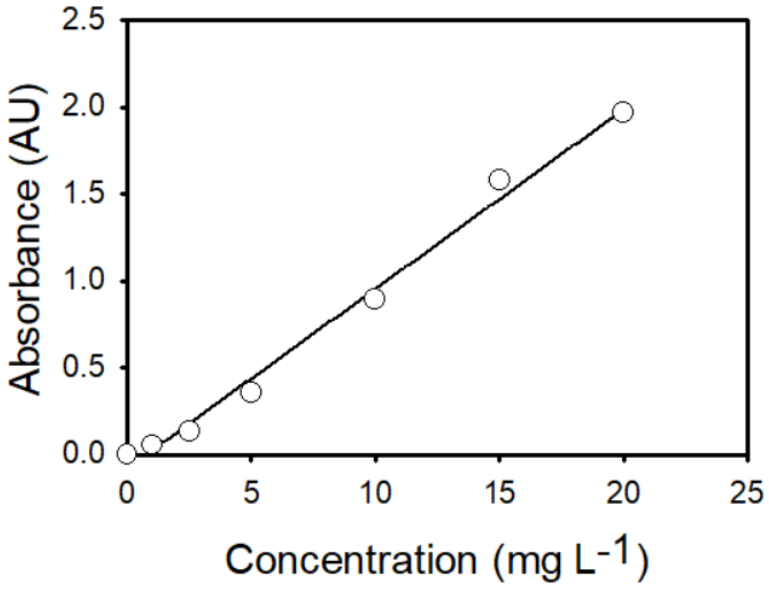


Figure 5.S2. The calibration curve which has relation between absorbance and concentration of fluorescein sodium salt.

The porosity was calculated as 0.41 ± 0.1 by fitting experimental breakthrough curve to model breakthrough curve while manipulating porosity, mean velocity, and dispersion coefficient values with solver extension in Excel.

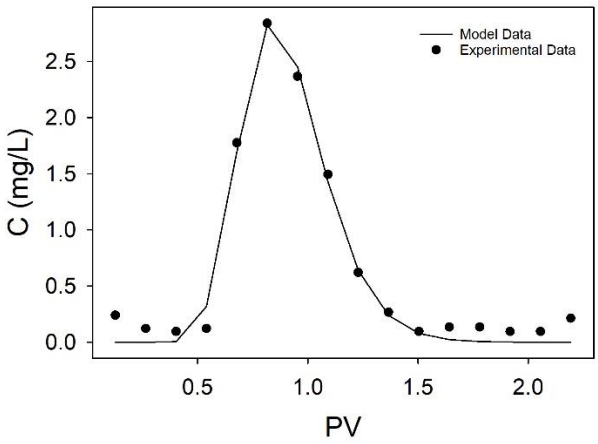


Figure 5.S3. The experimental breakthrough curve and Model breakthrough curve after fitting procedure. The dye tracer experiment is duplicated.

S4. Turbidity measurements

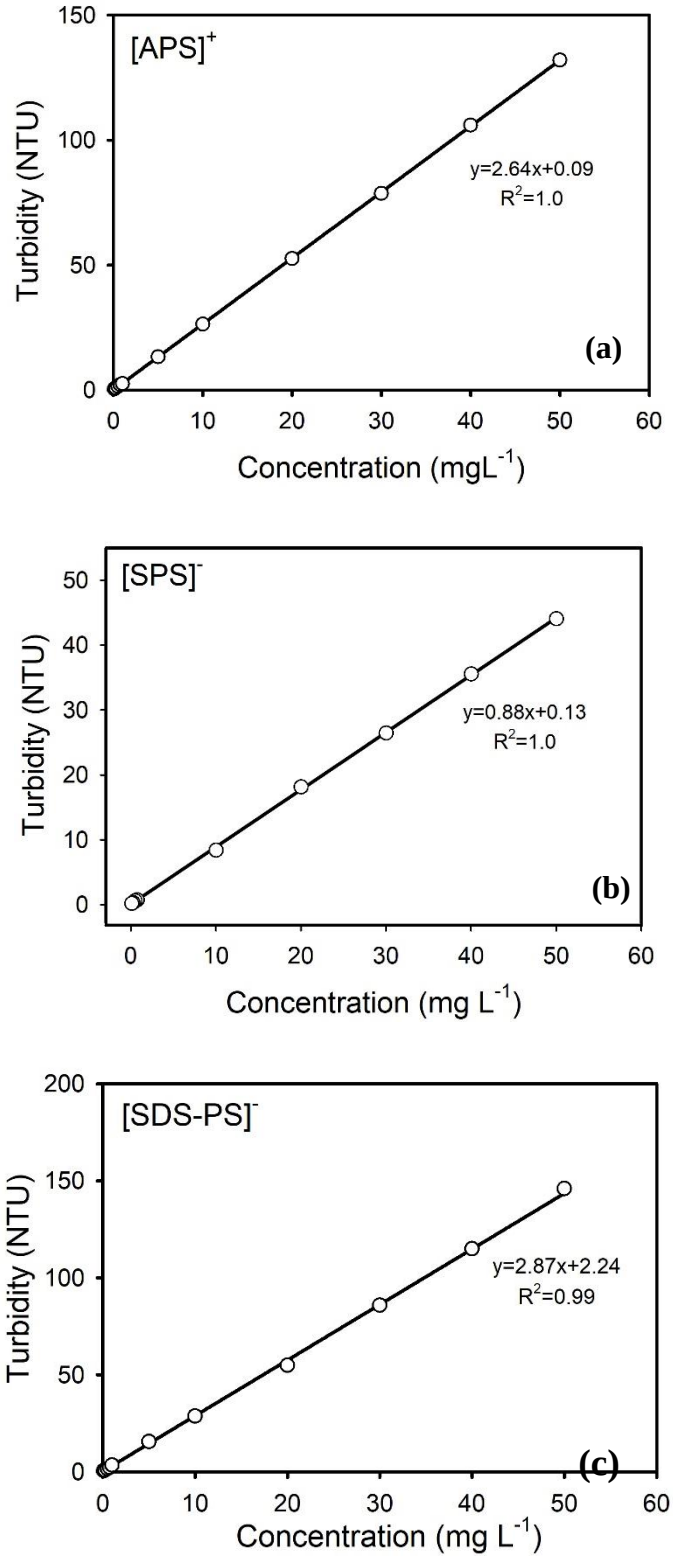


Figure 5.S4. The calibration curves which presents relation the concentration and turbidity measurements for [A-PS] + (a), [S-PS]- (b) and [SDS-A-PS]- (c).

S5. Preparation of SEM/TEM samples

S5.1. Preparation of solid samples for SEM imaging

A thin layer of a special glue was first spread out on the 5 × 5 mm silicon wafer (G3390, Agar Scientific) attached to an aluminum stub with a diameter of 12.7 mm. Then, a few sand grains sampled from the filtration column were placed and delicately embedded in the glue up to half of their height. Such prepared samples were air-dried for at least 48 hours. Prior to analysis, they were also covered with 10 nm gold coating.

S5.2. Preparation of liquid samples for TEM imaging

The carbon and holey carbon support with copper grids was used to deposit 10 µL (one drop) of NPls dispersions or effluent samples. The grids were dried under a glass cover with infrared lamp and introduced to the microscope (Hitachi H7650).

S6. Column Experiments

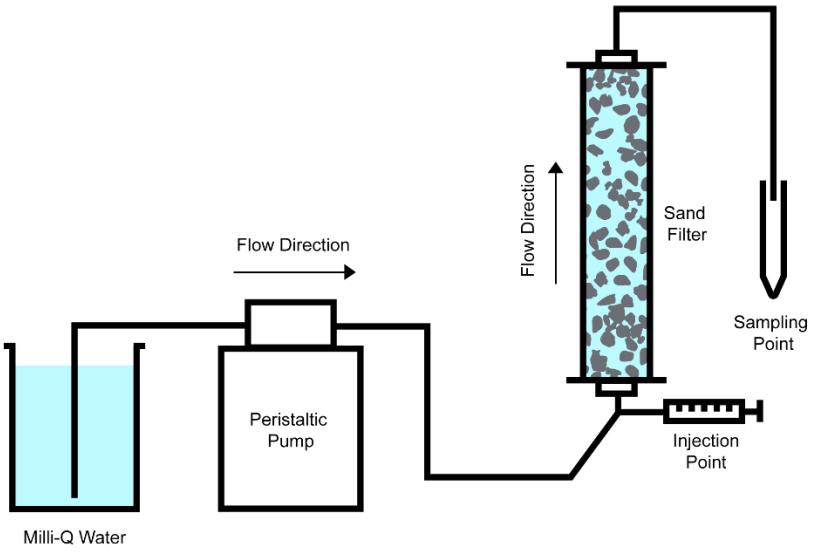


Figure 5.S5. The schematic illustration of used experimental setup.

S7. Characterization of NPls with different surface functionalities

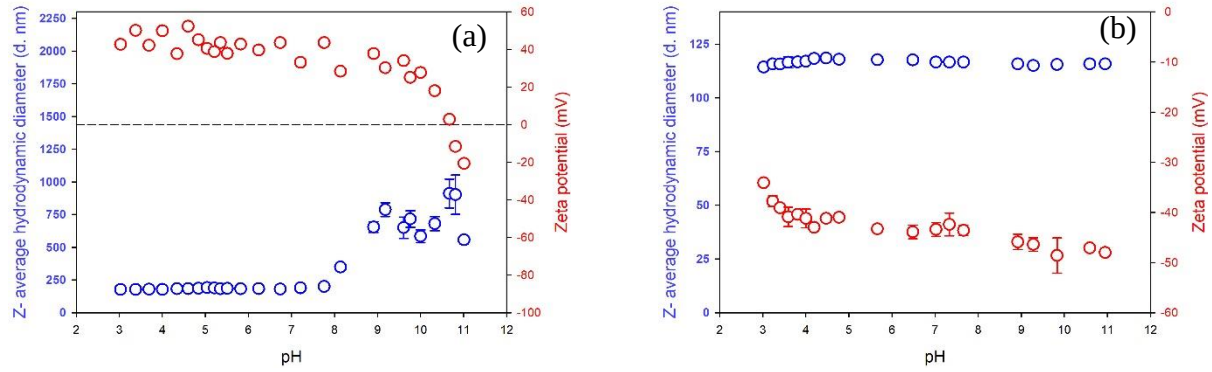
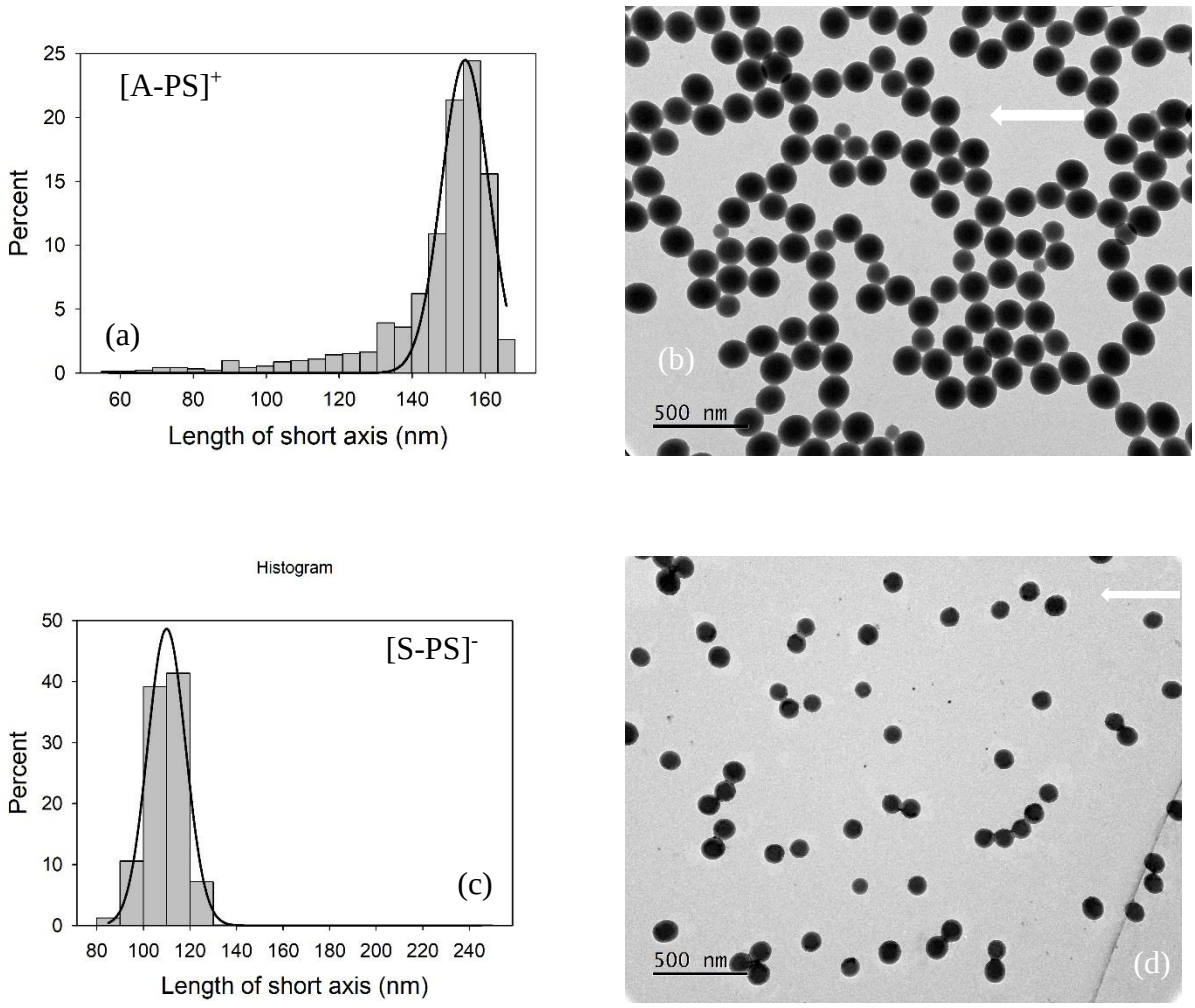


Figure 5.S6. Size and ζ potential titration curves for (a) [A-PS]+ and (b) [S-PS]-.



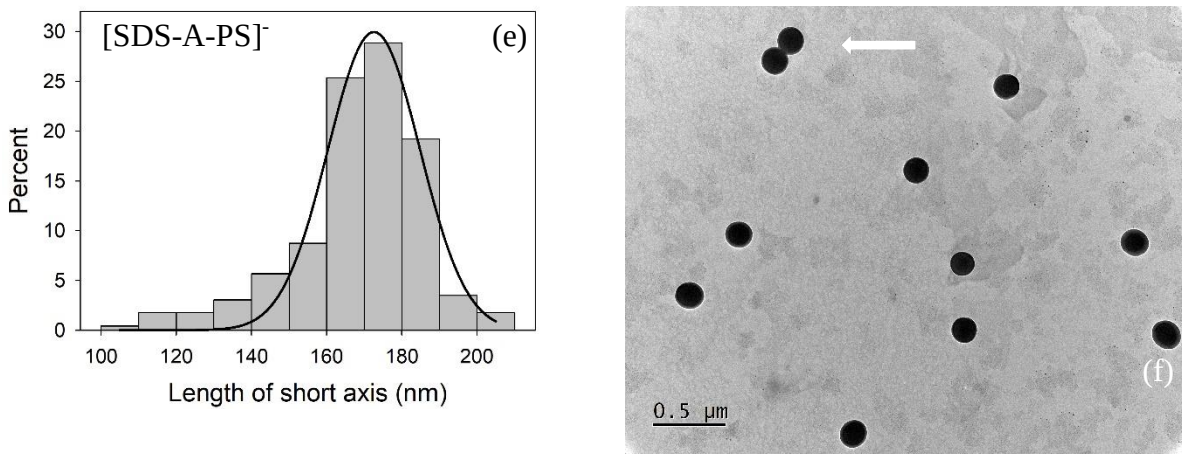


Figure 5.S7. (a, b) [A-PS] + (c, d) [S-PS]- (e, f) [SDS-A-PS]- NPls (white arrows) size distribution which was measured from TEM micrography (pH = 3 ± 0.1)

Table 5.S2. Statistical parameters for NPls from the TEM image measurements in "nm" unit (pH = 3 ± 0.1).

Amidine PS		Sulfate PS		SDS Coated PS	
nm	mV	nm	mV	nm	mV
177 ± 4	43 ± 2	114 ± 1	-34 ± 0	172 ± 1	-44 ± 0

Table 5.S3. Statistical parameters for NPls from the TEM image measurements in "nm" unit (pH = 3 ± 0.1).

Type of NPls	Size of population	Mean	σ	Max	Min	Median	25 %	75 %
Amidine PS	917	147	17	168	55	152	144	157
Sulfate PS	964	109	9	244	83	109	104	114
SDS Coated PS	229	168	17	204	105	170	161	179

S8. NPls transport behavior in quartz sand columns

Table 5.S4. Summary of injection conditions, maximum effluent concentrations (MEC), and retained mass values for intermediate concentration conditions.

Type	Injection Concentration (mg/L)	MEC (mg/L)	Retained Mass (%)
$[A\text{-}PS]^+$	150	0.4 ± 0.1	79 ± 4
	200	0.4 ± 0.1	84 ± 5
$[S\text{-}PS]^-$	150	1.2 ± 0.1	15 ± 4
	200	1.7 ± 0.1	17 ± 6

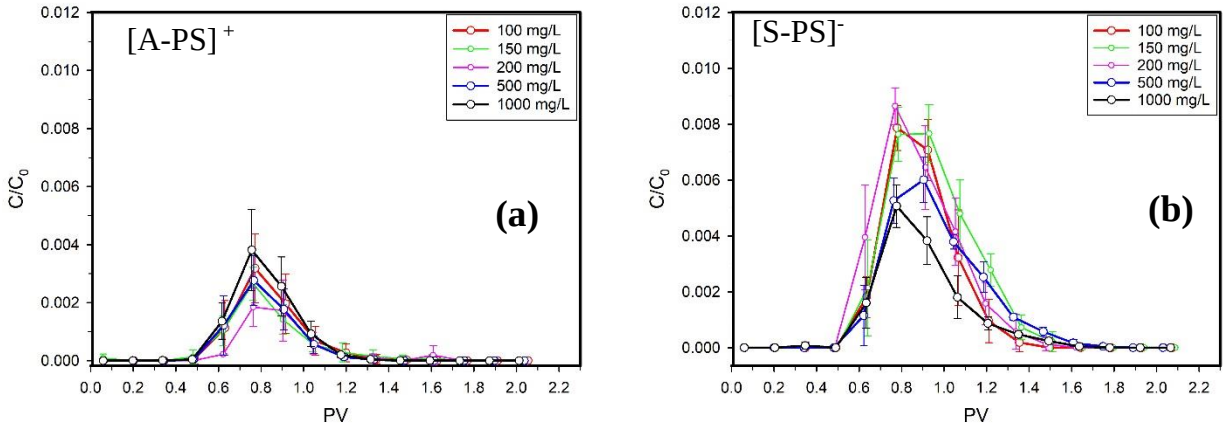


Figure 5.S8. Observed breakthrough curves for 100 mg/L, 150 mg/L, 200 mg/L, 500 mg/L and 1000 mg/L injection concentration (C_0) are shown for (a) [A-PS]+ (b) [S-PS]-.

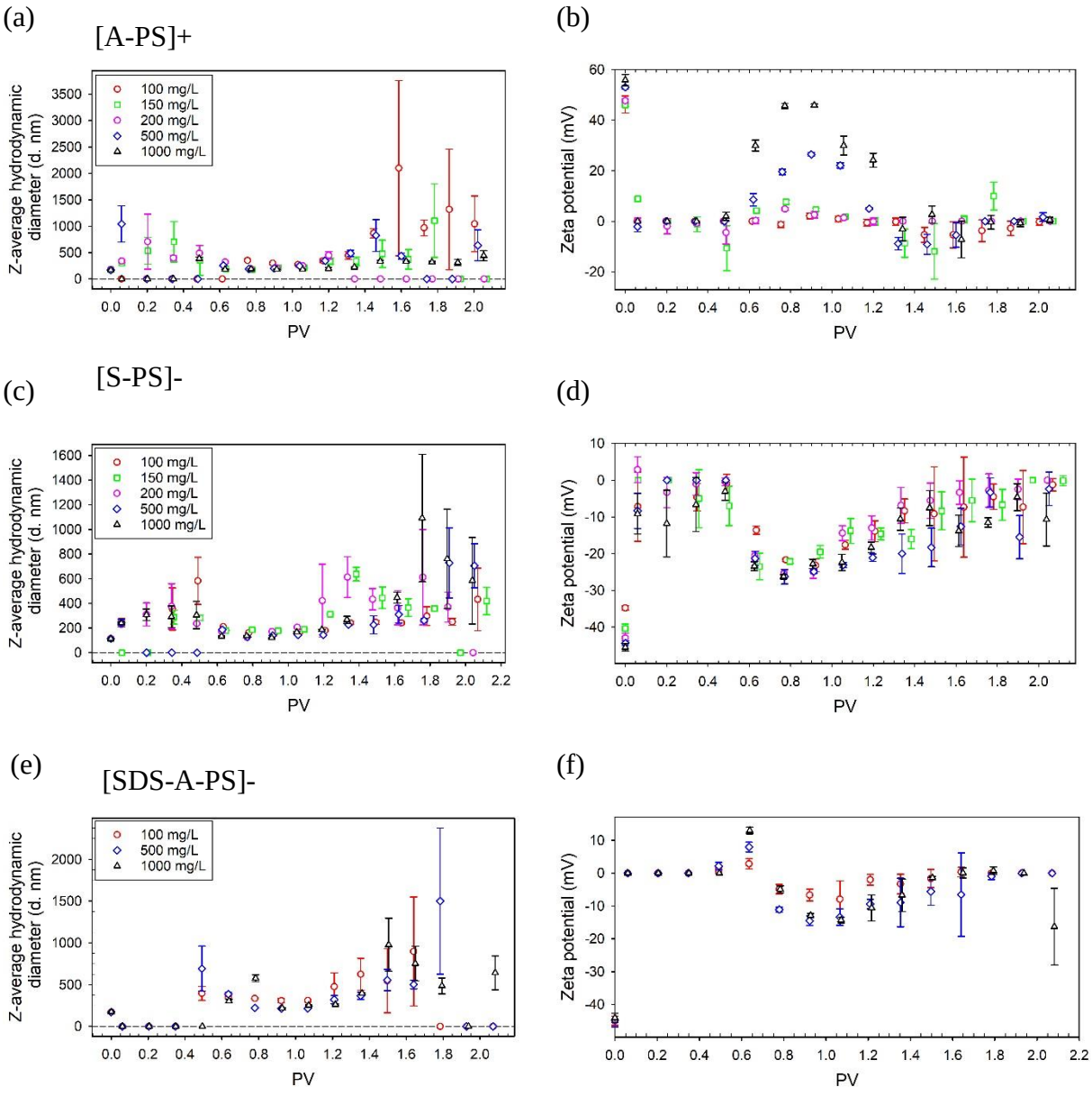


Figure 5.S9. Collective representation of hydrodynamic diameter and ζ potential vs PV graphs of experiments performed with [A-PS]+ (a, b), [S-PS]- (c, d) and [SDS-A-PS]- (e, f) for all effluents.

S9. Re-mobilization (Desorption)

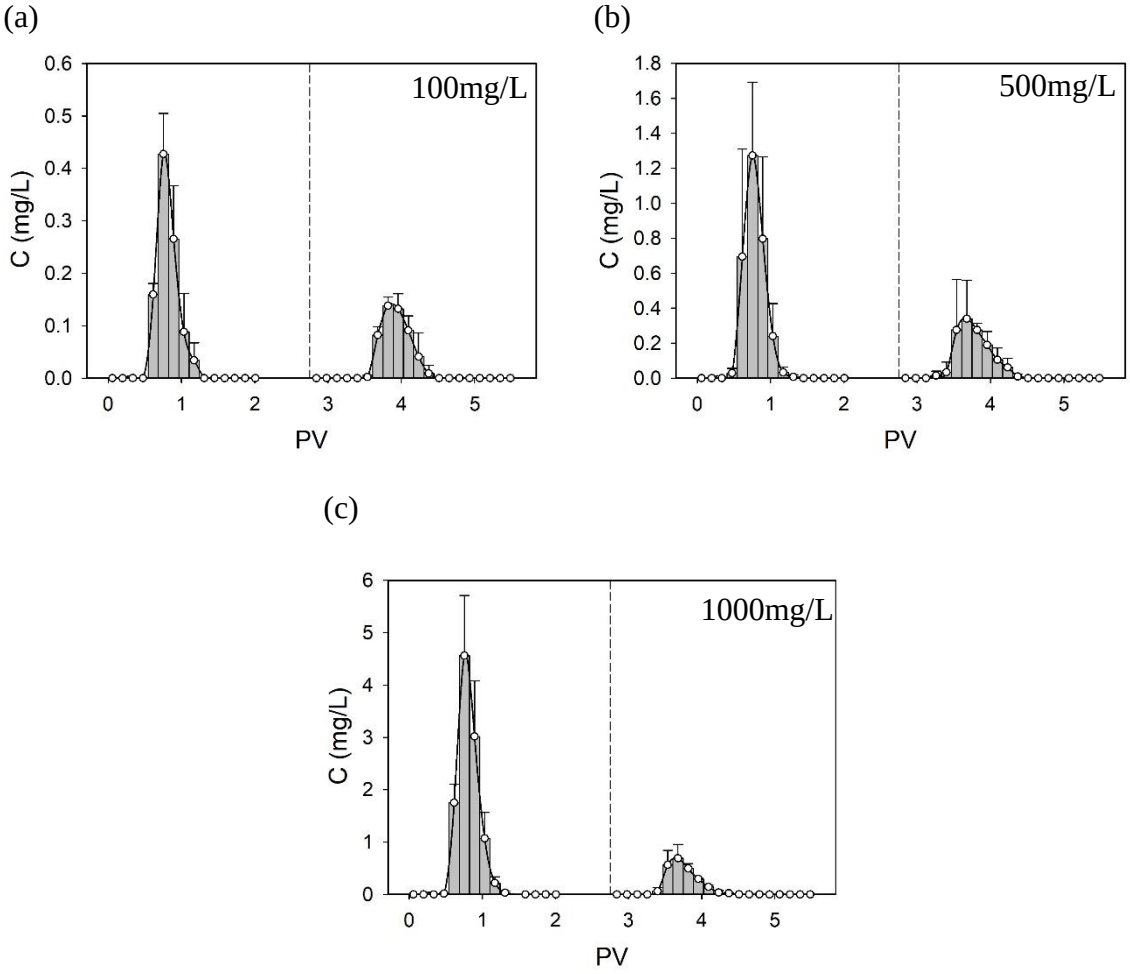


Figure 5.S10. The breakthrough curves of adsorption and desorption experiments with 100 mg/L (a), 500 mg/L (b) and 1000 mg/L (c) [A-PS]+ injection. The dash line represents the SDS injection.

S10. Aggregation Fractal Dimension

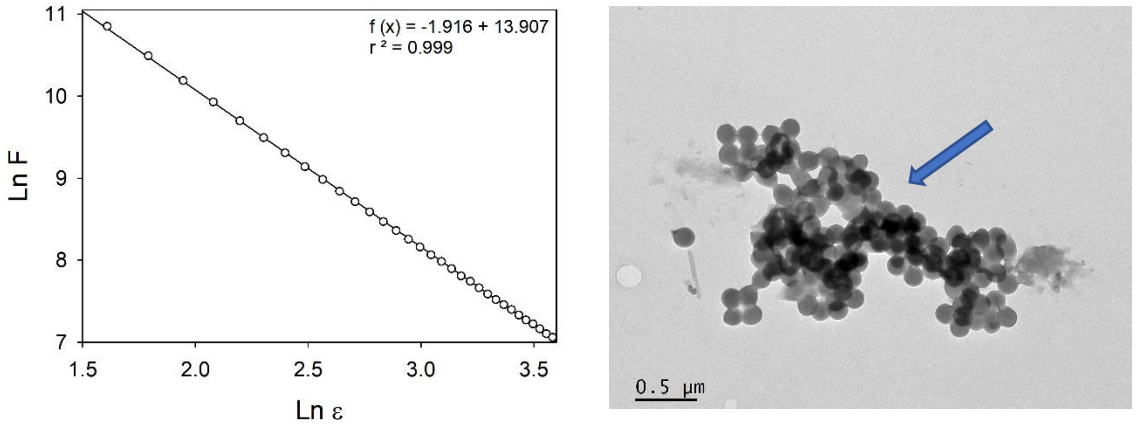


Figure 5.S11. Log-Log pilot of X axis is the ratio of the box size to the image size and Y axis is the number of pixels counted in per box for [A-PS]+ 500 mg/L injection conditions. (b) The TEM image of the [A-PS]+ NPls' homoaggregate (blue arrow) was used for D_f calculation.

6. CONCLUSIONS AND PERSPECTIVES

The purpose of this thesis work was to investigate and understand the behavior and fate of MPls and NPls through saturated porous media. Porous media denotes geological substances, such as sand, gravel, soil, fissured rocks, sandstone, and karstic limestone, characterized by void spaces permitting the flow of water. Invariably, these instances feature a combination of solid matrices and void spaces within their domains. In the scope of the thesis saturated porous media was associated with the sand filtration phase of drinking water treatment plants and water reservoirs of subsurface groundwater environment, both are important freshwater sources. Studies collectively shed light on the complex relationship between MNPls, porous media characteristics, and environmental factors. This highlights the crucial need to comprehend transport dynamics and retention efficiencies to develop effective mitigation strategies and protect water resources.

The initial phase of the research encompasses the association of MPls with diverse types of porous media to establish correlations pertinent to the protection of groundwater resources. Mathematical equations were employed to depict the flow and transport of MPls contaminants. Particular emphasis was placed on mathematical expressions delineating the movement of water and contaminants within the void spaces of saturated porous media. Upon acquiring a mathematical model tailored to specific scenarios, the subsequent solution, whether analytical or numerical, yields valuable insights into the dynamics of fluid flow and the behavior of MPls within the geological porous materials under examination.

First (Chapter 3), the analytical models were considered, with a key focus on addressing the primary challenge posed by the unique size and shape distribution of MPls, as identified in recent literature. Hydrodynamic parameters such as porosity and dispersivity of diverse porous media were determined using conservative tracers, and subsequently, these parameters were compared with those obtained from the transport of MPls. Both transport scenarios were addressed through analytical approaches utilizing inverse modeling techniques. Through experimentation involving various porous media and controlled flow rates in column experiments, the study elucidates the impact of mean velocity on particle transport, emphasizing the significance of pore size constraints and asymmetrical porosity distributions.

In the subsequent examination of MPls transport (Chapter 4), the complexity of mathematical formulations was heightened, prompting the adaptation of numerical solutions. This numerical approach provided insights into investigations of MPls transport through quartz sand, with a focus on reversible and irreversible sorption parameters across varying flow rates. Through experiments and numerical simulations, the study uncovers the interaction between sorption kinetics, flow dynamics, and particle characteristics. This provides valuable insights into filtration effectiveness and retention dynamics. Validation of the numerical model against experimental results showed a

minor difference of about 6%, indicating that the adapted numerical model, derived from solute transport theory, is suitable for modeling MPls transport.

In the investigation of the fate NPls in clean water (Chapter 5), special focus was placed on analyzing the sand filtration phase within industrial DWTPs, crucial for ensuring clean water supply. Here, the focus shifted from hydrodynamic parameters to physical and chemical properties of NPls, influencing their transport and behavior through sand filters. The sand filters utilized in the study were comprised of saturated quartz sand sourced from the DWTP of Geneva, Switzerland. Flow rate conditions were standardized to replicate operations within DWTPs, while variations in the concentration of NPls and surface properties were introduced. Investigations into the adsorption and desorption behavior of NPls encompassed considerations of size, zeta potential, concentration, electron microscopy, and image processing aspects. Through laboratory-based experiments replicating operational conditions, the study illuminates the impact of surface functionalities and surfactants on the retention and transport of NPls within porous media. By clarifying the complex relationship between surface charges, aggregation properties, and filtration efficiency, the research emphasizes the importance of improving sand filtration practices, which are essential components of industrial DWTPs.

Collectively, these studies highlight the interdisciplinary nature of plastic pollution research and underscore the importance of collaborative efforts in developing holistic solutions. By integrating experimental approaches, numerical modeling, and theoretical frameworks, these studies advance our understanding of plastic transport dynamics in porous media and provide crucial insights for informing policy decisions and implementing effective mitigation measures. Moving forward, ongoing research efforts need to take into account natural conditions, which inherently add complexity to studies but are essential aspects that need to be addressed. Nature involves numerous intricate dynamics and parameters beyond the scope of this study's focus. This study introduces complexity by incorporating various types of MNPls, each characterized by unique morphology and size distributions that are not extensively investigated elsewhere. These MPls types represent contaminants that may be more prevalent in environmental settings compared to reference type MPls. Additionally, the surface functionalities of NPls utilized in the study exhibit a wide range, and the variation in injection concentrations is extensive, contributing to the comprehensive examination of filtration processes. While previous studies have primarily concentrated on the adsorption aspect of sand filtration, this research also considers desorption phenomena in conjunction with other contaminants. It is crucial to assess the findings of this thesis in the context of future perspectives in the field, especially regarding the reference phase for future research.

The future perspective opened by this thesis involves investigating the transport of plastic contaminants through porous media while considering variations in water chemistry, flow velocities, plastic concentrations, co-presence with other contaminants or natural colloids, and the type of plastics used to reflect natural environmental conditions. This expanded perspective goes beyond the traditional focus on one-dimensional modeling and experimentation to include two-dimensional and three-dimensional media, providing a more comprehensive understanding of transport phenomena. Numerous studies have already confirmed the presence of MNPls in both

terrestrial and aquatic environments, indicating that plastic contaminants originate from various sources and eventually find their way into natural ecosystems. Understanding these transport processes is crucial for devising effective strategies to prevent the spread of these contaminants and mitigate their environmental impact.

The main findings are;

Microplastics:

- The investigation of MPls transport in groundwater is a relatively new area of research, with fundamental consequences suggesting that vertical movement of microplastics may contaminate groundwater. The migration of MPls into groundwater through soil-groundwater interactions poses risks to terrestrial ecological systems and human health, emphasizing the importance of developing strategies to safeguard freshwater resources.
- Polyethylene (PE) particles ranging from 200 to 500 μm were expected to pass through the large silica whose 97% of the pore size is higher than 800 μm but experimental results showed no transport, likely due to the large silica's predominantly large pore size distribution. Small silica and sand, with smaller pore sizes, were also unsuitable for PE particle transport. The fact that the porosity distributions are not symmetrical and the presence of small pores should be considered. When evaluating the pore size, it needs to be considered by using the maximum, minimum, and standard deviation values.
- Coarse gravel, featuring significantly larger pore sizes, facilitated PE particle transport. Breakthrough curves and hydrodynamic parameters were achieved with analytical solutions from fluorescent and MPls tracer experiments and were assessed together. Mean velocity (u) emerged as a critical parameter influencing PE particle transport in saturated porous media, with particles unable to transport effectively below a threshold mean velocity of 2.02 cm/min.
- Considering natural groundwater conditions, characterized by lower mean velocities, the potential accumulation of PE particles in aquifers poses additional concerns warranting further investigation.
- The hydrophobic nature and density properties of PE posed challenges for dispersing MPls in water. This challenge was addressed in two ways: by reducing the density of the background liquid and by adding surfactant.
- Sorption parameters changed with flow rate, where lower flow rates correlated with higher distribution coefficient (K_d) and mass transfer coefficient (β) values. Increases in K_d led to more gradual sorption and increased retardation, while variations in β affected the pace of sorption and peak concentration. Lower irreversible sorption rate (K_1) values were associated with higher concentration peak values and decreased retention efficiency at constant flow rates.
- Retention rates were assessed at different flow rates with numerical model (R_1) and experimental measurement (R_2). For a flow rate of 31 ml min^{-1}, the average retention rates are 28 ± 1% for R_1 and 24 ± 2% for R_2, respectively. At a flow rate of 65 ml min^{-1}, the average retention rates are 17 ± 1% for R_1 and 9 ± 4% for R_2.

- Retention rates were assessed at different flow rates, showing discrepancies between the numerical model and experimental measurements, with a mean absolute error of 6%.

Nanoplastics:

- Findings revealed that surface charges of NPLs, determined by various surface functionalities or coatings with surfactant molecules, significantly influenced retention behavior within porous media.
- The average retention efficiency of [A-PS]+, [S-PS]−, and [SDS-A-PS]− NPLs were 75%, 40%, and 15%, respectively, across all injection concentrations.
- Electrostatic interaction forces played a major role in retention, with different NPls with surface functionalities resulting in varying degrees of retention during sand filtration.
- Aggregate compactness, as indicated by fractal dimension values, influenced retention efficiencies, with smaller aggregate sizes associated with decreased retention.
- ζ potential measurements demonstrated an increase in positively charged particle retention with rising concentrations, while the effect on negatively charged particles was less pronounced.
- Remobilization of retained NPls was observed with the introduction of surfactants, highlighting the importance of considering pollutant interactions in subsequent treatment phases.

REFERENCES

Adin, A., Baumann, E. R., & Cleasby, J. L. (1979). Application of Filtration Theory To Pilot-Plant Design. *J Am Water Works Assoc*, *71*(1), 17–27. https://doi.org/10.1002/j.1551-8833.1979.tb04285.x

Ahfir, N., Wang, H. Q., Benamar, A., Alem, A., Massei, N., & Dupont, J. P. (2007). Transport and deposition of suspended particles in saturated porous media : hydrodynamic effect. *Hydrogeology Journal*, *15*, 659–668. https://doi.org/10.1007/s10040-006-0131-3

Alimi, O. S., Farner Budarz, J., Hernandez, L. M., & Tufenkji, N. (2018). Microplastics and Nanoplastics in Aquatic Environments: Aggregation, Deposition, and Enhanced Contaminant Transport. *Environmental Science and Technology*, *52*(4), 1704–1724. https://doi.org/10.1021/acs.est.7b05559

Allen, S., Allen, D., Karbalaei, S., Maselli, V., & Walker, T. R. (2022). Micro(nano)plastics sources, fate, and effects: What we know after ten years of research. *Journal of Hazardous Materials Advances*, *6*(February), 100057. https://doi.org/10.1016/j.hazadv.2022.100057

Amobonye, A., Bhagwat, P., Raveendran, S., Singh, S., & Pillai, S. (2021). Environmental Impacts of Microplastics and Nanoplastics: A Current Overview. *Frontiers in Microbiology*, *12*(December). https://doi.org/10.3389/fmicb.2021.768297

Andrady, A. L. (2011). Microplastics in the marine environment. *Marine Pollution Bulletin*, *62*(8), 1596–1605. https://doi.org/10.1016/j.marpolbul.2011.05.030

Atugoda, T., Vithanage, M., Wijesekara, H., Bolan, N., Sarmah, A. K., Bank, M. S., You, S., & Ok, Y. S. (2021). Interactions between microplastics, pharmaceuticals and personal care products: Implications for vector transport. *Environment International*, *149*, 106367. https://doi.org/10.1016/j.envint.2020.106367

Banihashem, S., & Karrabi, M. (2022). Investigation of suspended particle size effects on clogging of soil filters under laminar flow. *European Journal of Environmental and Civil Engineering*, *26*(6), 2294–2303. https://doi.org/10.1080/19648189.2020.1761455

Batu, V. (2005). Applied flow and solute transport modeling in aquifers: Fundamental principles and analytical and numerical methods. In *Applied Flow and Solute Transport Modeling in Aquifers: Fundamental Principles and Analytical and Numerical Methods*. https://doi.org/10.2136/vzj2006.0163br

Bear, J. (1988). *Dynamics of fluids in porous media*. American Elsevier Publishing Company.

Bear, J., & Cheng, A. H.-D. (2010). *Modeling Groundwater Flow and Contaminant Transport*. Springer Netherlands. https://doi.org/10.1007/978-1-4020-6682-5

Bharath K, M., Natesan, U., R, V., Kumar R, P., R, R., & S, S. (2021). Spatial distribution of

microplastic concentration around landfill sites and its potential risk on groundwater. *Chemosphere*, *277*, 130263. https://doi.org/https://doi.org/10.1016/j.chemosphere.2021.130263

Birch, Q. T., Potter, P. M., Pinto, P. X., Dionysiou, D. D., & Al-Abed, S. R. (2020). Sources, transport, measurement and impact of nano and microplastics in urban watersheds. *Reviews in Environmental Science and Bio/Technology*, *19*(2), 275–336. https://doi.org/10.1007/s11157-020-09529-x

Bläsing, M., & Amelung, W. (2018). Plastics in soil: Analytical methods and possible sources. *Science of The Total Environment*, *612*, 422–435. https://doi.org/10.1016/j.scitotenv.2017.08.086

Bradford, S. A., & Bettahar, M. (2006). Concentration dependent transport of colloids in saturated porous media. *Journal of Contaminant Hydrology*, *82*(1–2), 99–117. https://doi.org/10.1016/j.jconhyd.2005.09.006

Bradford, S. A., Yates, S. R., Bettahar, M., & Simunek, J. (2002). Physical factors affecting the transport and fate of colloids in saturated porous media. *Water Resources Research*, *38*(12), 63-1-63–12. https://doi.org/10.1029/2002wr001340

Carpenter, E. J., & Smith, K. L. (1972). Plastics on the Sargasso Sea Surface. *Science*, *175*(4027), 1240–1241. https://doi.org/10.1126/science.175.4027.1240

Chakraborti, R. K., Gardner, K. H., Atkinson, J. F., & Van Benschoten, J. E. (2003). Changes in fractal dimension during aggregation. *Water Research*, *37*(4), 873–883. https://doi.org/10.1016/S0043-1354(02)00379-2

Chu, X., Li, T., Li, Z., Yan, A., & Shen, C. (2019). Transport of microplastic particles in saturated porous media. *Water (Switzerland)*, *11*(12), 1–12. https://doi.org/10.3390/w11122474

Compère, F., Porel, G., & Delay, F. (2001). Transport and retention of clay particles in saturated porous media. Influence of ionic strength and pore velocity. *Journal of Contaminant Hydrology*, *49*(1–2), 1–21. https://doi.org/10.1016/S0169-7722(00)00184-4

da Costa, J. P., Santos, P. S. M., Duarte, A. C., & Rocha-Santos, T. (2016). (Nano)plastics in the environment – Sources, fates and effects. *Science of The Total Environment*, *566–567*, 15–26. https://doi.org/10.1016/j.scitotenv.2016.05.041

da Silva, D. J., & Wiebeck, H. (2022). ATR-FTIR Spectroscopy Combined with Chemometric Methods for the Classification of Polyethylene Residues Containing Different Contaminants. *Journal of Polymers and the Environment*, *30*(7), 3031–3044. https://doi.org/10.1007/s10924-022-02396-3

DeNovio, N. M., Saiers, J. E., & Ryan, J. N. (2004). Colloid Movement in Unsaturated Porous Media: Recent Advances and Future Directions. *Vadose Zone Journal*, *3*(2), 338–351. https://doi.org/10.2113/3.2.338

Dong, S., Xia, J., Sheng, L., Wang, W., Liu, H., & Gao, B. (2021). Transport characteristics of fragmental polyethylene glycol terephthalate (PET) microplastics in porous media under various chemical conditions. *Chemosphere*, *276*, 130214. https://doi.org/10.1016/j.chemosphere.2021.130214

Dong, Z., Qiu, Y., Zhang, W., Yang, Z., & Wei, L. (2018). Size-dependent transport and retention of micron-sized plastic spheres in natural sand saturated with seawater. *Water Research*, *143*, 518–526. https://doi.org/10.1016/j.watres.2018.07.007

Dong, Z., Zhu, L., Zhang, W., Huang, R., Lv, X. W., Jing, X., Yang, Z., Wang, J., & Qiu, Y. (2019). Role of surface functionalities of nanoplastics on their transport in seawater-saturated sea sand. *Environmental Pollution*, *255*, 113177. https://doi.org/10.1016/j.envpol.2019.113177

Dukhin, A. S., & Xu, R. (2020). Zeta-potential measurements. In V.-D. Hodoroaba, W. E. S. Unger, & A. G. Shard (Eds.), *In Micro and Nano Technologies, Characterization of Nanoparticles*, (pp. 213–224). Elsevier Inc. https://doi.org/https://doi.org/10.1016/B978-0-12-814182-3.00014-6

Einstein, A. (1905). Über die von der molekularkinetischen Theorie der Wärme geforderte Bewegung von in ruhenden Flüssigkeiten suspendierten Teilchen. *Annalen Der Physik*, *322*(8), 549–560.

European Commission. (2023). COMMISSION REGULATION (EU) 2023/2055 of 25 September 2023. In *Official Journal of the European Union: Vol. L* (Issue 238).

Farrokhbin, M., Stojimirović, B., Galli, M., Khajeh Aminian, M., Hallez, Y., & Trefalt, G. (2019). Surfactant mediated particle aggregation in nonpolar solvents. *Physical Chemistry Chemical Physics*, *21*(35), 18866–18876. https://doi.org/10.1039/c9cp01985e

Ferreira, T., & Rasband, W. (2012). ImageJ User Guide ImageJ/Fiji 1.46. *Image J User Guide*. https://doi.org/10.1038/nmeth.2019

Fetter, C. W. (1999). *Contaminant Hydrogeology* (2nd Editio). Prentice Hall Inc.

Fetter, C. W. (2014). *Applied Hydrogeology* (4th Editio). Prentice Hall.

Fetter, C. W., Boving, T., & Kreamer, D. (2018). *Contaminant Hydrogeology (Third Edition)*.

Field, M. S., Wilhelm, R. G., Quinlan, J. F., & Aley, T. J. (1995). An assessment of the potential adverse properties of fluorescent tracer dyes used for groundwater tracing. *Environmental Monitoring and Assessment*, *38*(1), 75–96. https://doi.org/10.1007/BF00547128

GESAMP. (2015). Sources, fate and effects of microplastics in the marine environment: a global assessment. In P. J. Kershaw (Ed.), *International Maritime Organization*.

Geyer, R., Jambeck, J. R., & Law, K. L. (2017). Production, use, and fate of all plastics ever made. *Science Advances*, *3*(7), 25–29. https://doi.org/10.1126/sciadv.1700782

Goeppert, N., & Goldscheider, N. (2021). Experimental field evidence for transport of microplastic tracers over large distances in an alluvial aquifer. *Journal of Hazardous Materials*, *408*(November 2020), 124844. https://doi.org/10.1016/j.jhazmat.2020.124844

Goldscheider, N., & Drew, D. (2007). Methods in Karst Hydrogeology: IAH: International Contributions to Hydrogeology, 26. In *Hydrogeology Journal* (1st Editio). CRC Press. https://doi.org/10.1201/9781482266023

Gouin, T., Roche, N., Lohmann, R., & Hodges, G. (2011). A Thermodynamic Approach for

Assessing the Environmental Exposure of Chemicals Absorbed to Microplastic. *Environmental Science & Technology*, *45*(4), 1466–1472. https://doi.org/10.1021/es1032025

Guo, X., Hu, G., Fan, X., & Jia, H. (2020). Sorption properties of cadmium on microplastics: The common practice experiment and A two-dimensional correlation spectroscopic study. *Ecotoxicology and Environmental Safety*, *190*, 110118. https://doi.org/10.1016/j.ecoenv.2019.110118

Harter, T. (2003). Basic Concepts of Groundwater Hydrology. *Basic Concepts of Groundwater Hydrology*, 1–6. https://doi.org/10.3733/ucanr.8083

He, L., Wu, D., Rong, H., Li, M., Tong, M., & Kim, H. (2018). Influence of Nano- and Microplastic Particles on the Transport and Deposition Behaviors of Bacteria in Quartz Sand. *Environmental Science and Technology*, *52*(20), 11555–11563. https://doi.org/10.1021/acs.est.8b01673

Henry, D. C. (1931). The cataphoresis of suspended particles. Part I.—The equation of cataphoresis. *Proceedings of the Royal Society*, *133*(821), 106–129. https://doi.org/10.1098/rspa.1931.0133

Hou, J., Xu, X., Lan, L., Miao, L., Xu, Y., You, G., & Liu, Z. (2020). Transport behavior of micro polyethylene particles in saturated quartz sand: Impacts of input concentration and physicochemical factors. *Environmental Pollution*, *263*, 114499. https://doi.org/10.1016/j.envpol.2020.114499

Hou, J., Zhang, M., Wang, P., Wang, C., Miao, L., Xu, Y., You, G., Lv, B., Yang, Y., & Liu, Z. (2017). Transport and long-term release behavior of polymer-coated silver nanoparticles in saturated quartz sand: The impacts of input concentration, grain size and flow rate. *Water Research*, *127*, 86–95. https://doi.org/10.1016/j.watres.2017.10.017

Hüffer, T., Metzelder, F., Sigmund, G., Slawek, S., Schmidt, T. C., & Hofmann, T. (2019). Polyethylene microplastics influence the transport of organic contaminants in soil. *Science of the Total Environment*, *657*, 242–247. https://doi.org/10.1016/j.scitotenv.2018.12.047

Hul, G. J., Ramseier Gentile, S., Zimmermann, S., & Stoll, S. (2022). Towards a better understanding of CeO2 manufactured nanoparticles adsorption onto sand grains used in drinking water treatment plants. *Colloids and Surfaces A: Physicochemical and Engineering Aspects*, *646*. https://doi.org/10.1016/j.colsurfa.2022.129000

Hul, G., Martignier, A., Gentile, S. R., Zimmermann, S., Ramaciotti, P., Perdaems, P., & Stoll, S. (2024). Insights into polystyrene nanoplastics adsorption mechanisms onto quartz sand used in drinking water treatment plants. *Science of The Total Environment*, *908*, 168076. https://doi.org/10.1016/j.scitotenv.2023.168076

Hul, G., Okutan, H., Le Coustumer, P., Ramseier Gentile, S., Zimmermann, S., Ramaciotti, P., Perdaems, P., & Stoll, S. (2024). Influence of Concentration, Surface Charge, and Natural Water Components on the Transport and Adsorption of Polystyrene Nanoplastics in Sand Columns. *Nanomaterials*, *14*(6), 529. https://doi.org/10.3390/nano14060529

Hul, G., Ramseier Gentile, S., Zimmermann, S., & Stoll, S. (2022). Towards a better understanding of CeO2 manufactured nanoparticles adsorption onto sand grains used in drinking water

treatment plants. *Colloids and Surfaces A: Physicochemical and Engineering Aspects*, *646*(April), 129000. https://doi.org/10.1016/j.colsurfa.2022.129000

Hul, G., Seijo, M., Carnal, F., Cornelis, G., & Stoll, S. (2021). Effect of deposition, detachment and aggregation processes on nanoparticle transport in porous media using Monte Carlo simulations. *Environmental Science: Nano*, *8*(8), 2223–2234. https://doi.org/10.1039/D1EN00034A

ISO/TR 21960. (2022). *Plastics — Environmental aspects — State of knowledge and methodologies*.

ISO 24187. (2023). *Principles for the analysis of microplastics present in the environment*.

Ivar do Sul, J. A., & Costa, M. F. (2014). The present and future of microplastic pollution in the marine environment. *Environmental Pollution*, *185*, 352–364. https://doi.org/10.1016/j.envpol.2013.10.036

Ivar Do Sul, J. A., & Costa, M. F. (2014). The present and future of microplastic pollution in the marine environment. *Environmental Pollution*, *185*, 352–364. https://doi.org/10.1016/j.envpol.2013.10.036

Jiang, B., Kauffman, A. E., Li, L., McFee, W., Cai, B., Weinstein, J., Lead, J. R., Chatterjee, S., Scott, G. I., & Xiao, S. (2020). Health impacts of environmental contamination of micro- And nanoplastics: A review. *Environmental Health and Preventive Medicine*, *25*(1), 1–15. https://doi.org/10.1186/s12199-020-00870-9

Jiang, Y., Yin, X., Xi, X., Guan, D., Sun, H., & Wang, N. (2021). Effect of surfactants on the transport of polyethylene and polypropylene microplastics in porous media. *Water Research*, *196*, 117016. https://doi.org/10.1016/j.watres.2021.117016

Jiang, Y., Zhou, S., Fei, J., Qin, Z., Yin, X., Sun, H., & Sun, Y. (2022). Transport of different microplastics in porous media: Effect of the adhesion of surfactants on microplastics. *Water Research*, *215*(March), 118262. https://doi.org/10.1016/j.watres.2022.118262

Jódar-Reyes, A. B., Martín-Rodríguez, A., & Ortega-Vinuesa, J. L. (2006). Effect of the ionic surfactant concentration on the stabilization/destabilization of polystyrene colloidal particles. *Journal of Colloid and Interface Science*, *298*(1), 248–257. https://doi.org/10.1016/j.jcis.2005.12.035

Kanniah, V., Wu, P., Mandzy, N., & Grulke, E. A. (2012). Fractal analysis as a complimentary technique for characterizing nanoparticle size distributions. *Powder Technology*, *226*, 189–198. https://doi.org/10.1016/j.powtec.2012.04.041

Karperien, A. (1999). *FracLac for ImageJ*. http://rsb.info.nih.gov/ij/plugins/fraclac/FLHelp/Introduction.htm

Karperien, A. (2004). *FracLac Advanced User's Manual* (Issue June).

Koelmans, A. A., Mohamed Nor, N. H., Hermsen, E., Kooi, M., Mintenig, S. M., & De France, J. (2019). Microplastics in freshwaters and drinking water: Critical review and assessment of data quality. *Water Research*, *155*, 410–422. https://doi.org/10.1016/j.watres.2019.02.054

Koutnik, V. S., Leonard, J., Alkidim, S., DePrima, F. J., Ravi, S., Hoek, E. M. V., & Mohanty, S. K. (2021). Distribution of microplastics in soil and freshwater environments: Global analysis and framework for transport modeling. *Environmental Pollution*, *274*, 116552. https://doi.org/10.1016/j.envpol.2021.116552

Kreft, A., & Zuber, A. (1978). On the physical meaning of the dispersion equation and its solutions for different initial and boundary conditions. *Chemical Engineering Science*. https://doi.org/10.1016/0009-2509(78)85196-3

Kumar, M., Xiong, X., He, M., Tsang, D. C. W., Gupta, J., Khan, E., Harrad, S., Hou, D., Ok, Y. S., & Bolan, N. S. (2020). Microplastics as pollutants in agricultural soils. *Environmental Pollution*, *265*, 114980. https://doi.org/10.1016/j.envpol.2020.114980

Landini, G. (2011). Fractals in microscopy. *Journal of Microscopy*, *241*(1), 1–8. https://doi.org/10.1111/j.1365-2818.2010.03454.x

Law, K. L., & Thompson, R. C. (2014). Microplastics in the seas. *Science*, *345*(6193), 144–145. https://doi.org/10.1126/science.1254065

Lee, S. G., Lee, S., & Choi, J. W. (2021). Nonlinear sorption of organic contaminant during two-dimensional transport in saturated sand. *Water (Switzerland)*, *13*(11), 1–16. https://doi.org/10.3390/w13111557

Li, H., Lu, X., Wang, S., Zheng, B., & Xu, Y. (2021). Vertical migration of microplastics along soil profile under different crop root systems. *Environmental Pollution*, *278*, 116833. https://doi.org/10.1016/j.envpol.2021.116833

Li, J., Song, Y., & Cai, Y. (2020). Focus topics on microplastics in soil : Analytical methods , occurrence , transport , and ecological risks *. *Environmental Pollution*, *257*, 113570. https://doi.org/10.1016/j.envpol.2019.113570

Li, M., Zhang, M., Rong, H., Zhang, X., He, L., Han, P., & Tong, M. (2021). Transport and deposition of plastic particles in porous media during seawater intrusion and groundwater-seawater displacement processes. *Science of the Total Environment*, *781*, 146752. https://doi.org/10.1016/j.scitotenv.2021.146752

Li, M., Zhang, X., Yi, K., He, L., Han, P., & Tong, M. (2021). Transport and deposition of microplastic particles in saturated porous media: Co-effects of clay particles and natural organic matter. *Environmental Pollution*, *287*(March), 117585. https://doi.org/10.1016/j.envpol.2021.117585

Li, Y., Li, J., Ding, J., Song, Z., Yang, B., Zhang, C., & Guan, B. (2022). Degradation of nano-sized polystyrene plastics by ozonation or chlorination in drinking water disinfection processes. *Chemical Engineering Journal*, *427*(131690), 1–8. https://doi.org/10.1016/j.cej.2021.131690

Li, Y., Wang, X., Fu, W., Xia, X., Liu, C., Min, J., Zhang, W., & Crittenden, J. C. (2019). Interactions between nano/micro plastics and suspended sediment in water: Implications on aggregation and settling. *Water Research*, *161*, 486–495. https://doi.org/10.1016/j.watres.2019.06.018

Liang, Y., Luo, Y., Shen, C., & Bradford, S. A. (2022). Micro- and nanoplastics retention in porous

media exhibits different dependence on grain surface roughness and clay coating with particle size. *Water Research*, *221*(June), 118717. https://doi.org/10.1016/j.watres.2022.118717

Ling, X., Yan, Z., Liu, Y., & Lu, G. (2021). Transport of nanoparticles in porous media and its effects on the co- existing pollutants *. *Environmental Pollution*, *283*, 117098. https://doi.org/10.1016/j.envpol.2021.117098

Lowry, G. V, Hill, R. J., Harper, S., Rawle, A. F., Hendren, C. O., Klaessig, F., & Nobbmann, U. (2016). Environmental Science Nano Guidance to improve the scientific value of zeta-potential measurements in nanoEHS. *Environmental Science: Nano*, *3*, 953–965. https://doi.org/10.1039/C6EN00136J

Lu, T., Gilfedder, B. S., Peng, H., Niu, G., & Frei, S. (2021). Effects of clay minerals on the transport of nanoplastics through water-saturated porous media. *Science of the Total Environment*, *796*, 148982. https://doi.org/10.1016/j.scitotenv.2021.148982

Maaß, S., Daphi, D., Lehmann, A., & Rillig, M. C. (2017). Transport of microplastics by two collembolan species. *Environmental Pollution*, *225*, 456–459. https://doi.org/10.1016/j.envpol.2017.03.009

Maharana, D., Saha, M., Dar, J. Y., Rathore, C., Sreepada, R. A., Xu, X. R., Koongolla, J. B., & Li, H. X. (2020). Assessment of micro and macroplastics along the west coast of India: Abundance, distribution, polymer type and toxicity. *Chemosphere*, *246*, 125708. https://doi.org/10.1016/j.chemosphere.2019.125708

Maloszewski, P., Harum, T., & Benischke, R. (1992). Mathematical modelling of tracer experiments in the karst of Lurbach system. *Hydrogeologie*, *43*, 116–136.

Mandelbrot, B. B. (1982). *The fractal geometry of nature*. W.H.Freeman and Co.

Matthies, M., Witt, J., & Klasmeier, J. (2008). Determination of soil biodegradation half-lives from simulation testing under aerobic laboratory conditions: A kinetic model approach. *Environmental Pollution*, *156*(1), 99–105. https://doi.org/10.1016/j.envpol.2007.12.040

Maurice, L., Farrant, A. R., Mathewson, E., & Atkinson, T. (2023). Karst hydrogeology of the Chalk and implications for groundwater protection. *Geological Society, London, Special Publications*, *517*(1), 39–62. https://doi.org/10.1144/sp517-2020-267

McCormick, A. R., Hoellein, T. J., London, M. G., Hittie, J., Scott, J. W., & Kelly, J. J. (2016). Microplastic in surface waters of urban rivers: concentration, sources, and associated bacterial assemblages. *Ecosphere*, *7*(11). https://doi.org/10.1002/ecs2.1556

Meng, Z., Recoura-Massaquant, R., Chaumot, A., Stoll, S., & Liu, W. (2023). Acute toxicity of nanoplastics on Daphnia and Gammarus neonates: Effects of surface charge, heteroaggregation, and water properties. *Science of The Total Environment*, *854*, 158763. https://doi.org/10.1016/j.scitotenv.2022.158763

Mintenig, S. M., Int-Veen, I., Löder, M. G. J., Primpke, S., & Gerdts, G. (2017). Identification of microplastic in effluents of waste water treatment plants using focal plane array-based micro-Fourier-transform infrared imaging. *Water Research*, *108*, 365–372. https://doi.org/10.1016/j.watres.2016.11.015

Mintenig, S. M., Löder, M. G. J., Primpke, S., & Gerdts, G. (2019). Low numbers of microplastics detected in drinking water from ground water sources. *Science of The Total Environment*, *648*, 631–635. https://doi.org/10.1016/j.scitotenv.2018.08.178

Molnar, I. L., Johnson, W. P., Gerhard, J. I., Willson, C. S., & O'Carroll, D. M. (2015). Predicting colloid transport through saturated porous media: A critical review. *Water Resources Research*, *51*(9), 6804–6845. https://doi.org/10.1002/2015WR017318

Negrete Velasco, A., Ramseier Gentile, S., Zimmermann, S., & Stoll, S. (2022). Contamination and Removal Efficiency of Microplastics and Synthetic Fibres in a Conventional Drinking Water Treatment Plant. *Frontiers in Water*, *4*. https://doi.org/10.3389/frwa.2022.835451

Nielsen, D. R., & Biggar, J. W. (1962). Miscible Displacement: III. Theoretical Considerations. *Soil Science Society of America Journal*, *26*(3), 216–221. https://doi.org/10.2136/sssaj1962.03615995002600030010x

O'Connor, D., Pan, S., Shen, Z., Song, Y., Jin, Y., Wu, W., & Hou, D. (2019). Microplastics undergo accelerated vertical migration in sand soil due to small size and wet-dry cycles. *Environmental Pollution*, *249*, 527–534. https://doi.org/10.1016/j.envpol.2019.03.092

Ogata, A., & Banks, R. B. (1961). A Solution of the Differential Equation of Longitudinal Dispersion in Porous Media. In *Geological Survey Professional Paper 411-A*. United States Government Printing Office.

Okutan, H. M., Sağir, Ç., Fontaine, C., Nauleau, B., Kurtulus, B., Le Coustumer, P., & Razack, M. (2022). One-Dimensional Experimental Investigation of Polyethylene Microplastic Transport in a Homogeneous Saturated Medium. *Frontiers in Environmental Science*, *10*. https://doi.org/10.3389/fenvs.2022.885875

Panno, S. V., Kelly, W. R., Scott, J., Zheng, W., McNeish, R. E., Holm, N., Hoellein, T. J., & Baranski, E. L. (2019). Microplastic Contamination in Karst Groundwater Systems. *Groundwater*, *57*(2), 189–196. https://doi.org/10.1111/gwat.12862

Peng, L., & Wang, Y. (2022). Sediment organic carbon dominates the heteroaggregation of suspended sediment and nanoplastics in natural and surfactant-polluted aquatic environments. *Journal of Hazardous Materials*, *440*(May), 129802. https://doi.org/10.1016/j.jhazmat.2022.129802

Pivokonsky, M., Cermakova, L., Novotna, K., Peer, P., Cajthaml, T., & Janda, V. (2018). Occurrence of microplastics in raw and treated drinking water. *Science of the Total Environment*, *643*, 1644–1651. https://doi.org/10.1016/j.scitotenv.2018.08.102

Praetorius, A., Badetti, E., Brunelli, A., Clavier, A., Gallego-Urrea, J. A., Gondikas, A., Hassellöv, M., Hofmann, T., Mackevica, A., Marcomini, A., Peijnenburg, W., Quik, J. T. K., Seijo, M., Stoll, S., Tepe, N., Walch, H., & Von Der Kammer, F. (2020). Strategies for determining heteroaggregation attachment efficiencies of engineered nanoparticles in aquatic environments. *Environmental Science: Nano*, *7*(2), 351–367. https://doi.org/10.1039/c9en01016e

Prata, J. C., da Costa, J. P., Lopes, I., Duarte, A. C., & Rocha-Santos, T. (2020). Environmental exposure to microplastics: An overview on possible human health effects. *Science of the Total*

Environment, *702*, 134455. https://doi.org/10.1016/j.scitotenv.2019.134455

Pulido-Reyes, G., Magherini, L., Bianco, C., Sethi, R., von Gunten, U., Kaegi, R., & Mitrano, D. M. (2022). Nanoplastics removal during drinking water treatment: Laboratory- and pilot-scale experiments and modeling. *Journal of Hazardous Materials*, *436*(February), 129011. https://doi.org/10.1016/j.jhazmat.2022.129011

Pulido-Reyes, G., Magherini, L., Bianco, C., Sethi, R., Von Gunten, U., Kaegi, R., & Mitrano, D. M. (2022). Nanoplastics removal during drinking water treatment : Laboratory- and pilot-scale experiments and modeling. *Journal of Hazardous Materials*, *436*(April), 129011. https://doi.org/10.1016/j.jhazmat.2022.129011

Qi, S., Song, J., Shentu, J., Chen, Q., & Lin, K. (2022). Attachment and detachment of large microplastics in saturated porous media and its influencing factors. *Chemosphere*, *305*(April), 135322. https://doi.org/10.1016/j.chemosphere.2022.135322

Raaijmakers, B. (2018). *Solute transport in porous media ; An experimental pore-scale study using physical micromodels*. Utrecht University.

Ramirez Arenas, L., Ramseier Gentile, S., Zimmermann, S., & Stoll, S. (2020). Coagulation of TiO2, CeO2 nanoparticles, and polystyrene nanoplastics in bottled mineral and surface waters. Effect of water properties, coagulant type, and dosage. *Water Environment Research*, *92*(8), 1184–1194. https://doi.org/10.1002/wer.1313

Ramirez Arenas, L., Ramseier Gentile, S., Zimmermann, S., & Stoll, S. (2022). Fate and removal efficiency of polystyrene nanoplastics in a pilot drinking water treatment plant. *Science of the Total Environment*, *813*, 152623. https://doi.org/10.1016/j.scitotenv.2021.152623

Ren, Z., Gui, X., Wei, Y., Chen, X., Xu, X., Zhao, L., Qiu, H., & Cao, X. (2021). Chemical and photo-initiated aging enhances transport risk of microplastics in saturated soils: Key factors, mechanisms, and modeling. *Water Research*, *202*, 117407. https://doi.org/10.1016/j.watres.2021.117407

Ren, Z., Gui, X., Xu, X., Zhao, L., Qiu, H., & Cao, X. (2021). Microplastics in the soil-groundwater environment: Aging, migration, and co-transport of contaminants – A critical review. *Journal of Hazardous Materials*, *419*, 126455. https://doi.org/10.1016/j.jhazmat.2021.126455

Rillig, M. C., Ziersch, L., & Hempel, S. (2017). Microplastic transport in soil by earthworms. *Scientific Reports*, *March*, 1–6. https://doi.org/10.1038/s41598-017-01594-7

Runkel, R. L. (2015). On the use of rhodamine WT for the characterization of stream hydrodynamics and transient storage. *Water Resources Research*, *51*(8), 6125–6142. https://doi.org/10.1002/2015WR017201

Sabatini, D. A., & Austin, T. A. (1991). Characteristics of Rhodamine WT and Fluorescein as Adsorbing Ground-Water Tracers. *Groundwater*, *29*(3), 341–349. https://doi.org/10.1111/j.1745-6584.1991.tb00524.x

Samandra, S., Johnston, J. M., Jaeger, J. E., Symons, B., Xie, S., Currell, M., Ellis, A. V, & Clarke, B. O. (2022). Microplastic contamination of an unconfined groundwater aquifer in Victoria, Australia. *Science of the Total Environment*, *802*, 149727. https://doi.org/10.1016/j.scitotenv.2021.149727

Shi, W., Wu, N., Zhang, Z., Liu, Y., Chen, J., & Li, J. (2024). A global review on the abundance and threats of microplastics in soils to terrestrial ecosystem and human health. *Science of The Total Environment*, *912*(September 2023), 169469. https://doi.org/10.1016/j.scitotenv.2023.169469

Shu, X., Wu, Y., Zhang, X., & Yu, F. (2023). Experiments and models for contaminant transport in unsaturated and saturated porous media – A review. *Chemical Engineering Research and Design*, *192*, 606–621. https://doi.org/10.1016/j.cherd.2023.02.022

Simunek, J., He, C., Pang, L., & Bradford, S. A. (2006). Colloid-Facilitated Solute Transport in Variably Saturated Porous Media: Numerical Model and Experimental Verification. *Vadose Zone Journal*, *5*, 1035–1047. https://doi.org/10.2136/vzj2005.0151

Skaggs, T. H., & Leij, F. J. (2002). 6.3 Solute Transport: Theoretical Background. In J. H. Dane & C. G. Topp (Eds.), *In Methods of Soil Analysis* (pp. 1353–1380). https://doi.org/10.2136/sssabookser5.4.c56

Smart, P. L., & Laidlaw, I. M. S. (1977). An evaluation of some fluorescent dyes for water tracing. *Water Resources Research*, *13*(1), 15–33. https://doi.org/10.1029/WR013i001p00015

Smoluchowski, M. (1921). Elektrische Endosmose und Strömungsströme. In *Handbuch der Elektrizität*.

Sun, P., Shijirbaatar, A., Fang, J., Owens, G., Lin, D., & Zhang, K. (2015). Distinguishable Transport Behavior of Zinc Oxide Nanoparticles in Silica Sand and Soil Columns. *Science of the Total Environment*, *505*, 189–198. https://doi.org/10.1016/j.scitotenv.2014.09.095

Sun, Y., Gao, B., Bradford, S. A., Wu, L., Chen, H., Shi, X., & Wu, J. (2015). Transport, retention, and size perturbation of graphene oxide in saturated porous media: Effects of input concentration and grain size. *Water Research*, *68*, 24–33. https://doi.org/10.1016/j.watres.2014.09.025

Sutton, D. J., Kabala, Z. J., Francisco, A., & Vasudevan, D. (2001). Limitations and potential of commercially available rhodamine WT as a groundwater tracer. *Water Resources Research*, *37*(6), 1641–1656. https://doi.org/10.1029/2000WR900295

Thompson, R. C., Olsen, Y., Mitchell, R. P., Davis, A., Rowland, S. J., John, A. W. G., McGonigle, D., & Russell, A. E. (2004). Lost at Sea: Where Is All the Plastic? *Science*, *304*(5672), 838–838. https://doi.org/10.1126/science.1094559

Thompson, R. C., Olson, Y., Mitchell, R. P., Davis, A., Rowland, S. J., John, A. W. G., McGonigle, D., & Russell, A. E. (2004). Lost at Sea: Where Is All the Plastic? *Science*, *304*(5672), 838. https://doi.org/10.1126/science.1094559

Torre, I. G., Heck, R. J., & Tarquis, A. M. (2020). MULTIFRAC: An ImageJ plugin for multiscale characterization of 2D and 3D stack images. *SoftwareX*, *12*. https://doi.org/10.1016/j.softx.2020.100574

Tufenkji, N., & Elimelech, M. (2004). Deviation from the Classical Colloid Filtration Theory in the Presence of Repulsive DLVO Interactions. *Langmuir*, *20*, 10818–10828.

Velasco, A. de J. N., Rard, L., Blois, W., Lebrun, D., Lebrun, F., Pothe, F., & Stoll, S. (2020).

Microplastic and fibre contamination in a remote Mountain lake in Switzerland. *Water (Switzerland)*, *12*(9), 1–16. https://doi.org/10.3390/W12092410

Waldschläger, K., Lechthaler, S., Stauch, G., & Schüttrumpf, H. (2020). Science of the Total Environment The way of microplastic through the environment – Application of the source-pathway-receptor model (review). *Science of the Total Environment*, *713*, 136584. https://doi.org/https://doi.org/10.1016/j.scitotenv.2020.136584

Wang, J., Zhao, X., Wu, A., Tang, Z., Niu, L., Wu, F., Wang, F., Zhao, T., & Fu, Z. (2021). Aggregation and stability of sulfate-modified polystyrene nanoplastics in synthetic and natural waters. *Environmental Pollution*, *268*, 114240. https://doi.org/10.1016/j.envpol.2020.114240

Wang, Y., Xie, Y., Fan, W., Yang, Z., Tan, W., Huo, M., & Huo, Y. (2022). Environment Mechanism comparisons of transport-deposition-reentrainment between microplastics and natural mineral particles in porous media : A theoretical and experimental study. *Science of the Total Environment*, *850*(May), 157998. https://doi.org/10.1016/j.scitotenv.2022.157998

Wei, Y., & Chen, Y. (2023). The Urgent Need to Investigate Microplastic Contamination in Groundwater: Soil and Groundwater Interactions as Key Drivers. *ACS ES and T Water*, *3*(12), 3736–3740. https://doi.org/10.1021/acsestwater.3c00645

Windsor, F. M., Durance, I., Horton, A. A., Thompson, R. C., Tyler, C. R., & Ormerod, S. J. (2019). A catchment-scale perspective of plastic pollution. *Global Change Biology*, *25*(4), 1207–1221. https://doi.org/10.1111/gcb.14572

World Health Organization. (2006). *Protecting Groundwater for Health: Managing the Quality of Drinking-water Sources* (O. Schmoll, G. Howard, J. Chilton, & I. Chorus (eds.)). IWA Publishing.

Wright, S. L., Thompson, R. C., & Galloway, T. S. (2013). The physical impacts of microplastics on marine organisms: a review. *Environmental Pollution (Barking, Essex : 1987)*, *178*, 483–492. https://doi.org/10.1016/j.envpol.2013.02.031

Wu, J., Jiang, R., Lin, W., & Ouyang, G. (2019). Effect of salinity and humic acid on the aggregation and toxicity of polystyrene nanoplastics with different functional groups and charges. *Environmental Pollution*, *245*, 836–843. https://doi.org/10.1016/j.envpol.2018.11.055

Wu, P., Tang, Y., Dang, M., Wang, S., Jin, H., Liu, Y., Jing, H., Zheng, C., Yi, S., & Cai, Z. (2020). Spatial-temporal distribution of microplastics in surface water and sediments of Maozhou River within Guangdong-Hong Kong-Macao Greater Bay Area. *Science of the Total Environment*, *717*, 135187. https://doi.org/10.1016/j.scitotenv.2019.135187

Wu, X., Lyu, X., Li, Z., Gao, B., Zeng, X., Wu, J., & Sun, Y. (2020). Transport of polystyrene nanoplastics in natural soils: Effect of soil properties, ionic strength and cation type. *Science of the Total Environment*, *707*, 136065. https://doi.org/10.1016/j.scitotenv.2019.136065

Xing, X., Zhang, Y., Zhou, G., Zhang, Y., Yue, J., Wang, X., & Yang, Z. (2023). Mechanisms of polystyrene nanoplastics adsorption onto activated carbon modified by ZnCl2. *Science of the Total Environment*, *876*(March). https://doi.org/10.1016/j.scitotenv.2023.162763

Xu, R. (2008). Progress in nanoparticles characterization : Sizing and zeta potential measurement. *Particuology*, *6*(6), 112–115. https://doi.org/10.1016/j.partic.2007.12.002

Zhang, M., Hou, J., Wu, J., Miao, L., & Zeng, Y. (2023). Effects of input concentration, media particle size, and flow rate on fate of polystyrene nanoplastics in saturated porous media. *Science of the Total Environment*, *881*(February), 163237. https://doi.org/10.1016/j.scitotenv.2023.163237

Zhang, P., Bai, B., Jiang, S., Wang, P., & Li, H. (2016). Transport and deposition of suspended particles in saturated porous media: Effect of hydrodynamic forces and pore structure. *Water Science and Technology: Water Supply*, *16*(4), 951–960. https://doi.org/10.2166/ws.2016.011

Zhang, T., Murphy, M. J., Yu, H., Bagaria, H. G., Yoon, K. Y., Neilson, B. M., Bielawski, C. W., Johnston, K. P., Huh, C., & Bryant, S. L. (2015). Investigation of Nanoparticle Adsorption During Transport in Porous Media. *SPE Journal*, *20*(04), 667–677. https://doi.org/10.2118/166346-PA

Zhang, Y., Diehl, A., Lewandowski, A., Gopalakrishnan, K., & Baker, T. (2020). Removal efficiency of micro- and nanoplastics (180 nm – 125 μ m) during drinking water treatment. *Science of the Total Environment*, *720*, 137383. https://doi.org/10.1016/j.scitotenv.2020.137383

Zhao, P., Cui, L., Zhao, W., Tian, Y., Li, M., Wang, Y. Y., & Chen, Z. (2021). Cotransport and deposition of colloidal polystyrene microplastic particles and tetracycline in porous media: The impact of ionic strength and cationic types. *Science of the Total Environment*, *753*, 142064. https://doi.org/10.1016/j.scitotenv.2020.142064

Zheng, C., Hill, M. C., & Cao, G. (2013). MT3DMS: Model use, calibration, and validation. *2012 American Society of Agricultural and Biological Engineers ISSN*, *July 2012*. https://doi.org/10.13031/2013.42263

Zheng, C., & Wang, P. P. (1999). *MT3DMS : A Modular Three-Dimensional Multispecies Transport Model for Simulation of Advection , Dispersion , and Chemical Reactions of Contaminants in Groundwater Systems ; Documentation and User ' s Guide* (Issue December).

Zięba-Palus, J. (2017). The usefulness of infrared spectroscopy in examinations of adhesive tapes for forensic purposes. *Forensic Science and Criminology Research*, *2*(2), 1–9. https://doi.org/10.15761/FSC.1000112